ABSTRACT

Title of dissertation: Measurement and Prediction of the Separated
Flow on a Rotor at High Advance Ratio

Luke Robert Smith, Doctor of Philosophy, 2020

Dissertation directed by: Associate Professor Anya R. Jones
Department of Aerospace Engineering

Flow separation is prevalent in a number of aerospace applications, but because of complex non-linearities in the governing equations, the resulting aerodynamic forces are challenging to model. This mathematical limitation is particularly impactful in the field of high speed rotorcraft. When a rotor operates at high advance ratio, a regime typical of high speed (and low power) flight, the blades of the rotor are subject to several unsteady motions that incur flow separation, including high pitch inputs and a region of reverse flow that occupies much of the rotor's retreating side. The aerodynamic forces in these regions are dominated by large-scale, coherent vortex structures that are poorly captured by conventional aerodynamics theories. The purpose of this work is to understand the physics of flow separation on high advance ratio rotors, and to leverage this understanding into a low-order, physics-based model for use in rotorcraft design applications.

The current work approaches this goal by identifying, understanding, and ultimately modeling the coherent flow structures present on a representative, sub-scale rotor system operating at high advance ratio. Flowfield measurements on this rotor revealed the presence of two distinct vortex structures, a “sharp-edge” vortex and a “blunt-edge” vortex, believed to dominate unsteady loading in the reverse flow region. The sharp-edge vortex was studied via a high-fidelity numerical simulation, and its growth was found to be dominated by 2-D mechanisms of vorticity transport. The insignificance of 3-D effects was attributed to a mutual cancellation of Coriolis forces and spanwise convection/tilting, a feature unique to reverse flow. Likewise, the blunt-edge vortex was studied in a series of 2-D surging and pitching wing experiments; its formation was found to largely depend on the unsteady, ”external” features of the flow, most notably the trailing wake. Together, these observations led to the development of a 2-D discrete vortex model capable of predicting the strength of the sharp-edge vortex and the timing of the blunt-edge vortex. The model has a computation time on the order of seconds, features only a single empirical parameter, and captures the fundamental physical mechanisms at play on a rotor at high advance ratio.

Measurement and Prediction of the Separated Flow on a Rotor at High Advance Ratio

by

Luke Robert Smith

Dissertation submitted to the Faculty of the Graduate School of the
University of Maryland, College Park in partial fulfillment
of the requirements for the degree of
Doctor of Philosophy
2020

Advisory Committee:
Professor Anya Jones, Chair/Advisor
Professor James Baeder
Professor Inderjit Chopra
Professor Johan Larsson
Professor Amir Riaz, Dean's Representative

© Copyright by
Luke Robert Smith
2020

Acknowledgments

I started working with Dr. Anya Jones in the spring of 2014. Shortly before my first day as an undergraduate researcher, I decided it would be a smart move to dye my hair bleach blonde. I looked, for lack of a better phrase, very odd. I will always be grateful that Dr. Jones saw promise in me then, and continued to see promise as I grew into a person with a naturally occurring hair color. Her patience, work ethic, and depth of knowledge is inspiring, and I am endlessly thankful for the guidance and respect Dr. Jones bestows on each of her students.

I would also like to thank my lab mates for their undoubtedly huge contribution to this work, particularly Field Manar, Peter Mancini, Gino Perrotta, André Bauknecht, Jonathan Lefebvre, Hülya Biler, and Girguis Sedky. That's a long list, but each of these folks is wildly intelligent, and played a major part in helping me understand fluid flows. A special, unique thanks is owed to one of the lab's first gurus: Dr. Andrew Lind. Andrew was my mentor throughout the first several years of my graduate studies, and he remains one of the kindest and most understanding people I have had the pleasure of meeting. I truly could not thank him enough for passing on his insights; this thesis most certainly would not exist without his wise teachings.

Finally, I owe a huge thanks to the University of Maryland Vertical Lift Center of Excellence (VLRCOE) for supporting my work financially over the past five years. Our funding contacts were continuously patient, engaged, and supportive as we pushed this project into new territory, and for that they have my utmost thanks and appreciation. This thesis was completed under the U.S. Army/Navy/NASA Vertical Lift Research Center of Excellence Cooperative Agreement, grant number W911W6-17-2-0004, with Mahendra Bhagwat serving as Program Manager and Technical Agent.

Table of Contents

List of Tables

List of Figures

Chapter 1: Introduction

The separated flow over an airfoil is among the most difficult aerodynamic phenomena to understand and predict. Observed in a broad range of fixed [1] and rotary wing applications [2], separation occurs when the flow very near the surface of an airfoil, typically confined to a thin region called the boundary layer, is ejected into the surrounding flowfield due to high pressure gradients at the wing surface. Figure 1.1 illustrates the difference between the more conventional attached flow over an airfoil, shown in figure 1.1(a), and a massively separated airfoil flow, shown in figure 1.1(b). The streamlines of the attached flow are organized, stick close to the airfoil surface, and are well-predicted by linear aerodynamic theories, even when the wing is subject to unsteady motion. The streamlines of the separated flow, in contrast, are more chaotic and rotational; the fluid dynamics of a separated flow are nonlinear, time-dependent, and mathematically complex. It has thus become a major goal of the unsteady aerodynamics community to (1) identify a coherent structure in separated flows, and (2) predict the behavior of these structures in a fashion similar to the more conventional attached flows.

Such a goal remains elusive, however, partially because of the expansive range of airfoil motions known to induce flow separation. From wind turbines to micro air

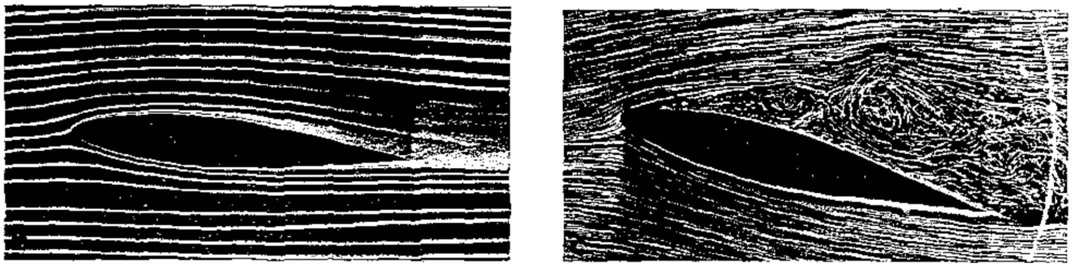

(a) Attached flow.

(b) Separated flow.

Figure 1.1: Flow visualization of the attached and separated flow over an airfoil [3].

vehicles, separated flows are highly variable, and their behavior strongly depends on the airfoil shape, the time-history of its motion, and any 3-D effects at play. With this in mind, the current work contributes to the study of separated flows by addressing a specific application, rotorcraft, where flow separation is a significant barrier to aerodynamic design. The ultimate goal of this thesis is then to investigate and model the separated flow that occurs in the complex, three-dimensional environment of a rotor operating in forward flight, an endeavor that has important ramifications both in the design of next-generation rotorcraft and in the understanding of separated flows at large.

1.1 Motivation: Rotorcraft Aerodynamics

Rotorcraft are perhaps the most versatile vehicles in the aerospace industry, capable of supporting vertical takeoff and precise maneuvering, but this versatility comes at the expense of a highly complex aerodynamic environment. Due to flow asymmetry on the rotor disk in edgewise flow (i.e., forward flight), the individual blades of a conventional helicopter undergo a number of unsteady motions, including dynamic pitch, flap, and lag, as a way of maintaining vehicle control. These unsteady motions, particularly blade pitch, can become quite aggressive at high forward flight speeds, meaning rotors must keep their thrust below an upper limit if they seek to avoid flow separation and stall. The onset of flow separation on a rotor blade can result in fatigue, a reduction in aerodynamic damping, and large blade torsional loading, and is one of several barriers that limit the flight envelope of conventional edgewise helicopters in forward flight [4].

Figure 1.2 shows a top-down view of the aerodynamic environment encountered by a conventional helicopter in forward flight, illustrating how separation fits into the overall context of helicopter aerodynamics. The distribution of velocity about the rotor hub is denoted by black arrows and represents a summation of the local rotational velocity (Ωr) and the forward flight velocity of the vehicle (U_∞). In figure 1.2, the local velocity on the right side (or "advancing" side) of the rotor is seen to be higher than what is seen on the left side (or "retreating" side) of the rotor, an asymmetric velocity distribution that drives the primary aerodynamic limitations of conventional helicopters. These include compressible effects near the advancing tip of the rotor ($0^\circ \leq \psi \leq 180^\circ$), where the local frestream velocity is at its highest; the potential for stall on the retreating side of the rotor ($180^\circ \leq \psi \leq 360^\circ$), where the blades pitch up to maintain roll control; and a region of reverse flow on the retreating side (shown in red), where the local freestream velocity travels from the geometric trailing edge of the blades to the geometric leading edge.

Of these effects, compressibility has historically been the main limiter in terms of the forward flight speed, and many modern, next-generation rotorcraft designs have implemented specific measures to mitigate drag due to compressibility effects.

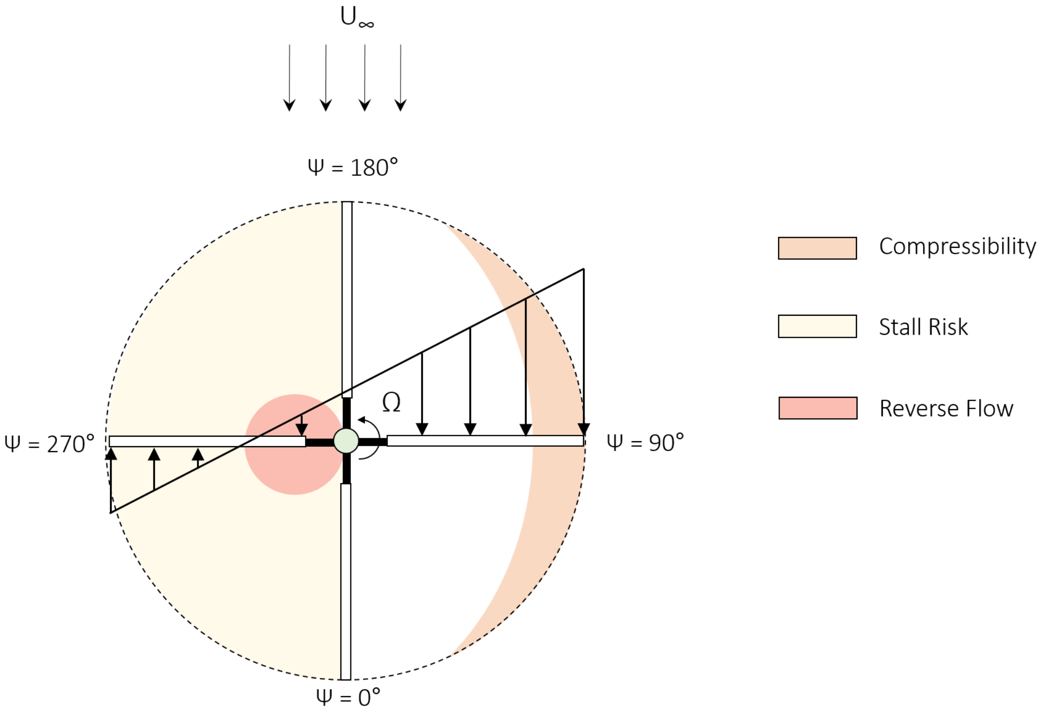

Figure 1.2: Top-down view of a conventional helicopter operating in forward flight at low advance ratio.

One particularly promising concept is that of the “slowed” rotor, where the angular velocity of the main rotor is decreased in forward flight and the ensuing loss of lift is compensated by auxiliary wings (or a second rotor in a “coaxial” configuration). The slowed rotor concept aims to reduce the Mach number at the advancing tip, and been successfully implemented in the Sikorsky XH-59A, the Sikorsky X2TD, and the Eurocopter X^3, all of which have flown above 200 kts (compared to a maximum of 160 kts for a typical helicopter) [5, 6]. This design concept, however, replaces the compressibility problem with another significant aerodynamic issue. Figure 1.3 shows a top-down view of the aerodynamic environment expected of a slowed rotor operating at reduced RPM in forward flight, revealing the presence of an excessively large reverse flow region, the size of which scales directly with the advance ratio, or the ratio of the forward flight velocity to the helicopter's maximum rotational velocity ($\mu = U_\infty/\Omega R$).

The presence of a large reverse flow region makes flow separation a much more pressing problem on slowed rotors compared to conventional designs. The blade-element views on the right-hand side of figure 1.3 demonstrate that the orientation of the reverse flow region is such that the geometric trailing edge of the rotor blade, which is typically “sharp” on a conventional helicopter blade, acts as the aerodynamic leading edge in reverse flow. A sharp leading edge, such as what would be found on a flat plate, is known to incur significant flow separation and vortex formation on wings in an unsteady flow [7]. A slowed rotor operating at high advance ratio, then, has two major sources of flow separation: (1) the large reverse flow region on its retreating side (red in figure 1.3), where separation occurs due

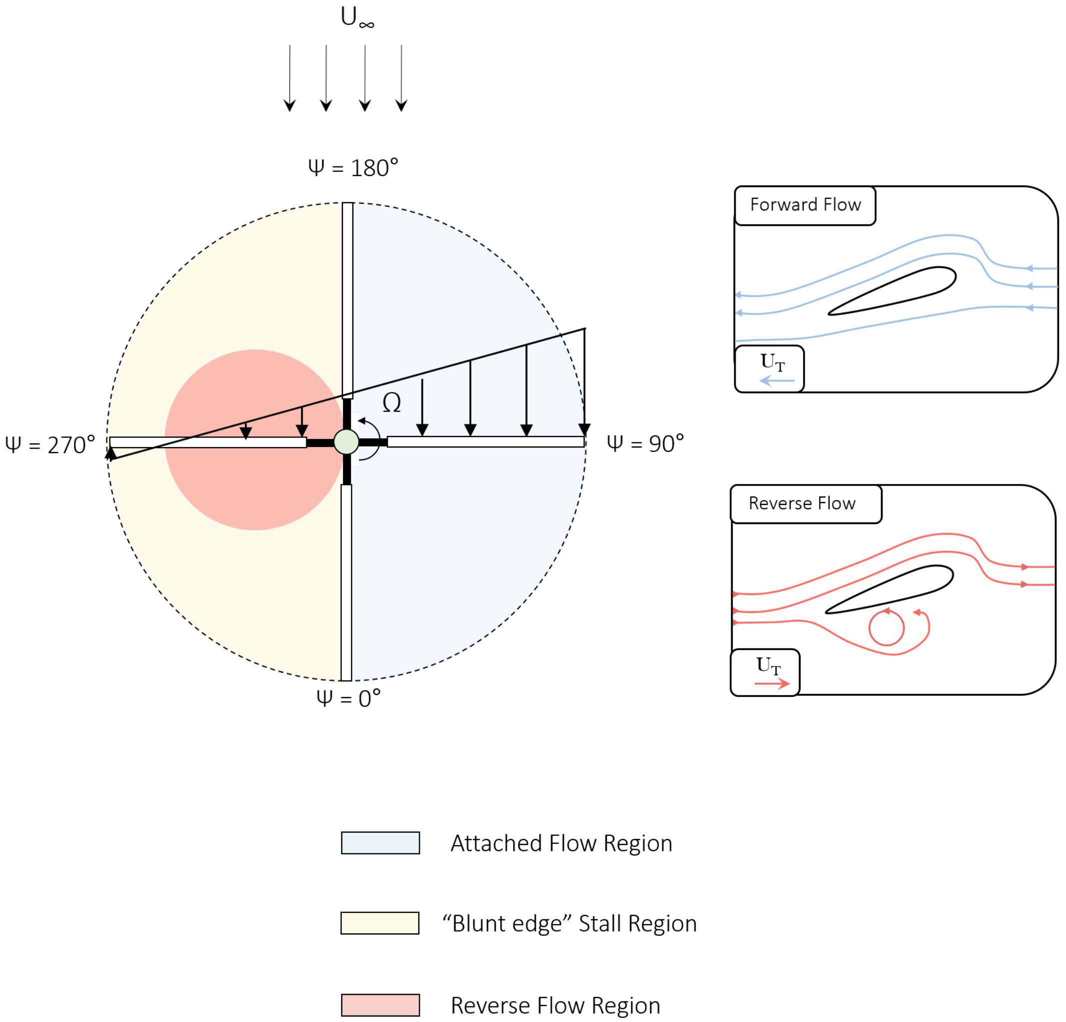

Figure 1.3: Top-down view of a “slowed rotor” helicopter operating in forward flight at high advance ratio.

to the sharp aerodynamic leading edge, and (2) the forward flow stall region on its retreating side (yellow in figure 1.3), where separation occurs about the blunt-edge of the blade due to high local incidence. When such a large region of the rotor disk is at significant risk for flow separation, the performance and blade loads of the helicopter become rather difficult to predict, and modern rotorcraft design codes remain unable to accurately capture the physics of the flow separation that plagues these high advance ratio designs.

1.2 Problem Statement

The current work is aimed at characterizing, understanding, and ultimately modeling the separated flow found on rotors operating at high advance ratio, or designs where the reverse flow region occupies a significant portion of the rotor's retreating side. This study addresses both the "sharp-edge" flow separation typical of the reverse flow region, and the "blunt-edge" flow separation expected of the forward flow stall region. Figure 1.4 provides a more specific illustration of the blade kinematics and flow regimes that will be investigated in the following sections. This figure shows the local freestream velocity (U_T), pitch input (θ), and local spanwise flow (U_Z) experienced by an element of a rotor blade as it revolves about the hub at a sample high advance ratio condition. This thesis is thus concerned with the flow over a conventional airfoil, with rounded leading edge and sharp trailing edge, subject to a large oscillation in local freestream, pitch angle, spanwise flow, and 3-D rotational effects. Flow separation is expected to occur about the sharp trailing

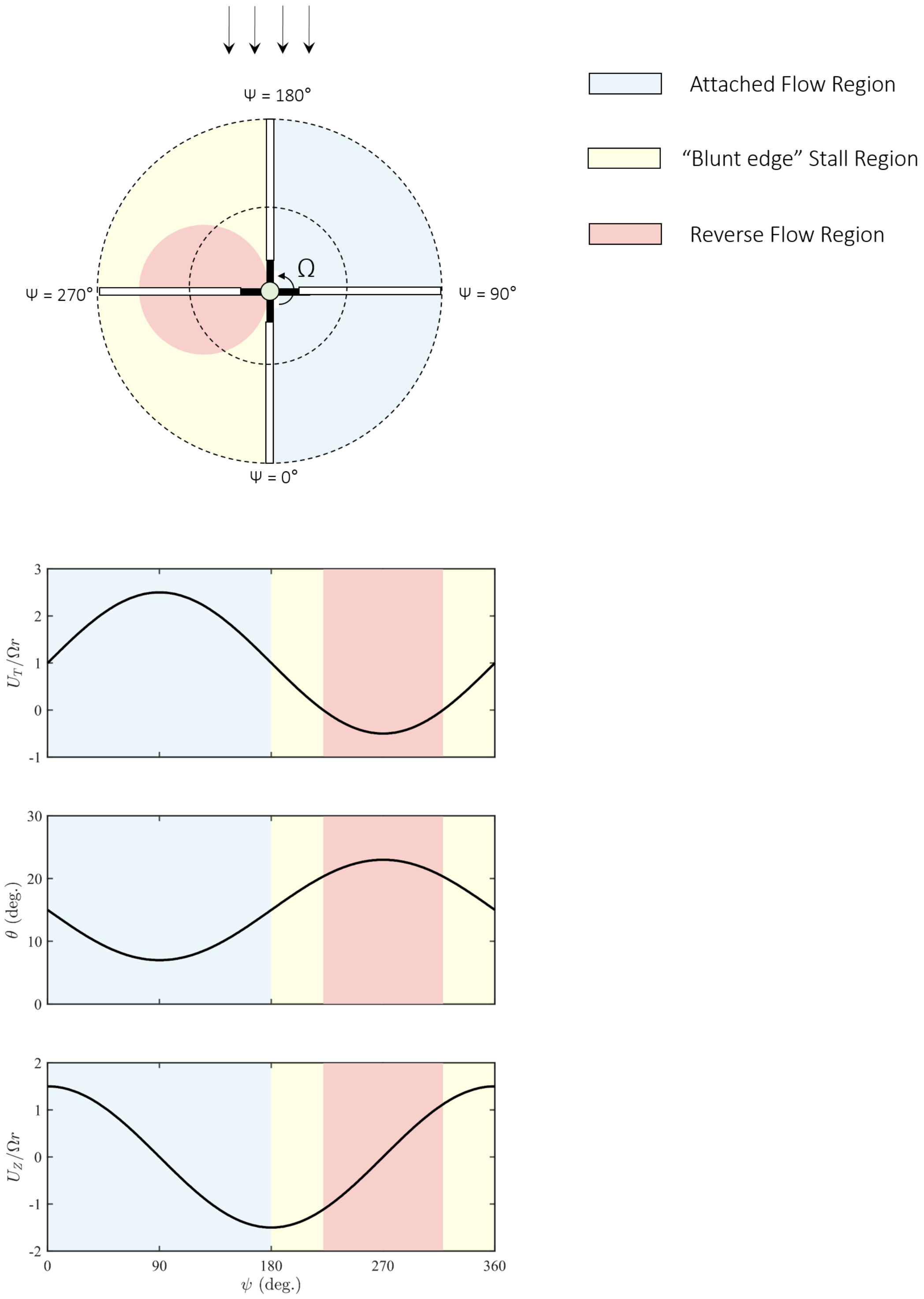

Figure 1.4: Sample kinematics of a rotor blade element at high advance ratio, showing the high amplitude freestream, pitch, and spanwise flow oscillation (adapted from the rotor system described in reference [8]).

edge in the reverse flow region, highlighted in red in figure 1.4, and about the blunt leading edge of the blade in the forward flow, pitch-up region, which is highlighted in yellow.

The following sections will detail the state of the art in both rotor testing and flow separation modeling, with a specific emphasis on why existing models are insufficient, before outlining the mixed experimental and numerical approach taken by the current research study.

1.3 Background

1.3.1 Rotor Experiments

Industry interest in high advance ratio flight has been spurred by recent progress in variable-speed transmissions [9] and blade resonance properties [10], but it is important to keep in mind that the concept of a high advance ratio, slowed rotor is not new. In fact, a full-scale technology demonstrator, the coaxial Sikorsky XH-59A, flew using a slowed rotor at high advance ratios as far back as 1973. The project was shelved due to structural issues, namely high vibration levels [11] and performance limitations [12], but it nonetheless demonstrates how long this technology has been on the mind of the rotorcraft design community. There are thus several examples of high advance ratio rotor testing in the literature that lay the groundwork for the flow separation problems addressed in the present study.

Early published experiments on rotors at high advance ratio, dating back to the 1930's, were primarily concerned with improving the understanding of rotary wings in general and validating basic control concepts. This includes the autogiro experiments of Wheatley and Hood [13], who tested the rotor of the Pitcairn PCA-2 autogiro up to an advance ratio of $\mu = 0.70$, and the rotor campaign of Meyer and Falabella [14], who addressed the blade loads of a sub-scale rotor at advance ratios up to $\mu = 1.0$. Meyer and Falabella, in particular, made important progress in their use of on-board pressure ports; the authors employed a novel surface pressure measurement technique to assess whether a 13% change in hinge offset could mitigate the effect of forward flow stall on the retreating blade. Neither of these experimental campaigns, however, featured rotor designs representative of modern or next-generation aircraft. The autogiro of reference [13] was unpowered, and the sub-scale rotor of reference [14] featured no mechanism for blade feathering, meaning Meyer and Falabella failed to capture the cyclic pitch control characteristic of conventional rotorcraft.

A more modern approach to high advance ratio rotor testing, and in turn a successful identification of many of the issues that still plague designs in this regime, was undertaken throughout 1960's and 1970's. Sweet et al. [15] and Jenkins [16] completed an extensive experimental campaign on a 15 ft teetering rotor in the NASA Langely full-scale tunnel, recording performance metrics (thrust, torque, drag, and control inputs) over a wide range of advance ratios ($0.65 \leq \mu \leq 1.45$). The authors were among the first to observe collective thrust reversal at high advance ratio, wherein an increase in the rotor collective leads to a decrease in thrust (possibly due to lift losses in reverse flow [17]); they also noted a significant discrepancy between the measured rotor drag and what was predicted by attached flow blade-element theory. A similar experimental campaign was performed in the NASA Ames 40 x 80 ft wind-tunnel [18] and uncovered a similar result. That is, rotor drag was consistently under-predicted compared to attached flow theory when operating at $\mu > 0.50$, and the equivalent flat plate area of the rotor was erroneously predicted by roughly 20% [19]. These observations all point to the likelihood of flow separation at high advance ratio, but it was difficult to comment on the aerodynamics of a high advance ratio rotor without more involved blade load measurements or flow visualization.

As part of the broader UH-60 airloads program [21], Datta, Yeo, and Norman made a significant step forward by providing detailed blade load measurements sorely missing from previous test campaigns [20]. The authors performed a series of tests on the full-scale blades ($R = 26.83$ ft) of the UH-60A rotor in a 40 ft x 80 ft wind-tunnel facility (figure 1.5(a)) and collected an expansive set of steady hub loads, dynamic blade loads, and surface pressure measurements over a range of advance ratios ($0.30 \leq \mu \leq 1.0$) and thrust conditions. Their ensuing analysis outlined the basic aeromechanics of a rotor at high advance ratio and identified a number of dynamic phenomena that explain the limitations of conventional theories in predicting rotor performance in this regime. The key observations of the UH-60 tests can be summarized as follows:

1. The rotor required a large longitudinal cyclic (θ_{1s}) to achieve trim at high advance ratio, meaning the blade incidence was very high on the retreating side of the rotor and very low on the advancing side.

(a) The UH-60A rotor system installed in the National Full-scale Aerodynamics Complex (NFAC) 80 ft x 40 ft wind tunnel.

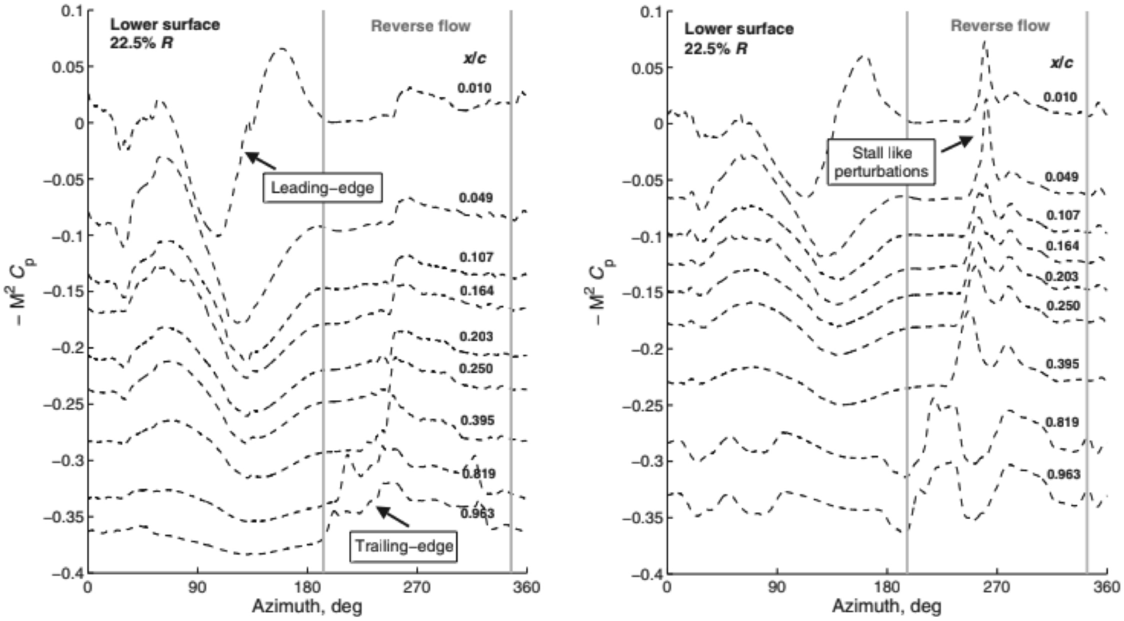

(b) Surface pressure measurements for $r/R = 0.225$ at $\mu = 1.0$ and a collective of 2°.

(c) Surface pressure measurements for $r/R = 0.225$ at $\mu = 0.8$ and a collective of 8°.

Figure 1.5: Sample photographs and results from the UH-60 "slowed rotor" experiments [20].

2. Surface pressure measurements for high advance ratio cases ($\mu = 0.80$ and $\mu = 1.0$) indicated the presence of a phenomenon called "reverse chord stall" in the reverse flow region. The term "reverse chord stall" describes an event wherein a vortex rolls up about the sharp-edge of the rotor blade and convects toward the leading edge as the blade passes through reverse flow. The signature of this vortex and its ensuing convection along the blade chord are evident at both low and high collective in figure 1.5(b) and figure 1.5(c).

3. The presence of "reverse chord stall" is believed to be responsible for an impulsive torsional moment as the blade passes through the reverse flow region. This torsional moment results in a large pitch link load, a potential source for blade fatigue, and plays a part in the excitation of high elastic twist along the blade, which in turn dramatically increases its flap bending moment.

The main takeaway of these high advance ratio tests, then, was that a transient flow separation process, specifically the formation of a vortex about the sharp edge of a rotor blade in reverse flow, appears to drive the dynamic loading of each blade at high advance ratio. The accuracy of any performance or blade loading prediction is thus highly dependent on its ability to predict the onset of flow separation and the unsteady flow structure that results.

Berry and Chopra expanded the parameter space of the UH-60 tests, albeit at smaller scale, with a number of experimental campaigns aimed at trimming a set of un-twisted, un-tapered rotor blades at advance ratios above $\mu = 1.0$ [17, 22, 23]. Collectively, these campaigns represent the widest variety of data types of any test considered thus far, and provide a reliable bank of unsteady blade loads, pressure measurements, and vibratory hub loads for a broad range of advance ratios ($0.30 \leq \mu \leq 1.6$) and collectives ($-10^\circ \leq \theta_0 \leq 11^\circ$). The authors' analysis was primarily focused on identifying the onset of collective thrust reversal, wherein the rotor can no longer be reliably controlled via a change in collective pitch, but their surface pressure measurements also provide an insightful look at how the "reverse chord stall" phenomenon changes over a sweep of advance ratios and collectives. A spike in surface pressure was again identified at high advance ratio and attributed to a coherent, transient vortex structure, as opposed to the chaotic vortex shedding characteristic of static stall. The authors also concluded that the severity of the "reverse chord vortex," and its corresponding impact on the rotor dynamics, increased with both advance ratio and collective.

More recent experimental studies have shifted focus from the dynamic behavior of the blades to the separated flow structures that dominate aerodynamic loading at high advance ratio. These include the two-component flowfield measurements of Lind et al. [24], who investigated reverse flow on the same rotor system used by Berry and Chopra, and the three-component, "stereoscopic" measurements of Hiremath et al [25, 26], who tested a sub-scale teetering rotor up to $\mu = 1.0$. Both campaigns confirmed the presence of a large vortex located at the sharp edge of the rotor blade in reverse flow and quantified the strength of this vortex over a sweep of advance ratios. Lind et al. also identified the presence of a second flow structure located near the blunt edge of the rotor blade. Figure 1.6 shows a snapshot of the vortices at the sharp and blunt edges, called the "reverse flow dynamic stall

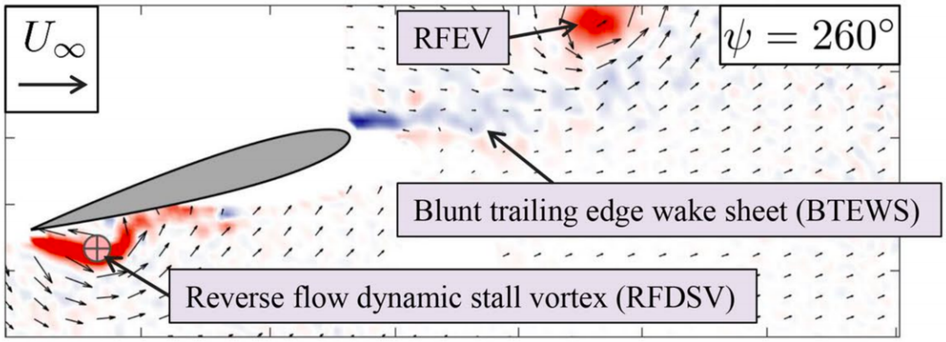

Figure 1.6: Phase-averaged vorticity field of a rotor blade element in reverse flow at $\mu = 0.60$ and $\theta_0 = 10°$ [24].

vortex" and the "reverse flow entrance vortex" (RFEV), respectively, as a sample blade element passed through reverse flow at $\mu = 0.60$. The presence of two distinct flow structures appeared to imply that vortices form both prior to and during the blade's passage through reverse flow, and illustrates the extent to which unsteady, separated flow dominates the entire retreating side of a rotor at high advance ratio. The specific physics of each flow structure, however, could not be ascertained from these experimental measurements, which were limited to a single radial station. It remains to be seen how the 2-D and 3-D mechanisms of the flowfield interact in the development of the vortex at the sharp and blunt edge of the blade.

All together, the preceding works demonstrate that flow separation is widespread when a rotor operates at high advance ratio, especially in the reverse flow region. A number of coherent flow structures, particularly a vortex that forms at the sharp edge of the blade, have been visualized through experimental flowfield measurements and evaluated in relation to their effect on blade dynamics. The next section will provide specific details on how these flow structures have been modeled in rotor analysis, and will explain why conventional models are inherently limited in their ability to capture the aerodynamic effects discussed above.

1.3.2 Conventional Methods for Modeling Unsteady Flows

The unsteady flow over an airfoil has been the subject of a rich, expansive body of research in the context of rotorcraft aerodynamics. Historically, the ultimate goal has been to arrive at a low-order, or computationally inexpensive, model for use in comprehensive rotorcraft analysis and design, a process that requires the quick prediction of blade loads across a wide sweep of design iterations. This section will describe the conventional low-order methods used to compute the aerodynamic forces on an airfoil in the context of rotorcraft design, and will assess their shortcomings when it comes to modeling the separated flow on a rotor at high advance ratio.

1.3.2.1 Table Lookup

The simplest and perhaps most popular method of predicting aerodynamic forces on rotors involves the incorporation of static lift and drag measurements. In this method, a rotor blade is discretized into a certain number of blade elements, and the local angle of attack for each element is calculated based on the geometric pitch, torsion, and inflow. The relevant aerodynamic forces are then interpolated from published experimental results for the specific airfoil section, Reynolds number, and angle of attack.

The table lookup method is well-suited to environments dominated by quasi-steady mechanisms of force generation, but begins to fail in cases with appreciable unsteady effects or flow separation. Floros and Johnson [27], Kottapalli [28], and Bowen-Davies and Chopra [29] all employed the table lookup method in attempting to validate comprehensive analysis codes against well-known high advance ratio rotor tests. Although each campaign was able to capture the general trend in rotor thrust, all three significantly either under-predicted or over-predicted the performance of the rotor at high advance ratios and high collectives. The inaccuracy was attributed to uncertainties in the reverse flow region specifically. Such a limitation makes intuitive sense; the forces generated by a rotor blade-element undergoing a transient flow separation process are much different than the time-averaged forces at the same angle of attack. The table lookup method, although certainly useful for less aggressive flight conditions, does not appear particularly well-suited to the flow separation characteristic of high advance ratio flight due to its neglect of any unsteady contributions to the force.

1.3.2.2 Linear Unsteady Theories

An alternative procedure is to employ the classical models of unsteady thin airfoil theory. In this method, the rotor blade is again discretized into a finite number of blade elements, but the blade angle of attack is now fed into a lift-deficiency function that accounts for both its current angle of attack and a time-history of its motion. These models include Theodorsen's theory, which addresses a sinusoidally pitching wing in uniform freestream [30]; Sears' function, which addresses a wing undergoing an oscillation in freestream [31]; and Greenberg's model, which combines the effects of an oscillating freestream and an oscillating pitch angle into a single closed-form equation [32]. Together, these foundational theories are able to account for a number of unsteady effects, including the non-circulatory force associated with the blade motion and the circulatory force due to the trailing wake, that cannot be captured from conventional thin airfoil theory or static force measurements. Each model, however, operates under the often limiting assumptions of attached flow, small-amplitude oscillations, and a sinusoidal planar wake.

The large amount of separated flow found on rotors at high advance ratio unfortunately makes these classical unsteady theories an inaccurate option. Yeo and Johnson, for example, accounted for the impact of linear unsteady effects in their correlation of rotor performance at high advance ratio, but again under-predicted the power required at higher thrust conditions [33]. Granlund et al. [34] and Kirk and Jones [35] both attempted to simplify the problem, testing a NACA 0012 airfoil under conditions representative of a blade element on a high advance ratio rotor, but observed a severe under-prediction of the forces generated at high angle of attack. The transient aspects of flow separation at high advance ratio, or more specifically the formation of a vortex at both the blunt and sharp edges of the blade, appear to impart a significant enough effect that the classical linear theories of unsteady aerodynamics are no longer valid.

1.3.2.3 Dynamic Stall Models

The final category of conventional aerodynamic force prediction consists of the semi-empirical models of dynamic stall. These models were developed based on the insights gained from "classical" dynamic stall experiments, wherein the motion of a rotor blade in forward flight is simplified to a pitching airfoil in a uniform freestream [36, 37, 38, 39, 40, 41], and include the well-known Leishman-Beddoes [42] and ONERA methods [43]. Dynamic stall models have the major advantage of accounting for the effects of flow separation and vortex formation on an airfoil in an unsteady flow, and contain additional corrections for the presence of non-circulatory pitch rate effects and a trailing wake. They do not, however, include any way of addressing the impact of an unsteady freestream velocity, and the heavy reliance of these models on experimental data makes them limited in their range of applicability.

Figure 1.7 provides an example of the forces predicted by the Leishman-Beddoes dynamic stall model in comparison with the measured lift, drag, and pitching moment of an oscillating Sikorsky SC-1095 airfoil (left column) and a Hughes HH-02 airfoil (right column). In each subfigure, the time-history of the airfoil's angle of attack is plotted on the abscissa, and the instantaneous aerodynamic force coefficient is plotted on the ordinate. Figure 1.7 demonstrates that the Leishman-Beddoes method is able to very reasonably re-create the trends and magnitude of the aerodynamic forces on a pitching airfoil under conditions that involve flow separation. The maximum lift coefficient (top row), which far exceeds what is achieved by a

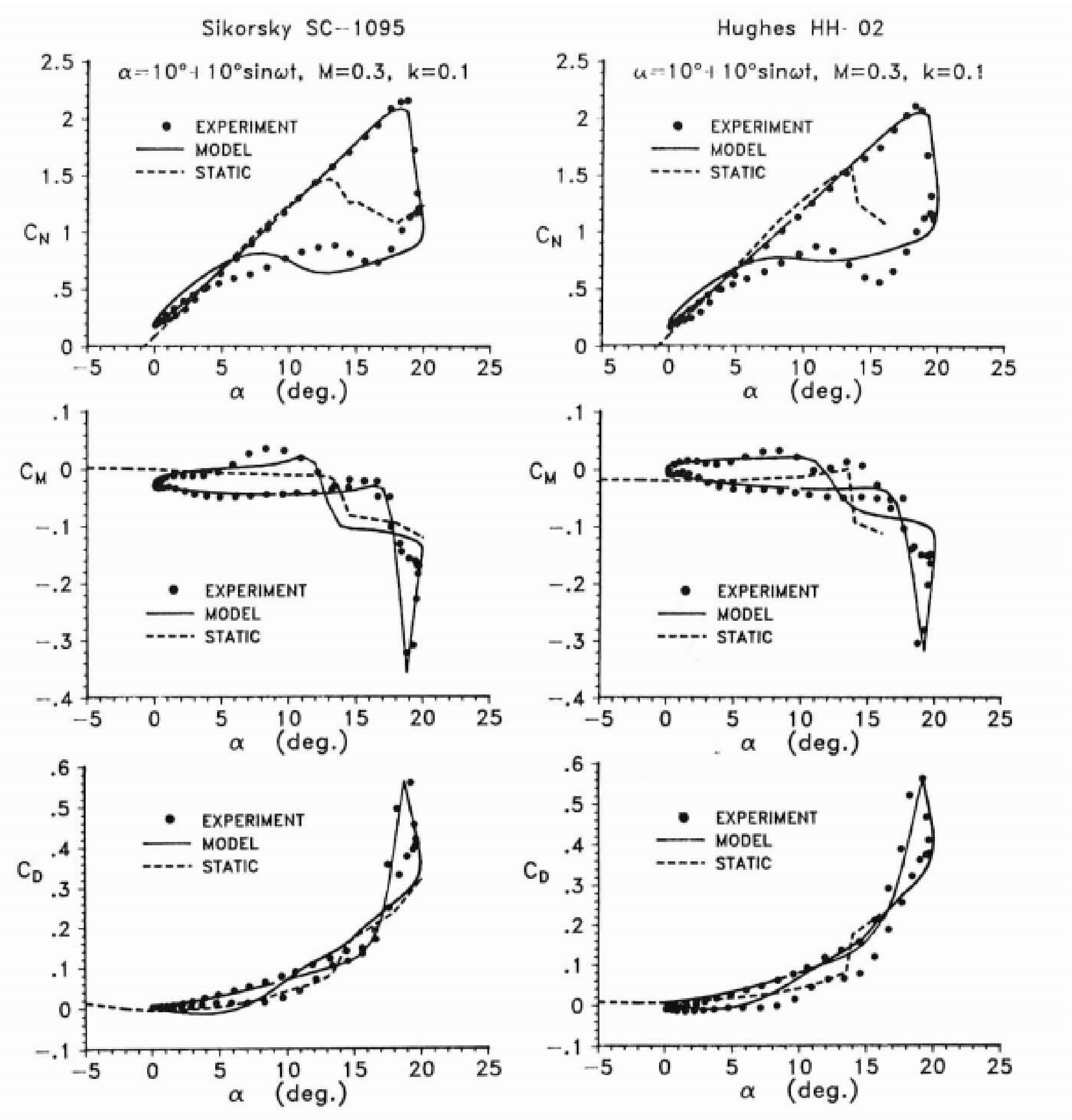

Figure 1.7: The aerodynamic forces predicted by the Leishman-Beddoes dynamic stall model compared with experimental measurement for two airfoils undergoing a pitch oscillation [42].

static airfoil, is well-resolved in figure 1.7, and the lift hysteresis loop has reasonably low error, even during the flow reattachment phase.

The major drawback of dynamic stall models, including the Leishman-Beddoes method shown in figure 1.7, is that they involve dozens of empirical parameters that can only be ascertained from experimental measurement. The best way to demonstrate this idea is through example. Consider the Leishman-Beddoes formulation for the increment in normal force due to the rollup of a vortex at the edge of a wing (C_V^N). This expression is written according to equation 1.1 and could, in theory, be used to predict the impact of the "sharp-edge vortex" that forms in reverse flow:

$$C_V^N = C_V^N\Big(s - \Delta s\Big)e^{\frac{-\Delta s}{T_V}} + \Big[C_V(s) - C_V(s - \Delta s)\Big]e^{\frac{-\Delta s}{2T_V}}. \tag{1.1}$$

In equation 1.1, s denotes the current non-dimensional time in the airfoil motion profile; C_V is a function of the instantaneous "attached flow" solution; and T_V is an empirical time constant determined from the behavior of the vortex. The general form of equation 1.1, like many others employed in dynamic stall modeling, is based on the indicial response of an airfoil to a step change in angle of attack, solved via Duhamel's integral, and similar to the well-known indicial models of Küssner [44] and Wagner [45].

The top-level physical principles behind equation 1.1 are actually quite sound. That is, the instantaneous contribution of vortex lift is coupled both to a time-history of its strength (first term on the right hand side) and the instantaneous potential flow solution near the leading edge (second term on the right hand side).

Equation 1.1 in turn captures the nonlinear relationship between the strength of a leading edge vortex, its growth rate, and the flow at the leading edge of the airfoil. The main problem arises when we consider the implementation of the time constant T_V. Mathematically, T_V controls the rate at which the influence of the vortex decays over time, a flow property that depends on both diffusion and the convection of the vortex away from the surface of the wing. Leishman and Beddoes estimated T_V based on experimental measurements of vortex convection on pitching airfoils, but one cannot assume that their function applies to vortex convection for any arbitrary airfoil or motion profile. In cases with a large variance in the local freestream, for instance, the convection behavior of a vortex is expected to be quite different than that of a pitching wing in a uniform freestream, and thus the validity of equation 1.1 becomes questionable.

The issues discussed above are not limited to the case of vortex convection. Time constants and empirical deficiency functions play a role in the determination of the attached flow solution, the time-history of the separation point, and the unsteady features of the boundary layer in the Leishman Beddoes model (and in indicial dynamic stall calculations in general). In regard to high advance ratio conditions, none of these empirical parameters have been extensively assessed or validated for an airfoil in reverse flow. A number of more fundamental, 2-D experiments have been undertaken from which the empirical constants could be ascertained [46, 47], but this would still not account for the large local freestream variations seen at high advance ratio, for which conventional dynamic stall models do not have a method of including.

Our main takeaway then is that dynamic stall models are quite useful for cases of separated flow where the blade pitching motion is the dominant unsteady feature, but would require a substantial reworking (and experimental evaluation) in order to be applicable to the large reverse flow region of a rotor at high advance ratio. As we will see later on, the general approach of the current work is to deviate from the conventional framework of dynamic stall models, and instead adopt a more physics-based philosophy that limits the number of empirical parameters at play.

1.3.3 Discrete Vortex Methods

One of the major assertions of the current work is that the discrete vortex methods, a class of models that takes a more first-principles approach to the topic of separated flow, are a viable alternative to the conventional methods of aerodynamics force computation in the design of high advance ratio rotorcraft. Rather than finding deficiency functions for effect of unsteady aerodynamics, discrete vortex methods attempt to model the unsteady flowfield itself, typically representing an airfoil and its wake with a series of vortex particles, and are thus more widely applicable than the empirically-driven dynamic stall models. Discrete vortex methods have seen a resurgence in recent years due to their success in modeling the separated flow about surging, pitching, and rotating wings at low Reynolds number [48, 49, 50, 51, 52, 53, 54, 55], and advances in computational efficiency make them an increasingly viable option for rotor airload calculation [56, 57, 58].

The fundamental conceit of a discrete vortex method is that the separated

(a) Discrete vortex method. (b) Experimental dye flow visualization.

Figure 1.8: Illustration of the use of a discrete vortex method in predicting the separated flow over a pitching flat plate [59].

flow over an airfoil can be modeled using a linear superposition of potential flows. The term “potential flows” refers to a subset of elementary flows, including the ideal source, doublet, and vortex, that satisfy the conservation of mass equation under the assumption of incompressible, inviscid (zero viscosity), and irrotational (zero vorticity) flow. These elementary flows themselves cannot account for viscous effects, such as boundary layer flow and separation, but a strategic placement of potential flows can very much simulate the large-scale flow structures that result from a transient flow separation procedure. Figure 1.8 provides a simple qualitative example of how a discrete vortex method can be used to predict the separated flow over a flat plate at high incidence [59]. By placing an ideal vortex at each of the sharp edges of the plate, then allowing the vortices to convect over time, the discrete vortex method (left) is able to closely approximate the flow structure in the plate’s wake, evidenced by a qualitative comparison with dye flow visualization (right).

The basic blueprint for a discrete vortex method consists of three parts: enforcing the flow tangency condition, modeling the wake, and accounting for the boundary layer. The following subsections will address each of these components individually to give the reader a sense of how a discrete vortex method functions, and to demonstrate how they capture the structure of a separated flow with minimal computational expense.

1.3.3.1 Flow Tangency

The first component of the discrete vortex method is a representation of the aerodynamic body of interest, or some way of enforcing the flow tangency condition (also called the "no through-flow condition") along the surface of a wing. Methods of body representation include conformal mapping, wherein the flow over a cylinder is transformed to that over a plate or airfoil [7, 60]; the use of basis functions, wherein the airfoil is modeled as an infinite series [61, 62]; and the panel methods, wherein the bound vorticity on an airfoil is approximated in discrete segments [63, 64, 65].

Of these three methods, the panel approach is the most versatile, and perhaps the best suited to rotor design applications. At the small expense of requiring a 1-D mesh, a panel method can represent any arbitrarily complex airfoil geometry and offers a simple framework for the incorporation of flow separation and vortex shedding. The panel method functions by assigning a vortex sheet (or "lumped" bound vortex) to each panel, then solving for the strength of that vortex sheet by enforcing flow tangency at discrete points along the airfoil surface. One can improve the fidelity of a panel method by assuming a linear or parabolic distribution of vorticity along each panel [66], or by incorporating a source distribution to explicitly account for the non-circulatory forces acting on the airfoil [67]. The modeling portion of this thesis will make frequent use of a simple “lumped” vortex model (i.e., a 2-D, first order panel method) in predicting flow separation on a rotor blade element at high advance ratio.

1.3.3.2 Modeling the Wake

The second component of a discrete vortex method is the representation of the airfoil’s trailing wake. The trailing wake is one of the key unsteady flow features that contributes to the delay in separation seen on a dynamically pitching airfoil, and its presence can also play a significant part in the rate at which separated flow structures grow and convect.

Early panel methods adopted a vortex sheet approach to modeling the trailing wake, extending the bound vorticity distribution of the airfoil along a prescribed path beyond its trailing edge [68], but the far more popular approach has been to discretize the wake into a finite number of vortex particles that convect in time. The fidelity with which this task is accomplished largely depends on the application of interest. The high-fidelity vortex methods, for instance, discretize the entire flow domain into a series of vorticity “blobs” (or rotational vortices with a finite, typically Gaussian core) and allow each blob to convect, diffuse, and distort in time [69, 70]. The lower order version of the vortex method, in contrast, limits the number of vortices in the flow domain and typically confines them to regions where a high concentration is expected. Most modern low order methods simply shed one vortex from the trailing edge an airfoil per time step, and keep the strength of those vortices constant over the course of the airfoil's motion [48, 71]. The strength of each wake vortex is determined by enforcing the Kutta condition at the sharp edge of the airfoil.

1.3.3.3 The Boundary Layer

The final component of the discrete vortex method is a treatment of the boundary layer at the surface of the airfoil. In the context of separated flows, the purpose of including the boundary layer is typically to identify the timing and location of the separation point, such that the unsteady vortex structures that result from separation can be properly resolved. Because the flow in the boundary layer is rotational, the governing fluid equations are numerically expensive, and it can become quite difficult to find a method that provides a suitable mix of accuracy and computational efficiency. There are thus many approaches that couple an inviscid flow solver (such as a panel method) with a viscous treatment of the boundary layer, all of various fidelity and efficiency.

The most rudimentary approach is to simply neglect the presence of the boundary layer entirely. In this method, the flow is assumed either assumed to be completely attached, or the separation point is set a priori from experimental measurement. Figure 1.9, taken from reference [54], serves as an example of the latter. This figure shows the flow of an accelerating flat plate as calculated by a discrete vortex method (top) that exhibits close qualitative agreement with experimental vorticity fields (bottom). Here, separation was assumed to occur at the leading edge of the

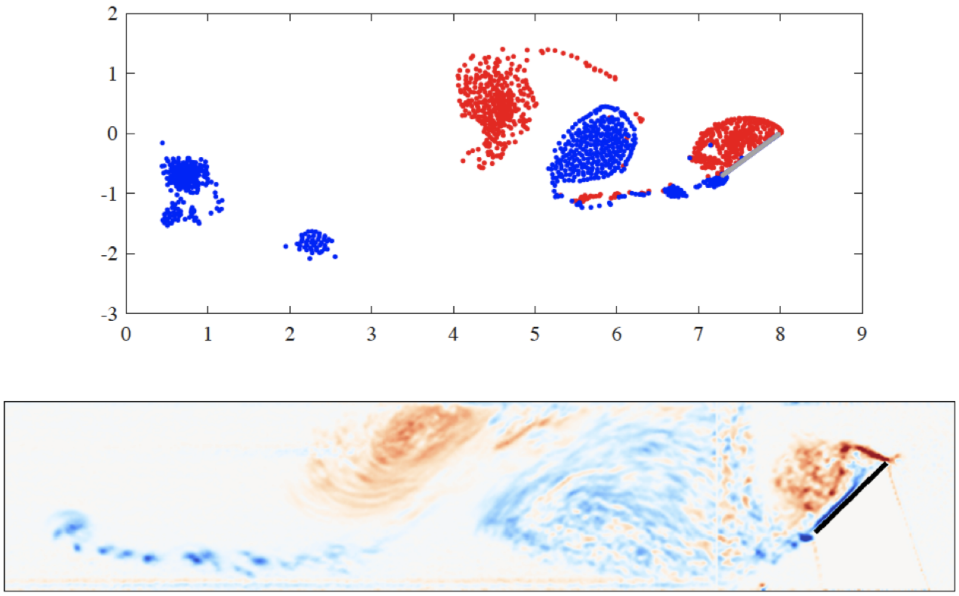

Figure 1.9: Discrete vortex model with leading edge shedding (top) compared to the vorticity field of an accelerating flat plate (bottom). In each subfigure, the plate is translating left-to-right at high incidence [54].

plate at all times throughout the simulation, and new vortices were shed from this location at each time step. For cases where the separation point is known, this approach is quite straightforward, and only sacrifices the computation of skin friction drag, which is not expected to be significant in a massively separated flow.

For cases with intermittent shedding, or where the properties of the separation point are not known beforehand, some acknowledgement of the boundary layer must be incorporated into the discrete vortex method. This usually manifests as an additional (or simultaneous) “viscous” calculation performed at each time step; one can extract the “slip” velocity at the airfoil surface from the panel method solution and use this velocity as a boundary condition for the laminar boundary layer equations. Although conceptually straightforward, the boundary layer equations, even in their 2-D laminar form, do not admit an analytic solution for an airfoil flow, and generally require some simplifying assumptions to be solved numerically. By far the most popular lower-order numerical approach is to consider an integrated form of the boundary layer equations known as the von Karman integral relations:

$$\frac{1}{\rho}\tau_w = \frac{\partial}{\partial t}\Big(U_e\delta_1\Big) + \frac{\partial}{\partial x}\Big(U_e^2\delta_2\Big) + U_e\Big(\frac{\partial U_e}{\partial x}\Big)\delta_1, \tag{1.2}$$

where x is directed along the surface of the airfoil; U_e is the exterior velocity of the boundary layer (taken from the inviscid solution); τ_w is the local shear stress at the wall; and δ_1 and δ_2 are the displacement and momentum thickness, both of which are functions of the local boundary layer profile.

The procedure for solving equation 1.2 involves (1) assuming a non-dimensional family of boundary layer profiles, (2) evaluating τ_w, δ_1, and δ_2 in terms of the non-dimensional parameters associated with this boundary layer profile, and (3) solving the resulting differential equation for the boundary layer height δ. The boundary layer height, or a non-dimensional version of it, can then be used to determine the local shear stress along the airfoil and thus the point of separation. The well-known methods of Pohlhausen [72] and Thwaites [73] both employ the methodology described above, and have provided reasonable predictions of the separation point on airfoils in the laminar regime. Over the years, various amendments to the basic integral boundary layer formulation have included the incorporation of empirical turbulence models [74], coupling of equation 1.2 with an integral energy equation [75], and overcoming the “Goldstein” singularity known to occur at the point of separation in the boundary layer equations [76].

The integral methods are now at the point where they can solve for the separated flow over an airfoil with an interacting boundary layer [77, 78], but in their most general form, they become somewhat computationally involved, especially in the unsteady case. A more recent approach is to reduce the order of the boundary layer calculation step based on physical observation from experiment as a way of quickly predicting the onset of flow separation. The foundational principle of these methods is that the onset of separation is a function of the inviscid properties of the flow, the shape of the airfoil, and the freestream Reynolds number; a "critical" separation parameter, based only on the inviscid properties of the flow, can then be obtained from experiment for any Reynolds number-airfoil combination. Such is the operating principle behind the leading edge suction parameter (LESP). An LESP-based method still computes the evolution of a separated flow with a discrete vortex framework, but replaces the boundary layer step with an empirical criterion based on the inviscid properties of the flow near the leading edge. The LESP has proven to be quite useful in modeling intermittent vortex shedding on surging, pitching, and plunging wings [59, 79, 80, 81], but its physical relation to the properties of the boundary layer is still an open research question.

1.3.3.4 Application to Rotorcraft

At this point, let us take a step back and consider the advantages of the discrete vortex method compared to the conventional methods of calculating the aerodynamics of rotor blades. For a 2-D blade element, the discrete vortex method is capable of capturing non-circulatory effects, deformation of the trailing wake, and the coherent flow structures that form due to separation; each of these features make them more versatile than the table lookup and "attached" unsteady methods. Compared to the dynamic stall models, the discrete vortex method is capable of predicting the growth and convection of vortical structures without using a single empirical parameter, provided that the separation point is known beforehand (or estimated from boundary layer analysis). These features make the discrete vortex method a promising alternative to traditional low-order unsteady models, and advances in computational efficiency make them increasingly viable for use in comprehensive codes.

A few works have gone as far as to predict flow separation phenomenon on rotors using an inviscid-viscous coupling procedure [82, 83]. These simulations have proven to be quite capable in estimating the various stages of dynamic stall, or flow separation about the blunt-edge of a rotor blade. The methods employed in these works are too computationally expense for direct incorporation into rotorcraft design procedures, but their basic framework, wherein the inviscid and viscous aspects of the flow are largely treated separately, allow for a straightforward reduction of order. Later in this thesis, it will become a major goal to reduce the order of a discrete vortex model to the point that it could be employed as a rotorcraft a design tool, a step that requires an understanding of the physics of separation at high advance ratio.

1.3.4 CFD-CSD Coupling

The previous methods for modeling separated flow have uniformly taken a low-order, 2-D (or blade-element) approach to the problem of a rotor blade in forward flight. This was driven by the intended application; in rotorcraft design, the ultimate goal is to develop a low-order, widely applicable model that can compute aerodynamic forces quickly, which typically necessitates a "blade-element" style formulation. It is important to keep in mind, however, that the full, three dimensional flowfield of a rotor in forward flight can in fact be well-resolved by high fidelity, volumetric CFD simulations. These methods operate by discretizing the Navier Stokes equations and numerically computing the flow properties in a finite difference or finite volume framework, at the expense of increased computational time. The existing CFD codes employed in rotor applications can account for a number of detailed fluid dynamic effects, including turbulence and 3-D vortex dynamics, with an accuracy that far exceeds any of the methods discussed thus far.

The case of separated flow on a rotor, specifically, has recently been modeled by high-fidelity numerical methods with a very reasonable degree of accuracy. The approach taken by these studies has been to couple high resolution CFD, which functions as a high-order aerodynamics model, with computational structural dynamics (CSD) codes for an estimation of blade motions and deflections. Chaderjian simulated the forward flight conditions of a UH-60 rotor ($\mu = 0.368$) with a loose coupling of a RANS-based Navier Stokes solver and a comprehensive rotor analysis code; the author was able to conduct a detail study on the effect of tip vortex interaction on dynamic stall [84]. Potsdam et al., in a particularly relevant work, attempted to simulate the UH-60 experiments that first identified the “reverse chord vortex” phenomenon at high advance ratio. The authors found good agreement in rotor performance compared to the experimental measurements, and were able to extensively characterize the flow structures present on the rotor at $\mu = 1.0$, including the “sharp-edge” vortex in the reverse flow region, the rotor wake, and interactions between blades [85].

In the context of rotor design, the most limiting aspect of CFD-CSD coupling is the computational time mentioned above. A high-fidelity CFD simulation can take hours or days to complete, even with parallelization and high-speed computing, and the multiple iterations associated with CFD-CSD coupling only delay the process further. At the current stage, the best way to view CFD simulations is as a tool for detailed case studies. Even if CFD remains too computationally expensive for direct integration with design codes, its high spatial and temporal resolution provide an enormous amount of insightful information regarding the physics at play on a rotor at a certain flight condition, and these insights can be used to develop and validate simpler models for design application.

1.4 Scope of the Present Research

The preceding sections have provided an overview of the separated flow structures, and the methods for modeling them, on a conventional rotor operating at high advance ratio. Two coherent vortex structures, one located at the sharp trailing edge of the rotor blade and one at the rounded leading edge, have been identified through experimental flowfield measurement in the literature, but their combined effect has not been sufficiently captured by the existing low-order methods of aerodynamic force computation. The discrete vortex method, a more physics-based model based in potential flow, was proposed as an alternative, but it is unclear whether a 2-D, low-order vortex method can sufficiently capture the physics of flow separation in the three dimensional environment of a rotor at high advance ratio.

The purpose of this thesis is to obtain an understanding of how the various mechanisms at play on a rotor in forward flight, including the unsteady freestream velocity, the dynamic pitching motion, and 3-D rotational effects, impact the evolution of separated flow structures in the high advance ratio regime. The ultimate goal of this understanding is to leverage our insights into the development of a discrete vortex model that contains the dominant physics of vortex formation but is of suitable order for use in rotor design applications. The specific approach taken by the current work consists of the following steps:

1. Collect three-component flowfield measurements, at various advance ratios and radial stations, on a rotor operating in the high advance ratio regime. This step will allow for the identification of 3-D gradients, particularly in the reverse flow region, that have not been thoroughly investigated by previous experimental measurement campaigns [24, 25].

2. Validate a high-fidelity CFD simulation of a rotor at high advance ratio against the experimental flowfield measurements mentioned above. This step will

demonstrate the ability of a RANS-based finite volume method to capture the coherent flow structures on a high advance ratio rotor; the high resolution numerical flowfields can then be used to conduct a more detailed quantitative analysis of these flow structures in three dimensions.

3. Perform a 3-D vorticity transport analysis, similar to the work of Wojcik and Buchholz [86], Panah et al. [87], and Akkala [88], on the numerical flowfields obtained from the CFD simulations. This step will provide insight into the relative role of 2-D and 3-D fluid mechanisms on the evolution of the vortex that forms at the sharp edge of the rotor blade in the reverse flow region. It will also serve as a guide for what mechanisms must be included in an accurate model of this flow structure.

4. Obtain flowfield measurements of the “blunt-edge” vortex that forms about the rounded edge of a pitching airfoil subject to an unsteady freestream velocity. This step will specifically address the physics of the “entrance vortex” seen in the measurements of Lind et al. [24], and will provide insight into how a large-amplitude freestream oscillation changes the conventional understanding of dynamic stall.

5. Leverage the lessons learned from (a) the CFD simulations and (b) the unsteady freestream experiments into a discrete vortex method that captures the primary separated flow structures of a rotor at high advance ratio. This model is intended to capture both the vortex at the sharp edge of the blade (or the structure responsible for “reverse chord stall”) and the vortex at the

blunt edge of the blade (which may have its own unique impact on unsteady blade loading).

The mixed experimental and numerical approach outlined above has been formulated to comprehensively address the behavior of separated flow on a rotor at high advance ratio. It is important to recognize, however, that the current work limits itself to investigating the retreating side of a single edgewise rotor configuration; that is, the conclusions of this thesis are strictly valid for a simplified, representative rotor system, with no twist, taper, or auxiliary wings/propellors. The analysis presented here will attempt to generalize its conclusions as much as possible, but additional research will inevitably be needed to approximate the flowfield of newer high advance ratio designs, such as those with a rounded trailing edge to combat separation in reverse flow. Chapter 6 contains a few recommendations for conducting future work on the 3-D vortex dynamics of a rotor at high advance ratio.

1.5 Dissertation Outline

Chapter 2 provides a brief outline of the experimental and numerical procedures involved in collecting the flowfield measurements investigated here. Chapter 3 presents the basic three dimensional flow structure of the reverse flow region on a high advance ratio rotor, formally identifies the vortex structures of interest, and performs a quantitative comparison of the experimental and numerical data sets. Chapter 4 takes a detailed look at one flow structure, the vortex that forms at the sharp edge of a rotor blade in reverse flow, and attempts to quantify the relative importance of 2-

D and 3-D mechanisms of vorticity transport. The resulting conclusions are used in the development of low-order model of the growth and convection of the sharp-edge vortex. The final analysis chapter, Chapter 5, shift focus to a vortex that forms about the blunt-edge of a rotor blade, and attempts to predict the timing of its formation based on a set of 2-D surging and pitching wing experiments. Chapter 6 summarizes the conclusions and contributions of this thesis, before adding a few suggestions for future work.

Chapter 2: Experimental and Numerical Methods

The ultimate goal of this work is to understand and model the physics of flow separation on a high advance ratio rotor. This chapter will outline three data-acquisition campaigns, two experimental and one numerical, that were undertaken to investigate specific regions of flow separation on a rotor in forward flight. Each campaign was tasked with capturing the flow about a rotor blade-element in forward flight, and their results combine to form a useful database representative of rotorcraft aerodynamics at high advance ratio.

2.1 Measurements on a Rotor in Forward Flight

The previous chapter established that flow separation may occur at multiple locations on a rotor at high advance ratio, but the primary source is believed to be the large region of reverse flow that persists on the rotor's retreating side. Reverse flow has been the subject of a few rather comprehensive airload investigations over the years, but there is still much to be learned regarding the flow physics of this region. Our first data-acquisition campaign was thus aimed at obtaining experimental flow-field measurements of the reverse flow region on a rotor at high advance ratio. The goal here was simply to visualize the features of the flow that may be contributing to the large pitch-link loads incurred in reverse flow [20, 22, 23], and to gain a basic understanding of how those flow features behave with properties of the rotor. Two past studies with similar goals can be found in the literature [24, 25], but the current work distinguishes itself by providing three-component flowfield measurements at multiple advance ratios, radial stations, and azimuthal locations.

The initial step of this experimental campaign was to select a rotor system representative of a high speed, or "slowed," rotor in forward flight. Due to the variance in how rotorcraft operate and control, such an undertaking was not necessarily straightforward. Rotors can be articulated, hingeless, or rigid, with propellors, wings, or even a second rotor augmenting their thrust; it can thus be quite difficult to select a rotor system for study that is broadly applicable to the field of rotorcraft at large. As a fundamental approach to the problem, it was decided to use a simple Mach-scale, articulated rotor system to study the aerodynamics of reverse flow. Although not strictly representative of the more advanced rotor configurations, such as the "lift-offset" coaxial rotor designs, an articulated rotor captures the basic dynamic motion that most rotor blades undergo in forward flight, and represents a good starting point for understanding reverse flow in more complex rotor environments.

The term "articulated" here refers to the way in which rotors introduce a dynamic, or time-dependent, pitch oscillation into the motion of the rotor blades [4]. For reference, the geometric incidence (θ) of a blade on an articulated rotor can be described as a function of azimuthal position (ψ) with the following equation:

$$\theta(\psi) = \theta_0 + \theta_{1s}\sin\psi + \theta_{1c}\cos\psi, \tag{2.1}$$

where θ_0 is a “collective” pitch input independent of azimuthal position, and θ_{1s} and θ_{1c} are “cyclic” pitch inputs that determine the properties of the blade’s pitching oscillation. The cyclic inputs are typically adjusted such that each rotor blade undergoes a pitch-up motion during the “retreating” motion of the blade, where the local freestream velocity is low, and a pitch-down motion during the “advancing” motion of the blade, where the local freestream velocity is high. The dynamic pitching motion of the blades, and the associated flap and lag response, can thus account for the flow asymmetry inherent to a rotor disk in forward flight, and allow a rotor to fly at some desired flight condition while maintaining stable moments about the hub. Depending on the flight condition, however, these unsteady blade motions may become so aggressive that they induce massive flow separation, a problem that becomes particularly troublesome in the reverse flow region.

With this in mind, the following sections will describe the articulated rotor system chosen for study in the current work, and will detail the methods used to visualize the vortical structures present in the reverse flow region of this rotor system as it operates at high advance ratio.

2.1.1 Rotor System

Figure 2.1 shows a photograph of the rotor system that served as the subject of our experimental flowfield study. For our experiments, the rotor was installed in

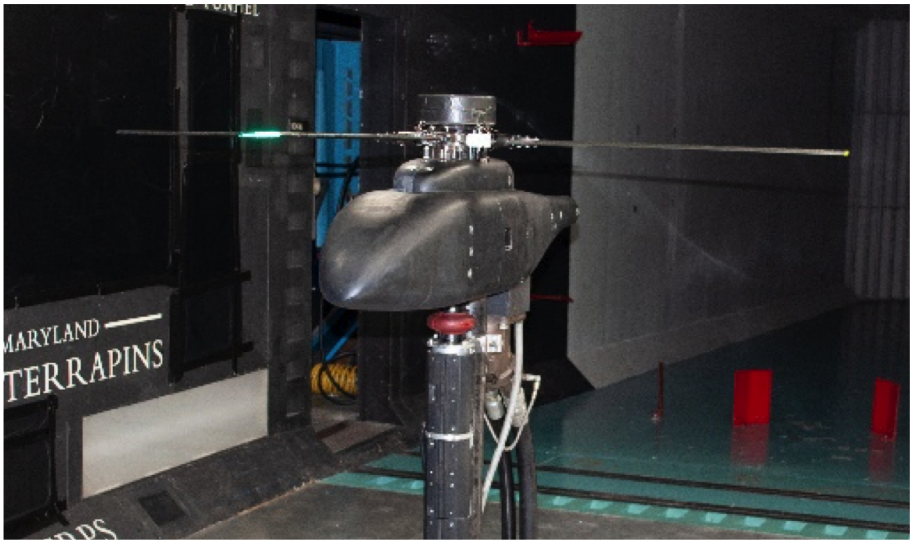

Figure 2.1: Photograph of the rotor system used in our experimental study of the reverse flow region at high advance ratio.

the Glenn L. Martin Wind Tunnel, a closed-circuit wind tunnel with a 3.36 m × 2.36 m test section, and was operated at advance ratios representative of high-speed, or “slowed rotor,” rotorcraft designs. The fabrication, structural properties, and installation procedures associated with this rotor system have been very well-documented throughout previous rotor performance and blade load campaigns [8, 17, 89], so this section will simply highlight the main features and operating procedures associated with the rotor system.

Table 2.1, adapted from reference [8], collects the main geometric properties of the rotor system relevant to the flowfield measurements of the current work. Each of the rotor’s four blades are un-twisted, un-tapered, and outfitted with a uniform NACA 0012 cross-section along the span. The rotor radius is $R = 0.85$ m, and each blade has an aspect ratio of $AR = 10.625$. The four blades were each manufactured to be structurally similar, a feature that ensures that each blade takes the same

Table 2.1: Geometric and structural properties of the rotor system.

Property	Value
No. of Blades	4
Airfoil	NACA 0012
Radius (R)	0.85 m
Chord (c)	0.08 m
Solidity (σ)	0.120
Angular Velocity (Ω)	900 RPM
Lock Number	4.96
Hinge Offset	6.4%
Root Cutout	16.4%

path about the hub, and were shown to exhibit less than 5% variance in their mass properties at the time of testing [8].

A given forward flight condition of the rotor was defined based on the rotor advance ratio (μ) and collective (θ_0). The process for operating our rotor system begins with spinning up the rotor to its nominal angular velocity in hover, then applying the tunnel freestream, before finally increasing the rotor collective to its desired value. The longitudinal (θ_{1s}) and lateral (θ_{1c}) cyclic inputs are then adjusted, or "trimmed," until a stable state of the rotor is achieved. For our experiments, the rotor was trimmed to minimize the first harmonic flap response of the blades ($\beta_{1s} \approx \beta_{1c} \approx 0$), a trim target known as "wind-tunnel trim." This trim target has the distinct advantage of minimizing the blades' flap response, meaning our analysis

Table 2.2: Comparison of our experiments with the design conditions of full-scale high-speed rotor designs.

	μ	M_{adv}	Re_{tip} (approximate)
Current Work	0.80	0.42	5.3×10^5
X2TD	0.82	0.90	9.1×10^5
X^3	0.66	0.85	1.0×10^6

of the reverse flow region can focus on the more fundamental effects of a time-varying pitch and time-varying freestream.

We repeated the trim procedure described above for three forward flight conditions over the range $0.60 \leq \mu \leq 0.80$. For each flight condition, the rotor angular velocity was held constant at $\Omega = 900$ RPM (chosen to approximate the Mach and Reynolds number of a high-speed helicopter as closely as possible without fatiguing the blades), and the collective was held constant at $\theta_0 = 10°$. Table 2.2, partially adapted from reference [24], compares the conditions of our highest advance ratio case ($\mu = 0.80$) with what is experienced on a full-scale helicopter designed for high advance ratio. This table includes properties of the design flight condition for two compound rotorcraft designs, the Sikorsky X2TD [5] and the Eurocopter X^3 [6], that have both successfully flown above 200 knots. A tip Reynolds number was estimated for each rotorcraft design based on its angular velocity, rotor radius, and an assumed chord of $c = 0.10$ m (exact blade geometries were not available). Table 2.2 shows that the advance ratio range considered here is very much representative of these high-speed designs. The tip Reynolds number of the current work is sub-scale compared to the designs in table 2.2, but the evolution of the reverse flow region has been shown to exhibit a weak dependence on Reynolds number, at least for rotor blades with a sharp geometric trailing edge [46].

As a final comment, we must again acknowledge that the pitch motion of our articulated rotor blades is not strictily representative of all high advance ratio rotorcraft designs. Many high-speed helicopters, such as the coaxial X2TD, do not feature blade articulation at all, and those that do are unlikely to cruise at a high collective due to the presence of lift-offset wings and flaps [90]. In this way, our choice of a reasonably high collective ($\theta_0 = 10°$) can be seen as a way of exaggerating the severity of flow separation to make the resulting flow structures more easily identifiable in our experimental measurements. The general behavior of these flow structures is still expected to hold at lower values of collective and blade incidence.

2.1.2 Flowfield Measurements

For each forward flight condition of the rotor, phase-averaged, three-component flowfield measurements were collected at a variety of radial stations over the range $0.30 \leq r/R \leq 0.60$. The purpose of these measurements was to visualize the separated flow in the reverse flow region of the rotor and identify any coherent vortex structures. Our use of a high speed, stereoscopic particle image velocimetry (stereo-PIV) system allowed us to see how the flow evolves over time, while our repetition of the measurements at several radial stations allowed us to see how the flow changes in three dimensions.

Figure 2.2 shows a top-down (figure 2.2(a)) and side view (figure 2.2(b)) of the stereo-PIV setup used to obtain flowfield images on the rotor in forward flight. For a given radial station, two high-speed cameras (Phantom v641, 4 Mpx, 1450 frames/sec at max resolution) were positioned in a stereoscopic configuration outside the confines of the test section. Each camera was outfitted with a Nikon 200mm f/2 telephoto lens and Schiempflug adapter, and focused on a field of view aligned with $\psi = 270°$. A double-pulsed, high-speed laser (Litron LDY304, 30 mJ/pulse, 10 kHz max) was installed beneath the test section floor and used to illuminate a planar region coincident with the cameras' field of view. Tracer particles were introduced into the flow by way of a theatre fog machine (PeaSoup Rocket, 180 m^3/min smoke output) and illuminated by the laser sheet near the blade. After completing the rotor's trim procedure, the cameras and laser were synchronized with the rotor's 60/rev encoder, and particle images were collected at an interval of $\Delta\psi = 6°$ as a rotor blade passed through our field of view.

The particle images were then processed using DaVis v8.4.0 by LaVision Inc. A multi-pass cross-correlation algorithm, with a 32 px × 32 px minimum window size and a 75% overlap, produced a grid of three-component vector fields for each image pair. As a final step, the resulting time-resolved flowfields were phase-averaged over 35 successive revolutions of the rotor. The ultimate product of this data acquisition procedure was a sequence of phase-averaged flowfields that show a single rotor blade as it passes through our field of view at a certain radial station and advance ratio. Each individual flowfield extends roughly two chords horizontally and one chord

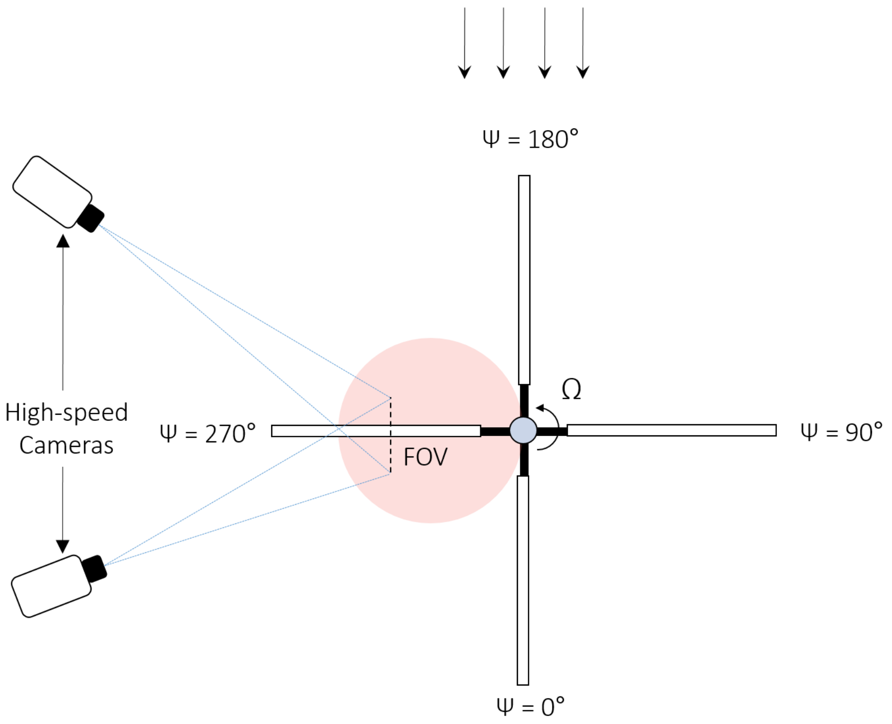

(a) Top-down view.

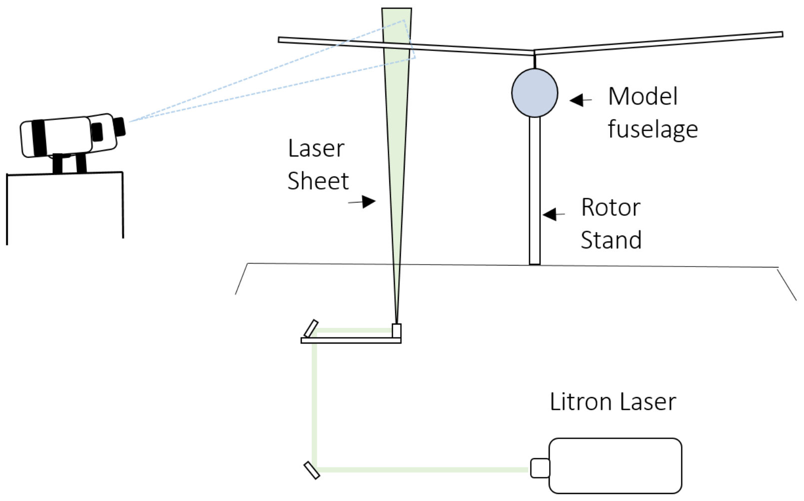

(b) Side view.

Figure 2.2: Illustration of the stereo-PIV setup used to obtain three-component flowfield measurements for a given radial station and advance ratio.

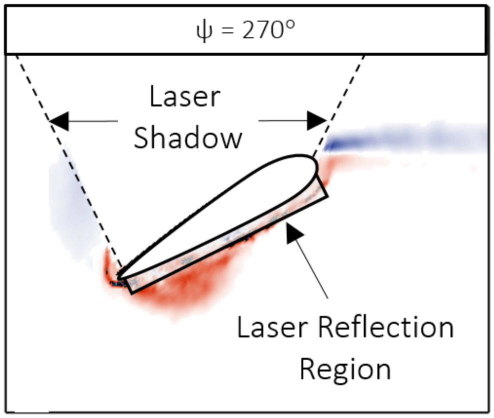

Figure 2.3: Sample phase-averaged vorticity field of the 45% blade element in reverse flow at $\mu = 0.80$.

vertically, and captures a single blade over the period $258° \leq \psi \leq 288°$.

Figure 2.3 shows a sample flowfield image to highlight the features and limitations of our data-collection procedure. This image was taken from an example flight condition of the rotor ($\mu = 0.80$, $\theta_0 = 10°$) and shows contours of vorticity for the 45% radial station midway through reverse flow ($\psi = 270°$). From this single image, one can clearly see a vortex rolling up about the sharp-edge of the rotor blade element, demonstrating the ability of our PIV setup to identify coherent flow structures in a complex rotor environment. However, one can also see a few important regions of the vorticity field that cannot be resolved by the current setup. The region very close to the lower surface of the blade, which nominally includes the boundary layer and feeding shear layer, is obscured by a large laser reflection at the blade surface, and contains only erroneous vectors. Likewise, the upper surface of the blade, and a large spatial region above it, are blocked by a substantial laser shadow. Both of these regions, and their erroneous vectors, will be manually masked in each flowfield image presented in the following sections.

We must also acknowledge that our planar PIV measurements, although very useful in identifying coherent flow structures on the rotor, are ultimately limited in terms of what they can reveal about the flow in three dimensions. Because our spanwise resolution is quite coarse (a consequence of time constraints on the tests), only a single component of the vorticity field (ω_z) can be accurately resolved at each radial station; 3-D vortex tilting and stretching, both characteristic of separated flows on revolving wings, cannot be directly quantified from our experimental measurements alone. Likewise, our field of view, which is fixed in space for a given radial station, is only nominally aligned with the blade chord at $\psi = 270°$, so even our measure of ω_z will inevitably be skewed at other azimuths. With these limitations in mind, the use of our experimental flowfields measurements is limited to a qualitative understanding of vortical structures in the following sections. The measurements can, however, also be used to validate a numerical simulation of the same flow, giving us an alternate avenue to investigate 3-D effects and gradients.

2.2 Simulation of a Rotor in Forward Flight

The previous section outlined an experimental methodology for obtaining flowfields in the reverse flow region of a rotor at high advance ratio. Although these measurements give an important sense for how the reverse flow region actually evolves on a rotor, the amount of information they provide is limited. If our goal is to model reverse flow using only the dominant physics of the region, we need to be able to quantify and understand how 3-D features of the flowfield, such as vortex tilting, spanwise convection, and Coriolis effects, impact the behavior of vortical structures in reverse flow, a task that cannot be accomplished with the resolution of our experimental measurements. Thus, we turn to a numerical simulation, with much higher spatial and temporal fidelity, to more rigorously investigate the reverse flow region at high advance ratio.

This section details a set of numerical CFD simulations undertaken to further interrogate the physics of reverse flow in more detail. The simulations were performed using an in-house finite volume solver (HAMSTR) on a model rotor with the same properties as the one used in our experimental measurements (see table 2.1 for specifics). Many of the details regarding our mesh generation and flow solver have been published in previous works, so only the main features of our simulation will be summarized here. A complete, thorough description of the mesh generation and finite volume components of HAMSTR, including how the algorithm was employed to solve for the flow over our rotor system, can be found in the works of Jung and Baeder [91, 92, 93], to whom the author is very much in debt for their guidance during the numerical stage of this research. The mesh generation and flow solver were developed entirely by Jung and Baeder, and were simply adapted to the geometry of our rotor system. Keep in mind, however, that the novel way in which the numerical flowfields were analyzed is a unique contribution of the current work.

Table 2.3: Primary and secondary flight conditions used in our CFD simulations.

	μ	θ_0	θ_{1s}	θ_{1c}	RPM
Primary	0.60	10°	-10.64°	2.80°	900
Secondary	0.80	11°	-12.69°	2.09°	700

2.2.1 Flight Conditions

The first step of our numerical methodology was to choose a forward flight condition of the rotor. Table 2.3 describes two forward flight conditions, one primary and one secondary, that served as baseline cases for the CFD simulations. The primary flight condition ($\mu = 0.60$, $\theta_0 = 10°$) was chosen to explicitly match the values of one of our experimental cases; it will be used primarily to validate the CFD simulation against experiment. The secondary flight condition ($\mu = 0.80$, $\theta_0 = 11°$) was chosen to slightly exaggerate the main features of reverse flow, and will be used to rigorously analyze the reverse flow region in a vorticity transport analysis. Our simulation procedure was identical in both the primary and secondary forward flight conditions.

After choosing a flight condition, our next step was to recreate the motion of the rotor blades in forward flight. The current numerical simulations make use of a CFD-CSD coupling procedure as a way of recreating the conditions of our experimental measurements as closely as possible. This methodology has the advantage of capturing the finer aspects of the blade motions, including their flap, lag, and torsion response, that were not measured in the experimental phase.

The CFD-CSD coupling procedure consisted of the following steps: first, an in-house flight dynamics solver [94] estimated the cyclic pitch inputs (θ_{1s}, θ_{1c}) and blade flap/lag response needed to achieve zero net moments about the hub. Next, a CFD simulation was completed using the results of the structural dynamics solver to prescribe the motion of the rotor blades. A table of aerodynamic lift, drag, and pitching moment was then extracted from the CFD simulation, and fed back into the next iteration of the structural dynamics solver. This coupling procedure, wherein blade motions were computed by the structural dynamics solver and aerodynamic forces were provided by the CFD, was repeated until the flowfield solution reached convergence. In this work, convergence is defined based on the lift coefficient generated at $r/R = 0.30$ for a given flight condition. An example of the iteration procedure, including a sample of a converged solution, is detailed in reference [95].

2.2.2 Mesh Generation

In the CFD step of our simulations, a volumetric mesh was generated about the rotor using HAMSTR, an in-house framework for mesh generation and flow computation. HAMSTR is a novel algorithm that uses Hamiltonian paths to identify the “hidden” line structure in an unstructured grid, and is especially useful in rotorcraft applications, where structured and unstructured grids are often combined to discretize complex blade and fuselage geometries. The mesh used for the current work was generated by Jung [93] using the blade geometry of our rotor system and

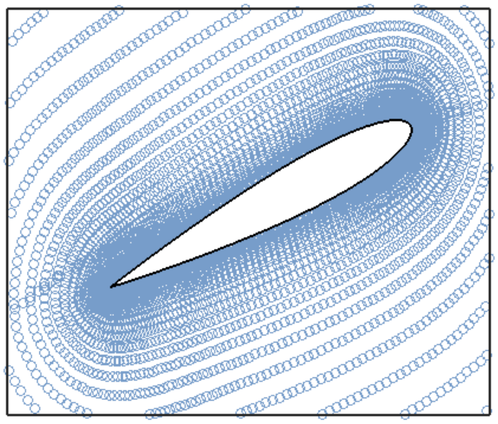

Figure 2.4: Example of the mesh generated by HAMSTR (with cell centers plotted represented by circles) at the 45% radial station of our rotor system.

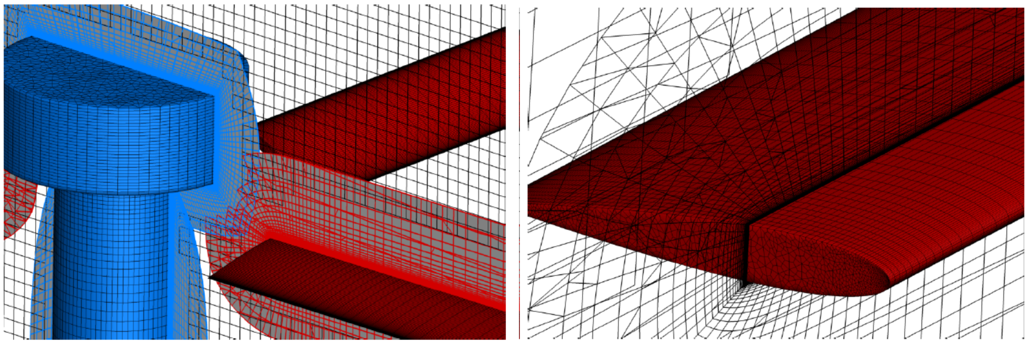

(a) Representative hub.

(b) Blade and blade tip.

Figure 2.5: Illustration of structured and unstructured portions of our mesh in three dimensions.

a simplified version of the hub.

Figure 2.4 shows a sample mesh for the $r/R = 0.45$ blade element as generated using HAMSTR. To create this mesh, the rotor blade was discretized into 200 points in the blade-wrap direction, and 100 points in the spanwise direction. Each cell along the surface of the blade was extruded outward, normal to the blade surface, to generate a volumetric mesh surrounding the rotor blade. The extrusion used an initial wall-normal spacing of 5×10^{-5} chord lengths, and consisted of 47 strand layers oriented away from the surface of the blade. The blade-tip region, which is not covered by the structured mesh extruded from the blade, was separately discretized into a series of unstructured hexagonal cells. An “off-body” cartesian mesh (uniform spacing of 0.10 chords) was also combined with the near-body cells using an overset technique.

A more three-dimensional view of the final mesh can be found in figure 2.5. From this figure, one can see, for a single rotor blade, the structured mesh extruded along the blade span, the unstructured mesh that makes up the blade tip, and an additional unstructured mesh surrounding a representative fuselage structure. At each time-step of the rotor’s revolution, the mesh shown in figure 2.5 was deformed according to the unsteady motions of each individual rotor blade, such that the blade boundary condition could be enforced at the same points in the mesh.

2.2.3 Flow Solver

An in-house finite volume solver was used to solve the unsteady Reynolds-averaged Navier Stokes equations (URANS) on the volumetric mesh described in the previous section. The mixture of grid types seen in figure 2.5 would typically require a series of different line reconstruction techniques to solve the governing equations, but the novelty of HAMSTR is that the algorithm is able to identify a line structure in both the structured and unstructured portions of the mesh. The flow solver can thus use the more accurate stencil-based reconstruction techniques throughout the entire flow domain, improving both the speed and accuracy of the ultimate solution.

In solving for the flow over our rotor system, the HAMSTR algorithm assumed compressible, viscous, and fully turbulent flow. Closure of the URANS equations was achieved using the Spalart-Allmaras turbulence model. The flow field was computed every one degree of rotor revolution, and a second-order backward time-stepping procedure was used to advance the solution. A fifth-order weighted essentially non-oscillatory (WENO) scheme was used for spatial reconstruction, while Roe's approximate Riemann solver was used to compute the inviscid fluxes. Viscous fluxes were handled with second-order central differencing.

Together with the experimental measurements, the flowfields that result from the above simulation procedure represent the primary tools for investigating the physics of the reverse flow region in the current work. The experimental measurements are used to identify coherent structures in reverse flow (and to validate the numerical simulation), while the CFD flowfields are employed in a detailed analysis of 2-D and 3-D vorticity transport. Although these two experiments extensively cover the reverse flow region, or the most significant source of flow separation on a rotor at high advance ratio, we must keep in mind that separation is possible at other locations on the rotor disk as well. The next section will describe an additional experimental campaign, performed in a water-filled tow tank facility, intended to address the possibility of flow separation outside the confines of the reverse flow on a high advance ratio rotor.

2.3 Measurements on a Surging and Pitching Wing

Thus far, the previous sections have outlined an experimental and numerical methodology for investigating the vortical structures that form in the reverse flow region of a spinning rotor. The reverse flow region, however, is not the only source of separated flow on an articulated rotor operating at high advance ratio. Dynamic stall, or the formation of a vortex about the *blunt* edge of the rotor blade, may also occur before the blade element transitions into the reverse flow region. Such an event can have a dramatic impact on the forces generated on the retreating side of the rotor, and is thus a fundamental part of understanding flow separation on a rotor at high advance ratio.

This section will describe a simple 2-D experimental campaign undertaken to investigate separation about the rounded edge of a rotor blade element. Unlike the sharp-edge flow separation expected to occur in the reverse flow region, separation about a blunt edge is a much more difficult process to understand and predict. The 2-D nature of these experiments was thus chosen to remove the rotational aspects of the flowfield and to focus only on the effects of an unsteady freestream and pitching variation. These experiments thus similar to the conventional dynamic stall experiments found in the literature, albeit with the inclusion of a large-amplitude freestream oscillation. The following sections will describe the test articles, facility, and optical measurement techniques used in conducting the 2-D surging and pitching wing experiments.

2.3.1 Test Articles, Facility, and Kinematics

The surging/pitching wing experiments were performed with a simple NACA 0012 wing. The wing was fabricated using Objet30 3-D printer and featured a chord of $c = 0.115$ m, a span of $b = 0.460$ m, and an aspect ratio of $AR = 4$. To conduct the experiments, the wing was submerged in a 7 x 1.5 x 1 m free-surface water-filled tow tank located at the University of Maryland. The tow tank is equipped with a magnetic track and gantry designed to execute surging wing maneuvers over its longitudinal dimension. The gantry houses three brushless linear motors and two control rods for mounting and pitching of the test article. Figure 2.6(a) shows a photograph of the test facility, highlighting the tow track, motors, and wing mounting apparatus, while figure 2.6(b) features a simple sketch of how the wing was positioned beneath the free surface of the tank.

The kinematics of these experiments were chosen to approximate the rotary motion of a rotor blade element with an equivalent rectilinear surge. Specific details regarding the parameter space of these experiments, including how they relate to the flight conditions of our rotor system, can be found in chapter 6, so only the basic form of the wing kinematics will be outlined here. In each run of the experiment, the wing was subject to a simultaneous surging and pitching oscillation, both of which are intended to mirror the local freestream and pitching variation experienced by a rotor blade element at high advance ratio. The wing surge velocity $(U(t))$ can be represented as follows:

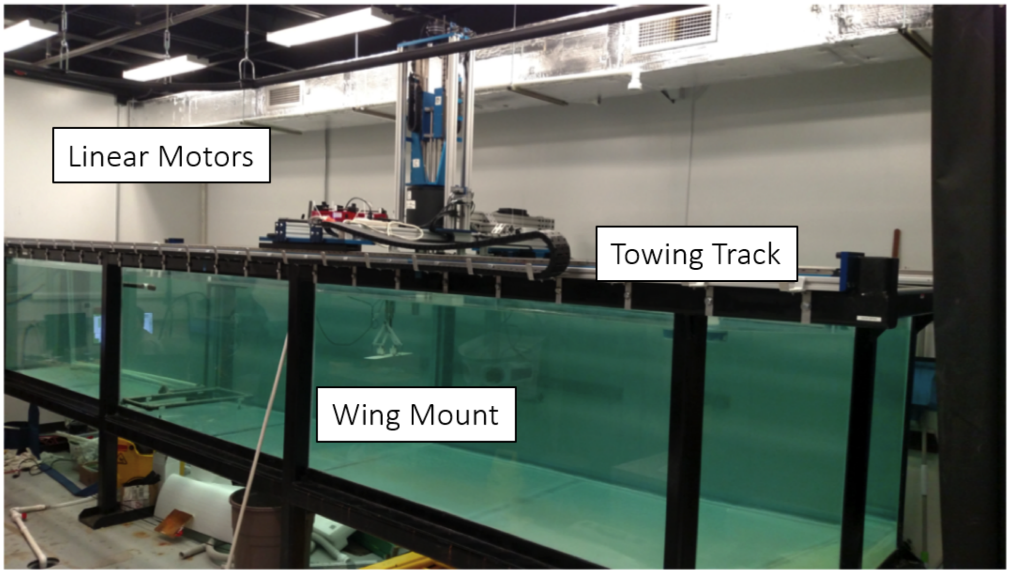

(a) The tow tank facility.

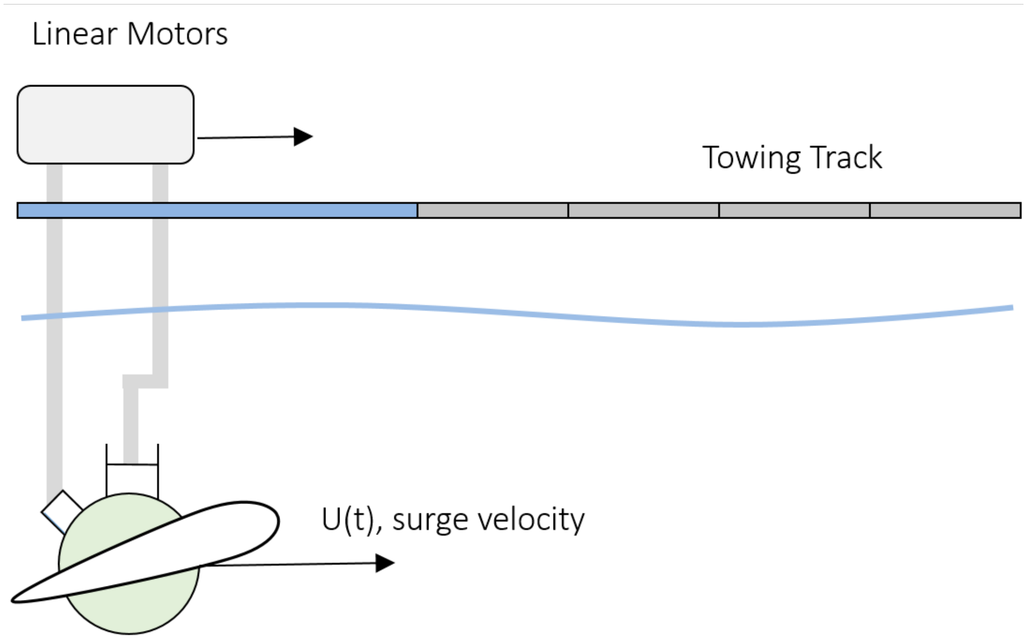

(b) Illustration of the wing mount.

Figure 2.6: Photograph and sketch of the 7 x 1.5 x 1 m water-filled tow tank facility.

$$U(t) = U_0\Big(1 + \lambda \sin\psi\Big), \tag{2.2}$$

where U_0 is a mean surge velocity, and λ is a non-dimensional surge amplitude. The variable ψ is a non-dimensional "cycle" time used in the following sections to denote specific points in the oscillation. This parameter is formally defined as $\psi = \Omega t$, where t is the time from the start of the oscillation, and varies from $\psi = 0°$ to $\psi = 360°$ over the course of a single oscillation. The deceleration portion of the oscillation, then, is denoted by the region $180° \leq \psi \leq 270°$, just as it would be for a rotor blade element in forward flight.

The wing pitching kinematics, completed concurrently with the surge oscillation, take a very similar form to what was described in equation 2.2. The geometric incidence of the wing ($\theta(t)$) can be described according to the following simple oscillation:

$$\theta(t) = \theta_0 + \theta_1 \sin\psi + \phi, \tag{2.3}$$

where again, θ_0 is a mean pitch angle, θ_1 is a pitch amplitude, and ψ is a non-dimensional cycle time. The final parameter, ϕ, represents a phase shift between the surging and pitching kinematics. This phase shift will be set to $\phi = \pi$ for all 2-D experiments presented in this work, such that the pitch-up portion of the wing kinematics occurs at the same time as the wing deceleration, similar to what occurs on the retreating side of a rotor in forward flight. Note that all wing pitching motions were performed using the wing's quarter chord (measured relative to the blunt leading edge of the wing) as the axis of rotation.

Figure 2.7 provides a sample surge and pitch oscillation to illustrate the basic kinematics of our 2-D tow tank experiments. In each run of the experimental setup, the wing undergoes a complete surge and pitch oscillation to remove any initial "start-up" transients present in the flow ($-360^\circ \leq \psi < 0^\circ$) before beginning the primary oscillation of interest ($0^\circ \leq \psi \leq 360^\circ$). Flowfield measurements are collected in the region $160^\circ < \psi < 260^\circ$, or during the pitch-up portion of the wing's kinematics, in hopes of capturing any flow separation that occurs in the forward flow (i.e., blunt-edge to sharp-edge) period of the oscillation. Analysis of these experiments will focus on these periods of blunt-edge flow separation, and specifically on how the very large unsteady freestream oscillation impacts the onset and behavior of any resulting vortical structures.

2.3.2 Flowfield Measurements

Flowfield measurements were collected using a standard two-component setup, and captured the flow over the wing in a Lagrangian, moving frame of reference. A single high-speed camera (Phantom v641, 4 Mpx, 1450 frames/sec max) was positioned outside the tow tank and physically fixed to the tow track via an aluminum arm that extended from the gantry. The camera was then towed along with the wing throughout its surge oscillation such that the position of the wing pitch axis remained reasonably constant within the field of view. A double-pulsed laser (Litron LDY304, 30 mJ/pulse, 10 kHz max) was synchronized with the camera and used to create

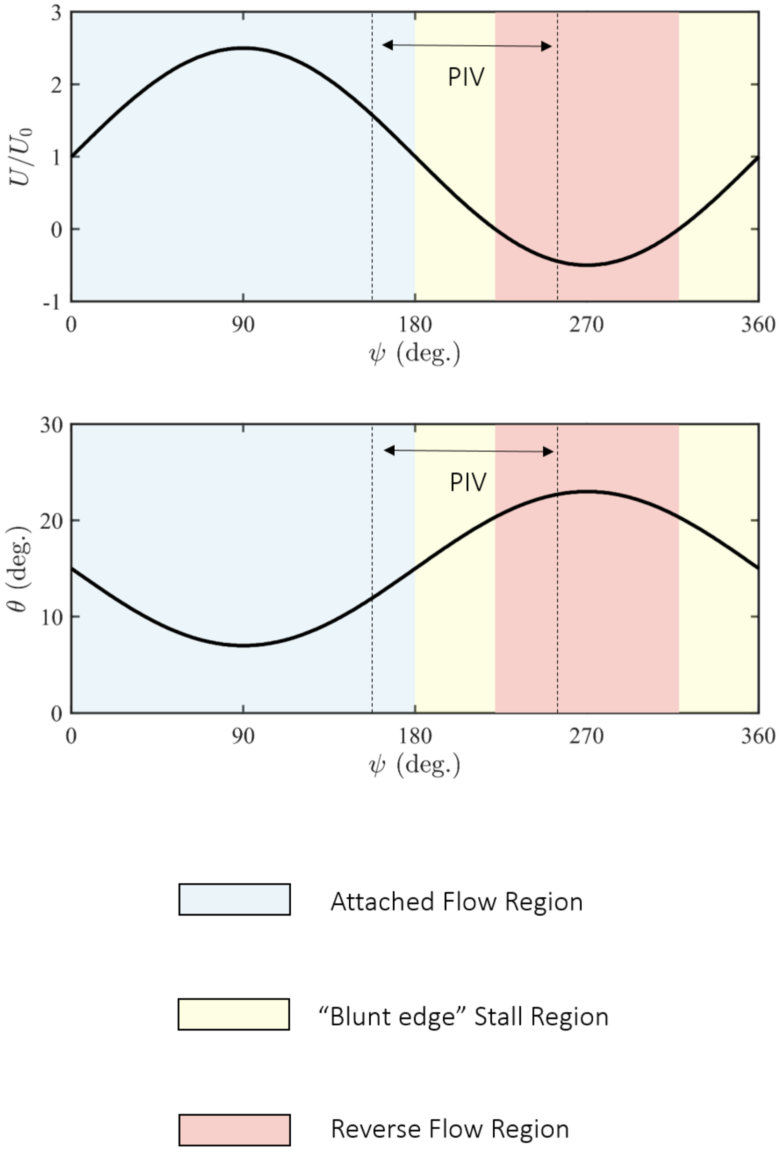

Figure 2.7: Sample surging and pitching kinematics for the NACA 0012 wing in the tow tank experiments.

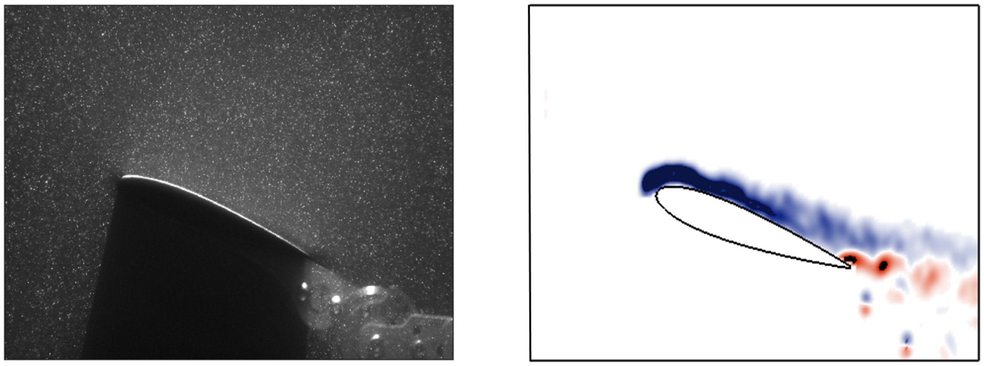

Figure 2.8: Example particle image (left) and the resulting phase-averaged vorticity field (right).

a light sheet, located 1 chord from the wing centerline, using a series of reflective mirrors. When the wing reached $\psi \approx 160^\circ$ for a given set of kinematics, both the laser and camera were triggered, and particle images were collected at a frequency of 250-500 Hz, depending on the exact frequency of the surge/pitch oscillation. All 2-D flowfield measurements were phase-averaged over six total runs of the experiment.

Figure 2.8 shows a sample particle image (left) and vorticity field (right) computed for a baseline set of surging and pitching kinematics of the wing. The snapshots in figure 2.8 demonstrate one of the main advantages of this data set compared to the rotor experiments. That is, our 2-D PIV setup is able to resolve regions very close to the surface of the wing, capturing the flow within the boundary layer. Such resolution, and the associated boundary layer statistics it allows us to calculate, will prove to be quite valuable to the analysis of blunt-edge flow separation found in chapter 6.

2.4 Chapter Summary

This chapter detailed three data-acquisition campaigns undertaken to investigate flow separation on a rotor operating at high advance ratio. The first campaign specifically targeted the reverse flow region, believed to be the primary source of flow separation on a high advance ratio rotor, and involved the collection of flowfield measurements on a Mach-scale rotor operating in forward flight. The resulting flowfield measurements are intended to qualitatively identify the coherent flow structures of the reverse flow region. The second campaign involved numerically simulating the flow over the same rotor system at a subset of forward flight conditions. This numerical data set is intended to reveal the more complex 3-D vortex dynamics of reverse flow that could not be captured by the coarse spanwise resolution of our experimental measurements.

The final campaign sought to extend our analysis to flow separation that occurs outside of reverse flow on a high advance ratio rotor. Here, the complex rotor flowfield was simplified to a simple surging and pitching wing, and experimental flowfield measurements were collected during the pitch-up/deceleration portion of the wing's motion. Together, these three campaigns represent a comprehensive investigation of the flow physics governing separation on a high advance ratio rotor, both during and prior to the onset of reverse flow on the rotor's retreating side, and will be used in the following section to understand and develop a modeling framework for the separated flow in high advance ratio forward flight.

Chapter 3: Vortex Structures in the Reverse Flow Region

Before we can develop a model of the separated flow on a high advance ratio rotor, we must first obtain a general idea of how this flow evolves over time. The purpose of this chapter is to identify the dominant flow structures present on a rotor at high advance ratio, and qualitatively observe how those flow structures evolve both spatially and temporally. This task is accomplished through a series of flowfield measurements intended to showcase the fundamental morphology of the reverse flow region. In addition to providing a basic picture of reverse flow in three dimensions, these experimental measurements serve as a benchmark for a high-fidelity numerical simulation of a rotor at high advance ratio, the results of which will serve as the basis for a more rigorous flowfield analysis in later chapters.

3.1 Kinematics

The current chapter seeks to introduce the fundamental features of the reverse flow region by considering our rotor system at a "primary" set of blade kinematics. These blade kinematics are intended to highlight the main flow structures of the reverse flow region at high advance ratio, while also remaining representative of the operating conditions of a "slowed" (or high-speed) rotor system. Table 3.1 defines

Table 3.1: Properties of the primary forward flight condition of the rotor.

Ω	μ	θ_0	θ_{1s}	θ_{1c}	R	c
900 RPM	0.60	10°	−8.9°	4.6°	0.85 m	0.08 m

the primary condition of the rotor system according to three properties of its flight condition: the angular velocity of the rotor ($\Omega = 900 RPM$), the advance ratio of the rotor ($\mu = 0.80$), and the collective pitch input of the rotor ($\theta_0 = 10°$). The longitudinal (θ_{1s}) and lateral (θ_{1c}) cyclic pitch inputs, which are necessary to achieved a "trimmed" state for a given advance ratio and collective, are also included in table 3.1 to fully describe blades' pitching kinematics. The following sections will use flowfield measurements to visualize the flow structures and gradients present on our rotor system at the primary forward flight condition described in table 3.1. The flowfields are collected at three radial stations ($0.30 \leq r/R \leq 0.60$), which span the majority of the reverse flow region at $\mu = 0.60$, as a way of capturing these flow structures in three dimensions.

3.2 Flow Morphology

The complete, three-dimensional flowfield of a spinning rotor in forward flight can be a rather overwhelming flow environment to visualize. In addition to a time-varying local freestream and pitch condition, rotor blades in forward flight are subject to a variety of spanwise gradients in their flow properties that can significantly impact how the various flow structures evolve in space and time. In the interest of simplicity, this section takes a "blade-element" approach to understanding the evolution of the reverse flow region, first showing the dominant flow structures at a single radial location before considering these same flow structures at other positions along the blade span. The dominant flow structures will be identified based on (1) their vorticity and (2) their effect on the flow along the blade span.

3.2.1 Vorticity Field

Figure 3.1 presents a series of phase-averaged flowfield snapshots that capture the 45% radial station as it passes through a portion of the reverse flow region ($258° \leq \psi \leq 288°$) at the primary forward flight condition ($\mu = 0.60$, $\theta_0 = 10°$). In each snapshot, the local freestream velocity is traveling from left to right, and the blade section is overlain with contours of non-dimensional spanwise vorticity ($\omega_z c/U_\infty$). A value for the convective time (s) is included in each snapshot as a way of denoting how far the blade section has traveled in reverse flow by the time it appears in our field of view. Convective time, which denotes the number of semi-chords traveled by a rotor blade element in the reverse flow, can be defined according to equation 3.1:

$$s = \frac{2}{\Omega c} \int_{\psi_i}^{\psi_f} U_T(\psi) \mathrm{d}\psi, \tag{3.1}$$

where U_T is the blade-normal velocity, ψ_i is the time at which the blade enters reverse flow, and ψ_f is the time at which it exits. The first snapshot of figure 3.1 captures the blade element a short time after it enters the reverse flow region ($s = 0$, $\psi_i = 229°$), and the final snapshot captures the blade element shortly before it begins

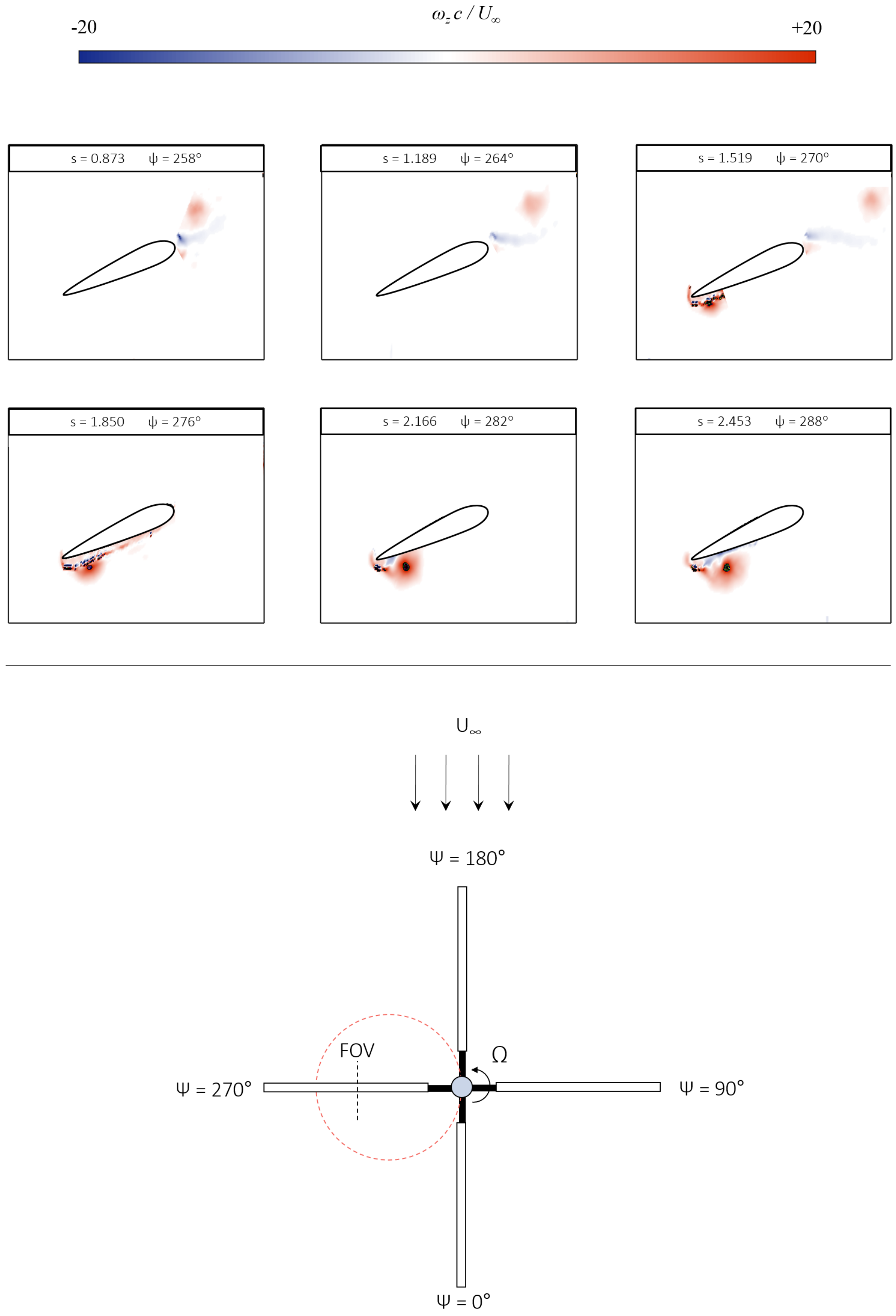

Figure 3.1: The phase-averaged vorticity field of the 45% radial station as it passes through reverse flow at the primary forward flight condition ($\mu = 0.60$, $\theta_0 = 10°$).

to transition back to forward flow ($s = 3.04$, $\psi_f = 311$).

Just from these few phase-averaged snapshots, figure 3.1 highlights the presence of two large-scale, coherent vortex structures in the reverse flow region of a rotor at high advance ratio. The first, and perhaps most unexpected, of these flow structures is the bundle of positive (red, counter-clockwise) vorticity that emanates from the blunt edge of the rotor blade over the period $258° \leq \psi \leq 270°$. This vortex, referred to as the "blunt-edge" vortex in the remainder of this thesis, appears to "lead" the $r/R = 0.45$ blade element as it passes through the reverse flow region, convecting beyond the blunt edge of the blade. The size of the blunt-edge vortex also appears relatively unchanged over the period $258° \leq \psi \leq 270°$; in fact, its size and strength are rather substantial even at very early times in reverse flow. All of this is to suggest that the vortex rolls up about the blunt-edge of the blade in forward flow, prior to the reversal of the local freestream, and the reverse flow region simply governs its convection behavior.

The second vortex structure visible in figure 3.1 is a bundle of positive vorticity located near the lower surface of the blade element over the period $270° \leq \psi \leq 288°$. This vortex, known as the "sharp-edge" vortex in the remainder of this work, is more familiar, and appears to result from flow separation about the sharp edge of the blade following the onset of freestream reversal. Although slightly obscured by the laser reflection, a shear layer can be observed at the sharp edge of the wing beginning at $\psi = 270°$, and the vorticity generated at this sharp edge is seen to feed the vortex throughout the remainder of the blade's passage. By $\psi = 288°$, the size of this sharp-edge vortex appears to be quite substantial, and a region of opposite-signed vorticity (blue, clockwise) appears between the sharp-edge vortex and the lower surface of the wing.

The two vortex structures highlighted in figure 3.1, one originating from the blunt edge of the blade and one originating at the sharp-edge, form the basis of the analysis presented in this thesis. Due to their proximity to the surface of the blade, each flow structure is expected to have significant impact on the blade loads at high advance ratio, but because of the nature of a separated flow, neither is able to be accurately modeled using conventional aerodynamic tools. The remainder of this chapter is aimed at giving the reader a basic idea of how these two flow structures behave in three dimensions, while later chapters will address the physics of each flow structure in more extensive detail.

3.2.2 3-D Flow Features

In the previous section, two large-scale vortical structures were identified in reverse flow, an important step in understanding how the flow in this region evolves. We must keep in mind, however, that this identification was limited to a single component of the vorticity field at a single radial station of the rotor. The three-dimensional aspects of the flowfield, including gradients and flow along the blade span, may also play an important role in how our flow structures evolve over time. This section will introduce and familiarize the reader with the spanwise gradients and spanwise flow present in the reverse flow region, two crucial components of the flowfield that will become a major part of our analysis in chapter 5 .

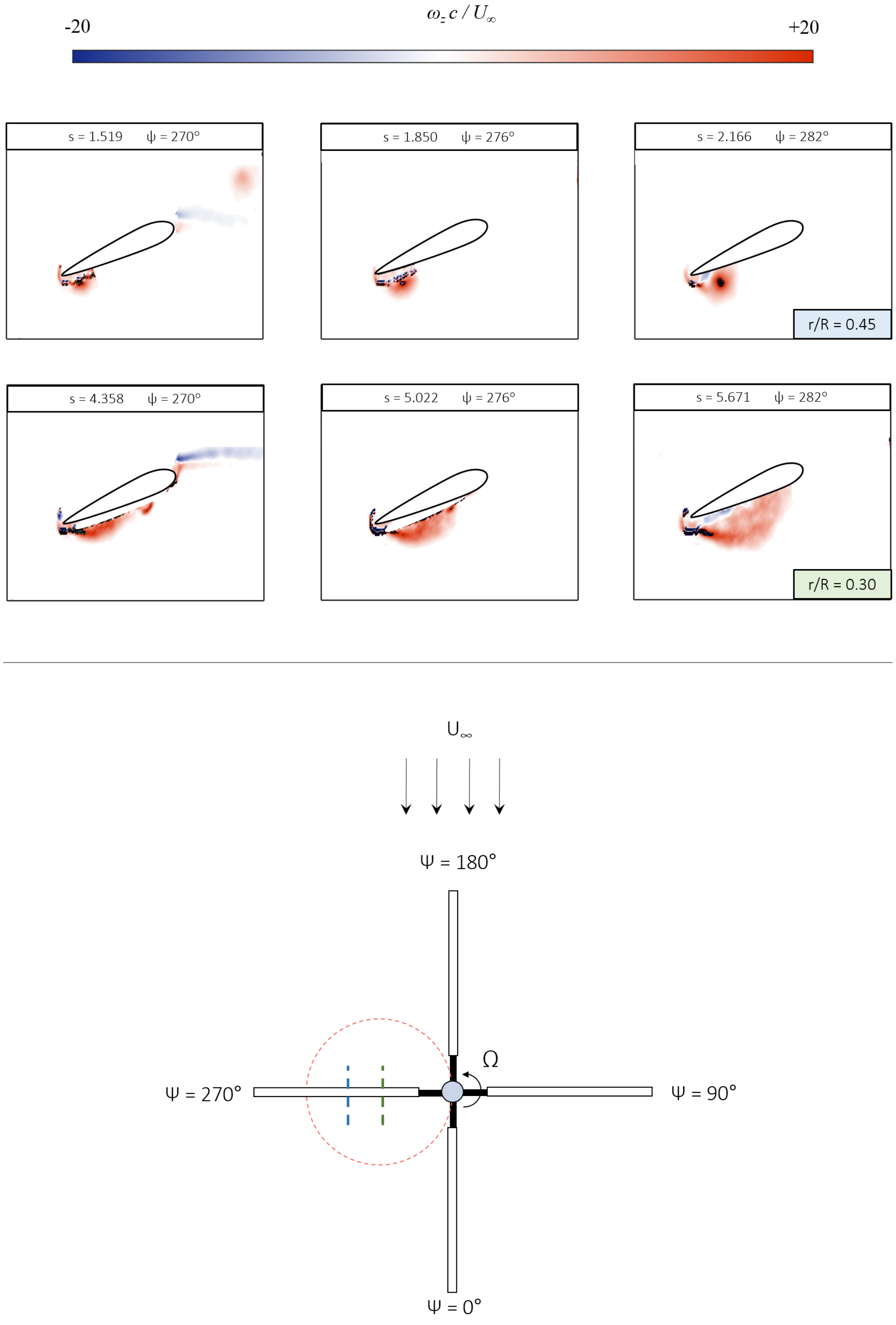

Figure 3.2: Phase averaged vorticity fields for $r/R = 0.45$ (top row) and $r/R = 0.30$ (bottom row) in the reverse flow region at the primary forward flight condition ($\mu = 0.60$, $\theta_0 = 10°$).

First, we will consider how a simple change in radial station impacts the basic flow features described in the previous section. Figure 3.2 shows the vorticity field for two radial stations, one corresponding to $r/R = 0.45$ (top row) and a second corresponding to $r/R = 0.30$ (bottom row), at the rotor's primary forward flight condition ($\mu = 0.60$, $\theta_0 = 10°$). The local freestream is again traveling from left to right in each subfigure, and the position of each radial station relative to the bounds of the reverse flow region is included in the sketch below. Figure 3.2 clearly indicates that the sharp-edge vortex is substantially larger at the inboard radial station ($r/R = 0.30$) compared to the vortex at the outboard station ($r/R = 0.45$). Likewise, the blunt-edge vortex, which was located quite close to the blade at $r/R = 0.45$, is not visible in any of the flowfield snapshots at $r/R = 0.30$, implying that this flow structure has convected out of our field of view. The reverse flow region in general appears more developed at the inboard radial station, a rather unique result compared to what occurs in the case of forward flow or hover [96], where the magnitude of the blade-tangent velocity increases at outboard stations.

The effect of changing radial station can be very easily related to the blade-tangent velocities experienced by each rotor blade element. In reverse flow, the magnitude of the local freestream velocity actually increases as one moves inboard, since the inboard regions have a lower rotational velocity component. The $r/R = 0.30$ blade element has thus traveled a larger number of chords in reverse flow by the time it reaches our field of view compared to the $r/R = 0.45$ blade element, leading to the more developed nature of the flow at the inboard station. The resulting spanwise gradients, wherein the magnitude of vorticity increases as one moves inboard, is unique to the reverse flow region, and will become a very important observation in later sections.

It is also important to recognize that a spanwise gradient in vorticity, and the spanwise pressure gradient that this creates, will inevitably lead to the presence of flow along the blade span. Figure 3.3 plots contours of this spanwise flow for the 45% radial station at the primary forward flight condition. The contours are defined such that a root-to-tip flow is positive (and plotted in orange) while a tip-to-root flow is negative (and plotted in purple). Figure 3.3 illustrates that the center, or "core," of the sharp-edge vortex is associated with a strong tip-to-root (purple) spanwise flow throughout the blade's passage through our field of view. The direction of this spanwise flow (tip-to-root) is consistent with the gradients in vorticity described above, as the inboard regions of the rotor are subject to a larger blade-tangent velocity, and in turn a lower static pressure, compared to outboard stations. The sharp-edge vortex is seen to exacerbate the magnitude of the tip-to-root flow in figure 3.3, likely due to the additional pressure deficit it creates at inboard locations [46].

At this point, let us briefly recap the essential 2-D and 3-D features of the reverse flow region covered in the last two sections. First, planar flowfield measurements were able to reveal the presence of two coherent vortical structures, a blunt-edge vortex and a sharp-edge vortex, at the primary condition of our rotor. Next, these flow structures were seen to be more developed at inboard stations of the rotor in reverse flow compared to outboard stations. The resulting spanwise gradient in vorticity lead to a strong spanwise flow that traveled from the blade

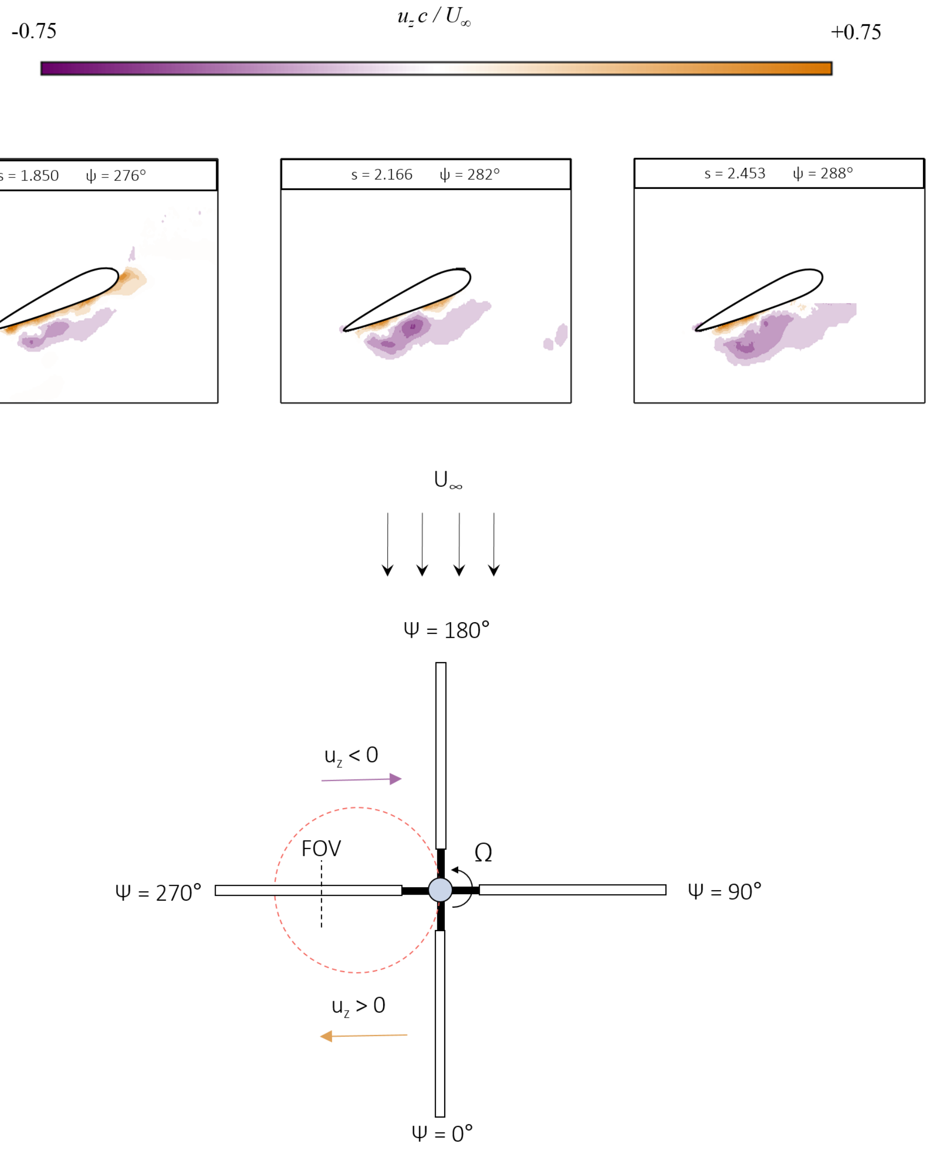

Figure 3.3: Phase-averaged contours of spanwise flow in the reverse flow region at the primary forward flight condition ($\mu = 0.60$, $\theta_0 = 10°$, $r/R = 0.45$).

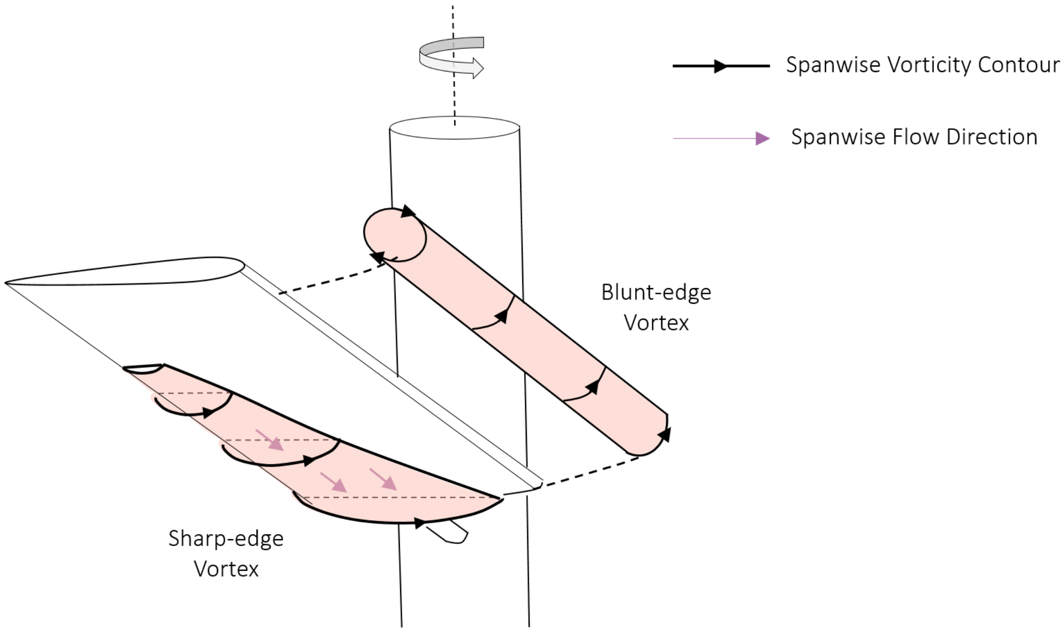

Figure 3.4: Qualitative illustration of the fundamental vortical structures, gradients, and spanwise flow in the reverse flow region of a rotor at high advance ratio.

tip toward the blade root, or in the opposite direction compared to what is seen in hover. These basic observations represent the fundamental morphology of the reverse flow region in three dimensions. Figure 3.4 provides a concise illustration of the three-dimensional structure of the reverse flow region, and highlights the spatial gradients in vorticity and the direction of spanwise flow. It will be crucial to keep this picture of the flowfield in mind as we move into the more rigorous analysis of chapters 5 and 6.

3.2.3 Effect of Advance Ratio

The previous section detailed the fundamental structure of the reverse flow region in three dimensions, but it is important that we also consider how a change in the advance ratio affects the main features of this region. Such a consideration will ensure the reader that more aggressive flight conditions, used later in this thesis to investigate the evolution of the sharp-edge vortex, still stick to the basic flow morphology introduced above.

Figure 3.5 shows a sequence of vorticity fields for a number of advance ratios at the 45% radial station. The top row corresponds to an advance ratio of $\mu = 0.60$ (the primary forward flight condition); the middle row corresponds to an advance ratio of $\mu = 0.70$; and the bottom row corresponds to an advance ratio of $\mu = 0.80$. A simple sketch is again included at the bottom of figure 3.5 to denote the position of our field of view relative to the confines of reverse flow for each of the three advance ratios. An increase in advance ratio in figure 3.5 is seen to consistently result in a larger size of the sharp-edge vortex for a given azimuthal location. Likewise, an increase in advance ratio is also seen to convect the blunt-edge vortex further downstream for a given azimuth, as this flow structure is outside our field of view in both the $\mu = 0.70$ case and the $\mu = 0.80$. In this way, an increase in advance ratio is actually quite similar to a decrease in the radial station. Higher advance ratios correspond to higher local freestream velocities, and in turn the reverse flow region appears more developed by the time it reaches at higher values of μ.

Figure 3.5 clearly indicates that an increase in advance ratio leads to a larger sharp-edge vortex, but it must be noted that an exception would be instances where the vortex grows so large that it experiences “vortex burst.” The term “vortex burst” describes a state of the flow wherein the coherence of the vortex collapses and the flow becomes disorganized. The early stages of such an event are visible at

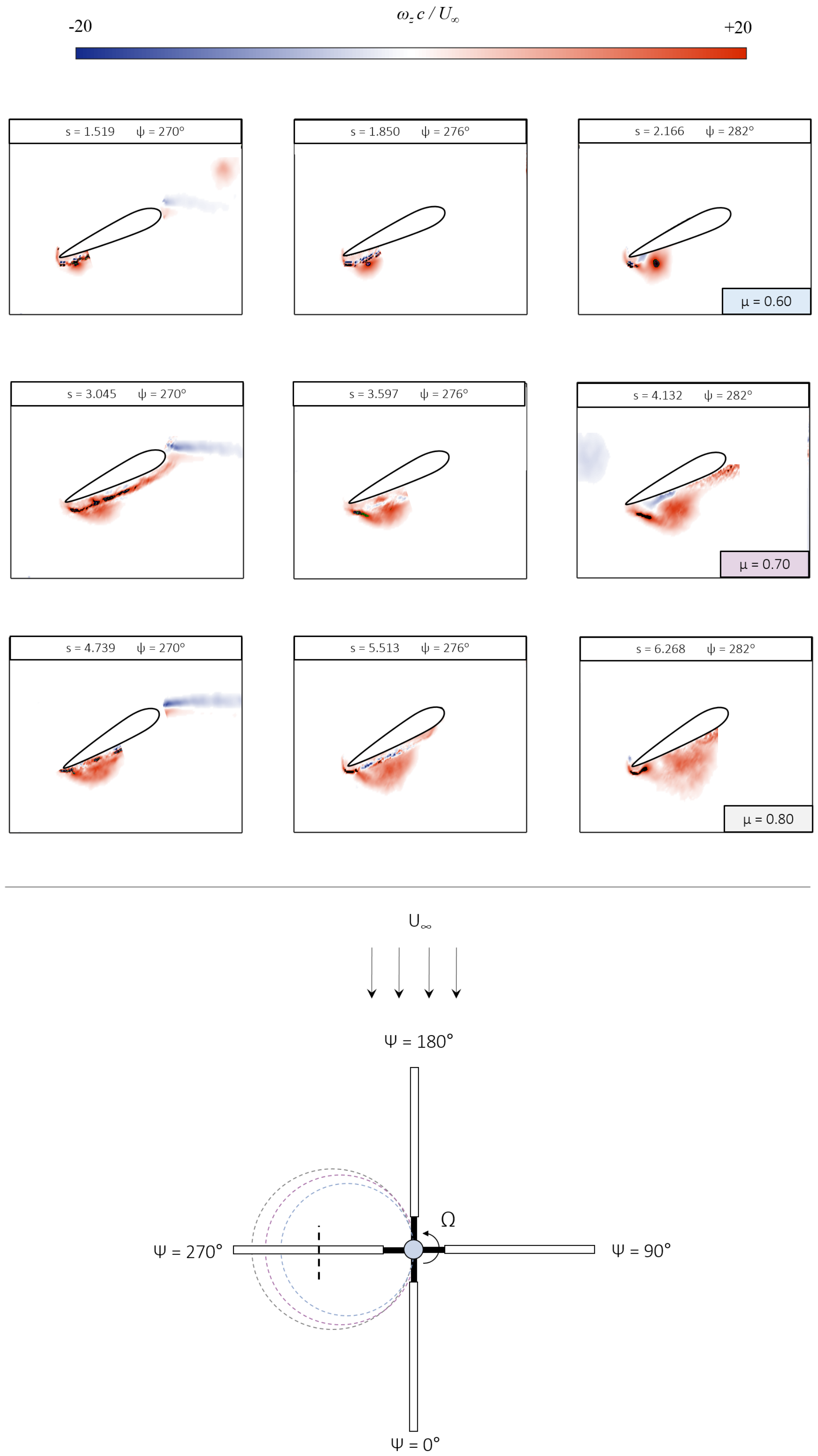

Figure 3.5: Phase averaged vorticity fields for $\mu = 0.60$ (top row), $\mu = 0.70$ (middle row), and $\mu = 0.80$ (bottom row) for $r/R = 0.45$ and $\theta_0 = 10°$.

$\psi = 282°$ for the $\mu = 0.80$ case, in which the vortex appears quite diffuse and less coherent (figure 3.5). The occurrence of vortex burst is expected to become a more significant issue as the advance ratio continues to increase beyond the values reported here. One could thus conclude that an increase in advance ratio does generally lead to an increase in the strength of the sharp-edge vortex, with the caveat that the onset of vortex burst will complicate (and possibly reverse) this trend. The notion of vortex burst will be visited at some length in chapter 5.

3.3 CFD Validation

At this stage, we have successfully identified the dominant vortical structures of a rotor at high advance ratio and have qualitatively observed how those structures change with the basic properties of the rotor's flight condition. We are still, however, quite far from our goal of being able to accurately re-create the reverse flow region with a low-order model. In order to accomplish this goal, we still need to fully understand how the various physical mechanisms at play on a rotor blade at high advance ratio, including the time-varying freestream, the pitch angle, and the 3-D effects outlined above, impact the evolution of our flow structures. Such an undertaking is quite difficult using our experimental measurement alone. Many of the 3-D effects on the rotor, in particular, are dependent on gradients along the blade span, which cannot be accurately captured from the coarse spanwise resolution achieved in our measurement campaign.

Our solution is to turn to a numerical simulation of the same rotor flowfield. A

CFD data set, computed using HAMSTR in our case (see chapter 3), has the distinct advantage of a very fine volumetric resolution, allowing for a quantification of 3-D gradients that would be impossible to ascertain from our experimental data. In this way, a high-fidelity numerical simulation is much better suited to investigating vortex behavior in a 3-D rotor environment. As usual with numerical simulations, however, the validity of the solution must be firmly established before any more detailed analysis can take place. This section will present a comparison of our experimental flowfield measurement and a CFD solution of the same flow, such that the high-fidelity numerical data can be used in later sections to rigorously investigate the formation of vortices in reverse flow.

3.3.1 Flowfield Comparison

A number of important observations regarding the veracity of these CFD simulations can be obtained from a simple qualitative comparison with experimental data. Figure 3.6 presents a side-by-side comparison of the experimental flowfields (top row) and the numerical flowfields (bottom row) for the primary forward flight condition of the rotor ($\mu = 0.60$, $\theta_0 = 10°$) over a portion of the reverse flow region. It is apparent from figure 3.6 that the numerical simulation does indeed capture the same primary flow structures observed in our experimental measurements. The blunt-edge vortex, for instance, can be seen emanating from the rounded edge of the rotor blade element at the $\psi = 270°$ snapshot from the CFD, and the sharp-edge vortex is situated at the lower surface of the blade throughout the entire sequence

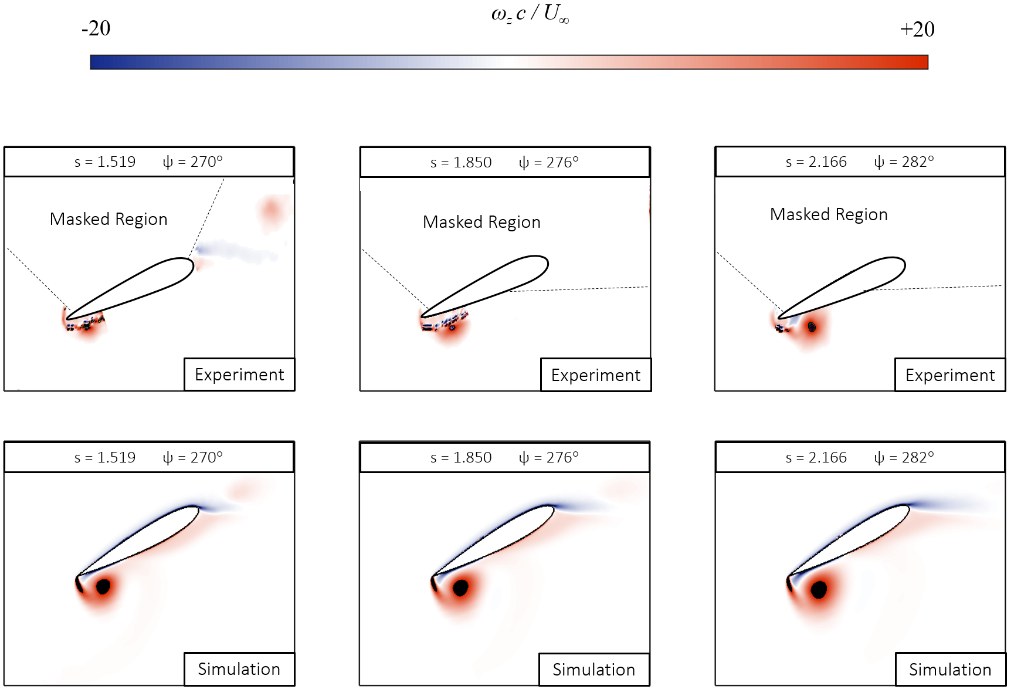

Figure 3.6: Vorticity fields from experimental measurements (top row) and CFD simulation (bottom row) for the primary forward flight condition of the rotor system ($\mu = 0.60$, $\theta_0 = 10°$).

of images. What is more, the CFD resolves many of the regions originally obscured by the blade in our experimental measurements, particularly the region close to the blade surface that includes the shear layer at the sharp edge.

The agreement in figure 3.6, however, is not perfect. For one, the blunt-edge vortex appears notably weaker in the CFD simulation, and is located much further upstream in the $\psi = 270^\circ$ snapshot. In addition, the sharp-edge vortex in the CFD, although its size is accurately predicted, appears to contain a slightly larger magnitude of vorticity in its core compared to experimental measurement. This latter point may be attributed to inaccuracies in the CFD-CSD coupling procedure; the simulation predicted a lower value of the lateral cyclic (θ_{1c}) than was observed in the experiment, meaning the blade was at a slightly higher incidence in reverse flow in the CFD. It is unclear from figure 3.6 whether the slight difference in vorticity magnitude can be considered a significant error, as a sizable portion of the sharp-edge vortex is obscured by the laser reflection in the experimental measurement. To answer this question, we must turn to a more quantitative metric of comparison between experiment and simulation.

3.3.2 Computing Vortex Strength

The error in our numerical simulation can be more accurately assessed by comparing a quantitative flowfield statistic between the experiment and CFD. For our purposes, we have chosen the strength, or circulation, of the sharp-edge vortex as the metric of comparison between the two data sets. The sharp-edge vortex is one of the two main vortical structures in reverse flow, and its strength over time is coupled to various features of the flowfield, including the interplay between 2-D and 3-D mechanisms of vorticity transport. A successful prediction of the sharp-edge vortex, then, also implies a reasonable prediction of the various physical features in the surrounding flowfield.

The strength of our sharp-edge vortex can be defined in variety of different ways. The most conventional measure of vortex strength throughout the literature is the vortex circulation (Γ_v), which is believed to be inherently linked to the velocity field induced by the vortex. Circulation is formally defined as the line integral of velocity over the boundary of the vortex, but is more commonly calculated via an area integral of vorticity within the vortex core:

$$\Gamma_v = \int_S \omega_z \mathrm{d}A, \tag{3.2}$$

where S is a spatial region encircling the vortex in question. Although the sharp-edge vortex does have a clearly defined boundary, our experimental measurements are not very well-suited to the use of equation 3.2, as a portion of the vorticity field near the blade surface is obscured by laser reflection. The current work thus makes use of an alternate method for calculating the circulation of the sharp-edge vortex that does account for the "missing" vorticity in figure 3.6.

Our method of estimating circulation consists of three steps. First, one selects a flowfield snapshot of interest, and calculates the "center" of the sharp-edge vortex at that particular time using the well-known Γ_1 criterion. The Γ_1 criterion physically

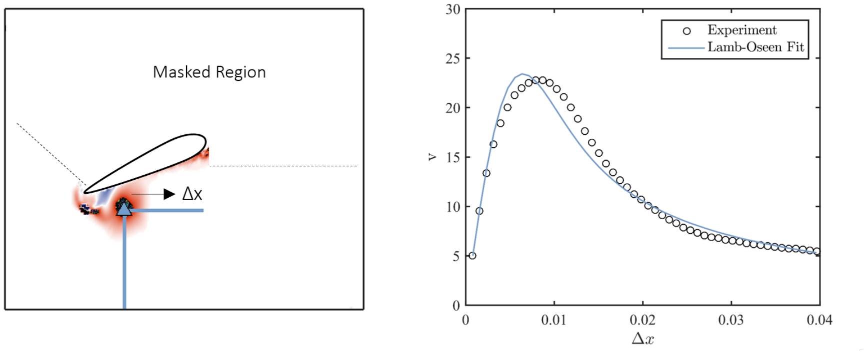

Figure 3.7: Illustration of the calculation of vortex strength, including the vortex center (blue triangle), the resulting lines, and the Lamb-Oseen curve fit.

represents a measure of the local rotation surrounding a certain point in the flowfield, and can be formally defined according to equation 3.3:

$$\Gamma_1 = \frac{1}{A}\int_A \sin\phi \mathrm{d}A, \tag{3.3}$$

where A is a small area of integration surrounding a given point, and ϕ is the angle between the position and velocity vector. For a given snapshot, the vortex center is estimated based on a local maximum in Γ_1 and visually confirmed to coincide with the approximate center of the sharp-edge vortex.

The next step of this process involves drawing two lines, each of roughly $c/2$ in length, from the center of the vortex. One line is drawn in the chordwise direction, extending toward the blunt-edge of the blade, and the second line is drawn in the vertical direction, extending below the surface of the wing. A sample flowfield snapshot featuring both the vortex center and the resulting lines is provided in figure 3.7 as an example. The flow perpendicular to each line can then be seen as an estimate of the local velocity induced by the sharp-edge vortex at a given time.

As mentioned above, the induced velocity is inherently tied to the circulation of the vortex itself, a relation for which several models exist in the literature. The current work makes use of the Lamb-Oseen model of a rotation vortex, defined according to:

$$u_\theta = \frac{\Gamma_v}{2\pi x}\left(1 - e^{x^2/x_c^2}\right), \tag{3.4}$$

where u_θ corresponds to the velocity induced by the vortex; Γ_v corresponds to the circulation; x is the distance (in either direction) from a given point to the center of the vortex; and x_c is a vortex core radius that results from the fit. Note that the velocity induced by the sharp-edge vortex does not necessarily adhere exactly to the form given by equation 3.4. In reality, the sharp-edge vortex is distorted by the it proximity to the blade surface, meaning the vortex does not induce a symmetric velocity field about its center. Below the vortex center, however, the Lamb-Oseen model does a decent job fitting the velocity induced by the vortex, as indicated in the sample fit on the right-hand side of figure 3.7.

The circulation of the sharp-edge vortex can be backed out of equation 3.4 by fitting a curve to the velocity induced along each line. The final vortex strength at a given time is then determined by averaging the circulation computed for each of the two lines emanating from the vortex center. If this calculation procedure is repeated at each of the available flowfield snapshots for a given flight condition, one arrives at a quantitative measure for the growth of the sharp-edge vortex throughout the reverse flow region.

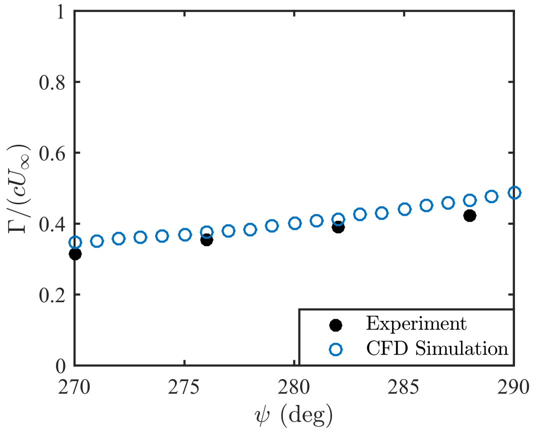

Figure 3.8: Comparison of the circulation in the sharp-edge vortex for the experimental measurements (black dots) and the CFD simulation (blue dots) at the primary forward flight condition of the rotor ($\mu = 0.60$, $\theta_0 = 10°$, $r/R = 0.45$).

3.3.3 Vortex Strength Comparison

Figure 3.8 shows the results of computing the circulation of the sharp-edge vortex for the experimental measurements (black dots) and the CFD simulations (blue dots). In this figure, azimuthal position is plotted on the abscissa, and vortex strength, computed via the Lamb-Oseen curve fitting method for both data sets, is plotted on the ordinate. The comparison of figure 3.8 suggests that the CFD is able to quite accurately capture the quantitative evolution of the sharp-edge vortex in the primary forward flight condition; the experimental and numerical simulations exhibit very close agreement over a broad portion of the reverse flow region. The slight overprediction of the blade incidence in the CFD, which was seen to slightly increase to the magnitude vorticity near the core, is ultimately shown to be a small source of error in the growth of the sharp-edge vortex. Based on figure 3.8, one can conclude that our numerical simulations provide a reasonable estimate of how the sharp-edge vortex, and the various mechanisms that govern its growth, evolve throughout the reverse flow region.

As a final comment, we will note that the validation procedure described above provided quite good results for the sharp-edge vortex, but less so for the blunt-edge vortex. Figure 3.6 revealed that the CFD was unable to qualitatively capture the strength and convection behavior of the blunt-edge vortex, and our subsequent attempts to quantitatively compare the strength of this flow structure to experimental measurements did not produce particularly close results. The CFD simulation will thus only be used to investigate how the sharp-edge vortex evolves and behaves over time. Figure 3.8 does, however, suggest that the growth of the sharp-edge vortex is relatively independent of the prediction of the blunt-edge vortex, at least for the primary condition of the rotor, meaning the CFD simulation can still considered to be generally valid for the flow structure at the sharp edge.

3.4 Chapter Summary

The purpose of this chapter was to introduce the basic flow structures and gradients present in the reverse flow region of a rotor at high advance ratio. From flowfield measurements of a baseline condition of rotor system, this chapter identified (1) a “blunt-edge” vortex believed to form prior to the blade’s transition into reverse flow, and (2) a “sharp-edge” vortex seen to result from flow separation about the sharp geometric trailing edge of the blade section. We were also able to identify, via three-component flowfield measurement techniques, an inboard-pointed gradient in vorticity and a tip-to-root spanwise flow through the core of the sharp-edge vortex. Together, these flow structures, and their associated 3-D gradients, represent the basic flow morphology that will be studied in the sections to come.

In addition, the baseline flow morphology outlined experimentally was compared, both qualitatively and quantitatively, with the results of a numerical simulation of the same rotor system at the same forward flight condition. The CFD simulation exhibited rather good agreement with the experimental flowfields in terms of the strength of the sharp-edge vortex. This has important ramifications for the sections that follow, as the CFD, with its high volumetric resolution, can be quantitatively analyzed as a reasonable approximation of the real flow. Chapter 5 of this thesis will make use of this high-fidelity numerical simulation to quantify the role of various 2-D and 3-D mechanisms of vorticity transport in the development of the sharp-edge vortex, a task that could not be accomplished from the experimental measurements alone. Chapter 6 will then focus on the origin and formation of the blunt-edge vortex.

Chapter 4: Analysis of the Sharp-Edge Vortex

The previous section identified two distinct vortical structures in the reverse flow region of a rotor at high advance ratio: one vortex that forms at the sharp edge of the rotor blade, and one vortex that forms at the blunt edge of the rotor blade. The purpose of this chapter is to address the physics of the sharp-edge vortex and to gain an understanding of what flow mechanisms have the most significant impact on its growth. Having been validated with experimental measurement, the numerical simulations are uniquely posed to accomplish this task, as their high spatial resolution allows for the calculation of various 3D flow properties that are difficult to obtain experimentally. The ensuing analysis will employ a vorticity transport analysis to directly quantify the relative importance of 2D and 3D vortex dynamics on a rotor operating in forward flight. In addition, this chapter will serve as a guide for which mechanisms of the flow are most important to modeling efforts, identifying what physics (if any) can be neglected in a low-order representation of the reverse flow region.

4.1 The Vorticity Transport Equation

Before the more detailed rotor analysis can take place, it is first important to review the exact physical mechanisms that impact the evolution of a vortex in a 3D flow environment. This introductory section will provide a fundamental, conceptual review of vorticity transport in three dimensions, while the next section will apply these concepts to the case of a rotor blade element in high advance ratio forward flight. The term "vorticity transport" here refers to the notion that the total vorticity in a flow is conserved over time, just as mass, momentum, and energy are conserved in the governing equations of fluid dynamics. A mathematical expression for vorticity transport is advantageous because it can be written in a way that identifies where vorticity is generated and where it is convected. In the case of the sharp-edge vortex, for example, it was qualitatively clear in Chapter 3 that vorticity was generated at the sharp edge of the rotor blade element as it passed through reverse flow, but it was less clear how much of that vorticity actually accumulated in the sharp-edge vortex. This section will derive an expression for vorticity conservation (similar to the expression derived by Wojcik and Buchholz [86] and Eldredge and Jones [97]) that allows for the quantification of 2D and 3D flow mechanisms on the transport of vorticity, with the intent of employing this expression in the analysis of the sharp-edge vortex.

Any expression of vorticity conservation can be traced back to a specific form of the standard momentum equation. This relation, often called the "vorticity equation" in fluid dynamics textbooks, is derived by taking the curl of the incompressible

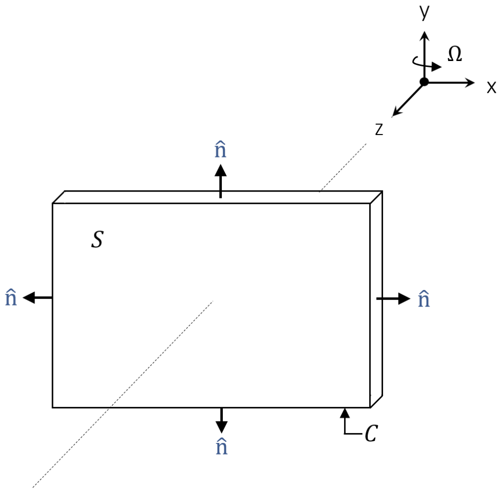

Figure 4.1: Definition of a rectangular control volume for illustration of vorticity transport in 3D.

Navier Stokes equation. It can be stated in a rotating reference frame as follows:

$$\frac{\partial \overrightarrow{\omega}}{\partial t} + \overrightarrow{u} \cdot \nabla \overrightarrow{\omega} = \overrightarrow{\omega} \cdot \nabla \overrightarrow{u} + \nabla \times \left(2\overrightarrow{\Omega} \times \overrightarrow{u}\right) + \nu\left(\nabla \times \nabla^2 \overrightarrow{u}\right), \qquad (4.1)$$

where $\overrightarrow{\omega}$ is the local vorticity vector in a rotating frame, $\overrightarrow{u}$ is the local velocity vector in a rotating frame, and $\overrightarrow{\Omega}$ represents the rotation vector for the reference frame of interest. Although fundamental, equation 4.1 does not offer many intuitive physical insights in its current form, as it expresses vorticity conservation for an individual fluid element. The physical interpretation of each term in equation 4.1 becomes much more meaningful when this expression is integrated over a finite region in space. To illustrate this idea, consider a planar, rectangular control volume, such as the one shown in figure 4.1. The control volume is defined by the exterior contour C, has surfaces normals $\hat{n}$, and occupies an area S. The coordinate system $[x, y, z]$

defines the position of the control volume in a frame continuously rotating about the vertical y-direction, such that the area vector is always defined as $\overrightarrow{S} = S\hat{z}$. For the purposes of this analysis, the control volume will also be assumed to contain some amount of vorticity, with the local vorticity vector having components in the x, y, and z direction.

Let us consider an expression of vorticity conservation for the z component of vorticity, or the "spanwise" component, for the control volume shown in figure 4.1. If the convection and tilting/stretching terms are expanded, the z-component of equation 4.1 can be written as follows:

$$\frac{\partial \omega_z}{\partial t} + \nabla_{2D} \cdot \left(\overrightarrow{u_{2D}}\omega_z\right) = \nabla_{2D} \cdot \left(u_z \overrightarrow{\omega_{2D}}\right) - \nabla \times \left(2\overrightarrow{\Omega} \times \overrightarrow{u}\right) \cdot \hat{z} + \nu\left(\nabla \times \nabla^2 \overrightarrow{u}\right) \cdot \hat{z}, \quad (4.2)$$

where the "2D" subscript denotes terms that include only the x and y components of velocity or vorticity (i.e., $u_{2D} = u_x\hat{x} + u_y\hat{y}$ and $\omega_{2D} = \omega_x\hat{x} + \omega_y\hat{y}$). If equation 4.2 is integrated over the area S, each divergence term can be transformed to a surface flux via the divergence theorem, and each cross-product term can be written as a simple line integral via Stokes theorem. This leads to a statement of vorticity conservation that will be frequently referenced in the current work:

$$\int_S \left(\frac{\partial \omega_z}{\partial t}\right) \mathrm{d}S = -\oint_C \omega_z \left(\overrightarrow{u_{2D}} \cdot \hat{n}\right) \mathrm{d}C + \oint_C u_z \left(\overrightarrow{\omega_{2D}} \cdot \hat{n}\right) \mathrm{d}C - \oint_C \left(2\overrightarrow{\Omega} \times \overrightarrow{u}\right) \cdot \overrightarrow{\mathrm{d}l} + \nu \oint_C \nabla^2 \overrightarrow{u} \cdot \overrightarrow{\mathrm{d}l}, \quad (4.3)$$

Equation 4.3 is a far more intuitive statement of vorticity conservation. It represents a simple relation between the time rate of change of circulation within the control volume (left-hand side) and the transport of vorticity due to various 2D and 3D mechanism of the flow (right-hand side). These mechanisms include the 2-D convection of vorticity (first term on the right-hand side of equation 4.3), the 3D convection and tilting of vorticity (second term), the transport of vorticity due to Coriolis forces (third term), and the viscous diffusion of vorticity (fourth term), . Each term has some finite impact on the convection of the individual elements of vorticity in the flow, and their combined effect determines how much vorticity is transported into and out of the control volume over a given period of time.

Equation 4.3 will play a significant role in the analysis of the sharp-edge vortex on a high advance ratio rotor. It is thus very important that each term in equation 4.3 is properly understood before moving forward. Figure 4.2 provides a series of simple sketches that cement the physical significance of each term in equation 4.3. The 2-D convection term is addressed first and is illustrated in figure 4.2(a). This term corresponds to the flux of z-vorticity (ω_z) through the edges of the control volume due to velocities in the x-y plane. A positive value of the integral in equation 4.3 represents the convection of positive vorticity into the control volume, while a negative value corresponds to the convection of positive vorticity out of the control volume.

The second term on the right-hand side of equation 4.3, the 3-D transport term, is somewhat more difficult to visualize. Its physical significance can be more easily explained by decomposing the term into equivalent area integrals, a derivation of which is formally outlined in reference [86] and [98]:

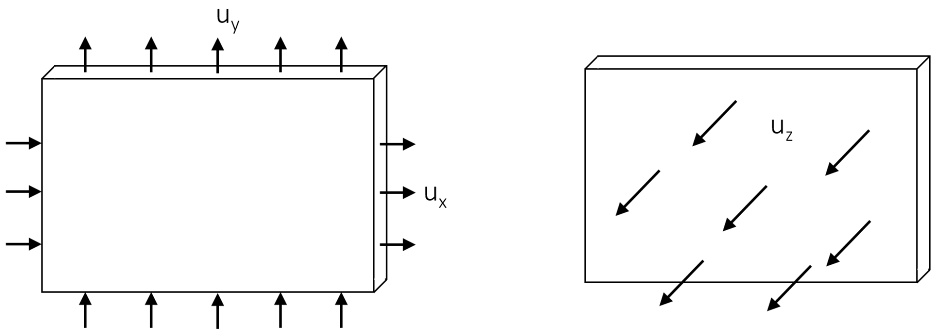

(a) The 2-D convection of vorticity. (b) The spanwise convection of vorticity.

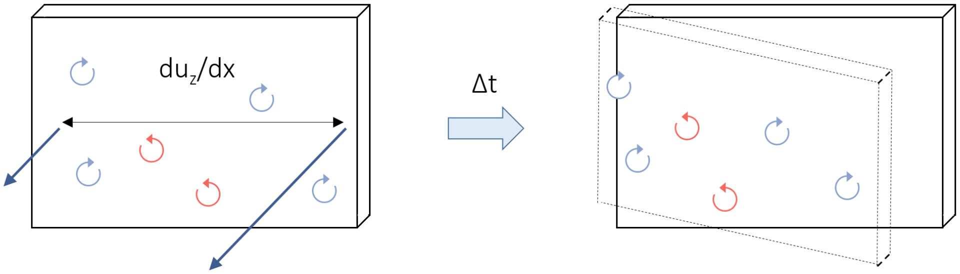

(c) The tilting of vorticity due to gradients in spanwise flow.

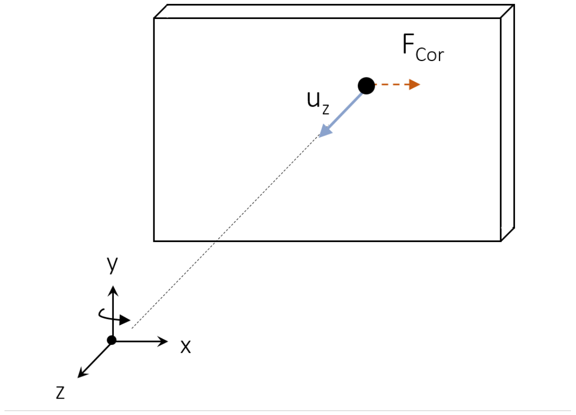

(d) Vorticity transport due to Coriolis forces.

Figure 4.2: Illustration of the various 2D and 3D mechanisms of vorticity transport at play on an arbitrary rotating control volume.

$$\oint_C u_z\left(\overrightarrow{\omega_{2D}}\cdot\hat{n}\right)\mathrm{d}C = \int_S u_z\frac{\partial\omega_z}{\partial z}\mathrm{d}A + \int_S\left(\overrightarrow{\omega_{2D}}\cdot\nabla_{2D}u_z\right)\mathrm{d}A \tag{4.4}$$

In the equation above, the total 3-D vorticity transport is revealed to consists of a spanwise convection term (first integral on the right-hand side of equation 4.4) and a vortex tilting term (second integral). The spanwise convection term, the action of which is illustrated in figure 4.2(b), effectively represents a z-direction flux of vorticity, or how much vorticity is brought into or out of a planar control volume by the action of spanwise flow. The vortex tilting term, or the second component of 3-D transport, accounts for the notion that spatial gradients in spanwise flow result in a re-orientation of the local vorticity vector. Consider, as an example, the simple linear variation in spanwise flow demonstrated in the left side of figure 4.2(c) for a control volume containing only ω_z vorticity. After a short time, vorticity elements on the left side of the the control volume convect a shorter distance than elements on the right hand side; the plane that encompasses the original vortex elements (and in turn the direction of the local vorticity vector) is no longer aligned with the z axis after a short time Δt. For a fixed control volume, this process ultimately manifests as ω_z vorticity being continuously re-distributed as either ω_x or ω_y, the amount of which depends on the direction of the gradients in spanwise flow.

The third term on the right-hand side of equation 4.3 quantifies the impact of Coriolis forces on individual fluid elements within the control volume. This term arises when the governing equations of fluid motion are applied in a rotating frame of reference. Conservation laws are only strictly valid in an inertial, non-accelerating frame, and thus the Coriolis force can be seen as a fictitious “correction” from a non-inertial frame to an inertial frame. As an example, imagine a fluid element with only a spanwise velocity in the rotating frame, such as the one shown in figure 4.2(d). The “true” velocity, or inertial velocity, of this fluid element also has an x-component, but to an observer in the rotating frame, this velocity component is not evident due to the motion of the control volume. A fictitious x Coriolis force is included in the rotating frame to account for this discrepancy between inertial and non-intertial observers. In the context of vorticity convection, gradients in Coriolis force lead to an unequal balance of forces on a fluid element in the rotating frame, potentially causing a significant change in the local value of vorticity.

The final term in equation 4.3 corresponds to the viscous diffusion of vorticity within the control volume. For the relatively high Reynolds number flows considered here, this term is expected to be quite small, except in regions of the flow close to solid boundaries. If an edge of the control volume in figure 4.1 were to coincide with a solid wall, the viscous term in equation 4.3 would include the diffusion of vorticity generated at the wall due to the action of the surface pressure gradient [87, 88, 99]. In this way, the viscous term in equation 4.3 can be seen to represent the generation of vorticity at a solid boundary and the ensuing diffusion of that vorticity into the surrounding flow. By virtue of its relation to vorticity generation, the viscous term cannot be neglected in many analyses of vorticity transport, even for very high Reynolds number flows.

Table 4.1: The “baseline” forward flight condition used in the vorticity transport analysis of the sharp-edge vortex.

μ	θ_0	θ_{1s}	θ_{1c}	RPM
0.80	11°	-12.69°	2.09°	700

4.2 Vorticity Transport in the Baseline Case

Having provided a basic background on vorticity transport, the next step of this analysis is to apply the concepts of vorticity conservation to the sharp-edge vortex found on a rotor in forward flight. Table 4.1 provides a recap of the forward flight condition of the rotor that will serve as the “baseline” case in our analysis of the sharp-edge vortex. The advance ratio of this case ($\mu = 0.80$) was chosen such that the sharp-edge vortex, and the 3-D gradients associated with it, have sufficient time to grow and develop as the rotor blade passes through reverse flow. Figure 4.3 shows a flowfield snapshot of the 45% radial station mid way through the reverse flow region ($\psi = 270°$) for the baseline forward flight condition ($\mu = 0.80, \theta_0 = 11°$) as computed by the CFD simulation. The flowfield presented is in a rotating reference frame [x, y, z] and is overlain by contours of spanwise vorticity (ω_z). The figure highlights the presence of a feeding shear layer and a region of secondary vorticity as a recap of the basic flow structure originally presented in Chapter 3.

Much like the previous section, the mechanisms of vorticity transport can be examined in this flow by first constructing a planar control volume in the rotor frame

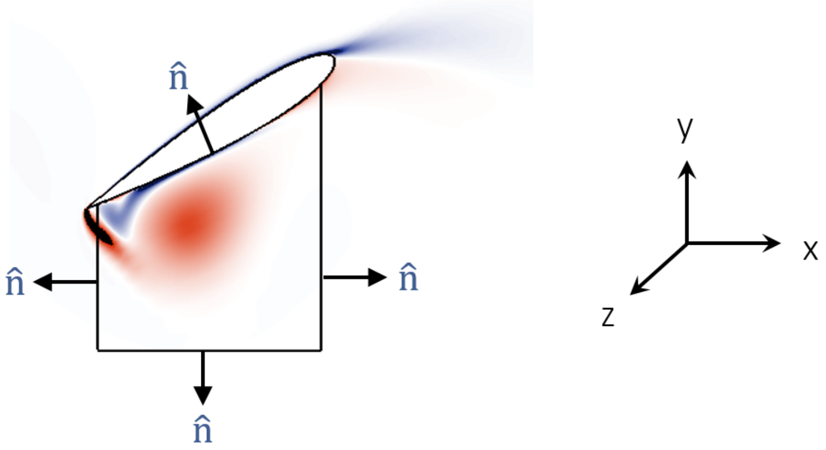

Figure 4.3: Definition of a planar control volume emanating from the lower surface of the rotor blade at $r/R = 0.45$. The control volume has surface normals $\hat{n}$, area S, and boundaries defined by C.

of reference. A sketch of the control chosen for this work is provided in figure 4.3. This control volume was defined such that the upper surface of the control volume coincided with the suction surface of the blade over a spatial region that includes the sharp-edge vortex for much of the blade's passage through reverse flow. Any transport of vorticity into or out of the control volume, then, can be seen as the transport of vorticity into or out of the sharp-edge vortex. An expression for the conservation of vorticity in this control is provided in the equation below:

$$\frac{\mathrm{d}\Gamma}{\mathrm{d}t} = \sum_C \omega_z \left(\overrightarrow{u} \cdot \hat{n}\right) \Delta s + \sum_C u_z \left(\overrightarrow{\omega} \cdot \hat{n}\right) \Delta s - \sum_C \left(2\overrightarrow{\Omega} \times \overrightarrow{u}\right) \cdot \hat{t} \Delta s + \nu \sum_C \left(\nabla^2 \overrightarrow{u} \cdot \hat{t}\right) \Delta s, \tag{4.5}$$

where $\hat{n}$ is the local surface normal vector, $\hat{t}$ is the local surface tangent vector, and Δs is an incremental distance along the contour. Evaluating each of the discrete summations on the right-hand side of equation 4.5 allows one to extract the contri-

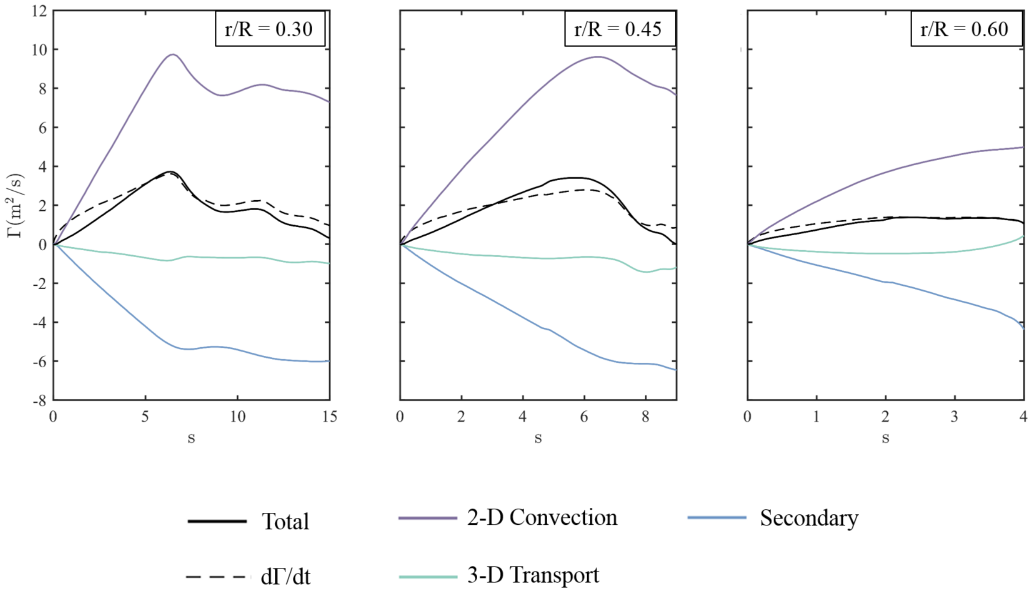

Figure 4.4: The contribution of 2-D convection, secondary vorticity, and 3-D vortex dynamics to the strength of the sharp-edge vortex for three radial stations ($0.30 \leq r/R \leq 0.60$) at the baseline forward flight condition ($\mu = 0.80$, $\theta_0 = 11°$)

bution of 2-D convection, 3-D transport, Coriolis forces, and the viscous generation of vorticity within the control volume, ultimately illustrating the interplay between the various mechanisms of vorticity transport in the evolution of the sharp-edge vortex.

Figure 4.4 plots the results of evaluating equation 4.5 for the baseline case and shows the contribution of each physical flow mechanisms to the total circulation within the control volume at various radial stations in the reverse flow region. In each subfigure, reduced time (i.e., the number of semi-chords traveled by each rotor blade element in reverse flow) is plotted on the abscissa, and the transport of circulation due to each flow mechanism is plotted on the ordinate. The contribution due to 2-D convection is plotted in purple; the contribution due to viscous generation along the surface is plotted in blue; and a net 3-D effects term, which groups spanwise convection, vortex tilting, and Coriolis forces into one term, is plotted in green. The total influx of circulation, computed by summing each contribution together, is represented by the solid black line, while a reference value of circulation, calculated via a line integral of the velocity field, is included as a dashed black line. Note that the solid and dashed black lines do not perfectly overlap; this inconsistency is attributed to the exclusion of turbulent stresses from equation 4.5 and from evaluating the viscous term only along the blade surface.

The leftmost plot in figure 4.4 shows the circulation contributions at $r/R = 0.30$ and illustrates the general behavior of each transport mechanism in reverse flow. The 2-D convection term (purple line) adds significant positive circulation to the control volume as the shear layer feeds the sharp-edge vortex during its growth. An opposite-signed vorticity (blue line) diffuses into the flow as a consequence of the no-slip condition along the lower surface of the rotor blade, and follows the same basic trend as the 2-D convection term. The combined 3-D effects term (green line), a combination of spanwise convection, vortex tilting, and Coriolis forces, maintains a small magnitude throughout the evolution of the sharp-edge vortex. This process, wherein the total circulation is dominated by shear layer vorticity and secondary vorticity, is also evident at $r/R = 0.45$ and $r/R = 0.60$.

Figure 4.4 appears to imply that 3D effects play a small role in vorticity transport throughout the entire reverse flow region, but one must keep in mind that figure 4.4 represents a time-integrated version of the vorticity transport equation. As an alternate approach to viewing vorticity transport, figure 4.5 plots the time rate

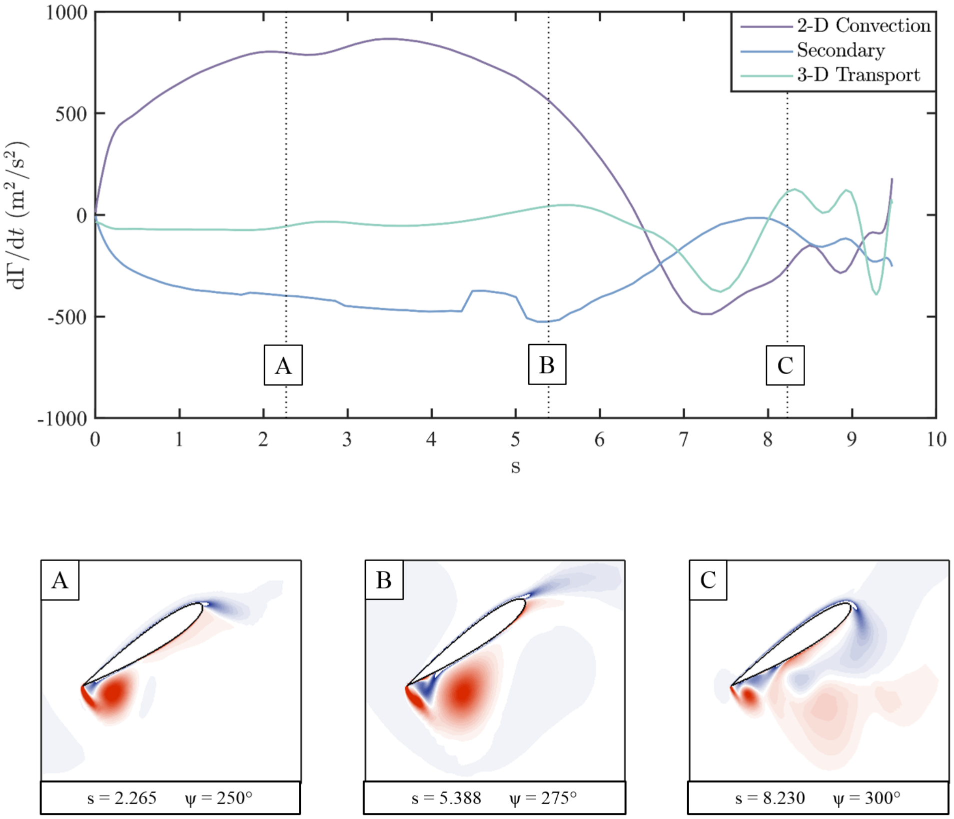

Figure 4.5: The contribution of 2-D convection, secondary vorticity, and 3-D vortex dynamics to the time rate of change of vorticity ($\mathrm{d}\Gamma/\mathrm{d}t$) for $r/R = 0.45$ at the baseline forward flight condition ($\mu = 0.80$, $\theta_0 = 11°$)

of change of circulation ($\mathrm{d}\Gamma/\mathrm{d}t$), or the derivative of the quantity from figure 4.4, for the 45% radial station as it travels through reverse flow. This figure is included as a way of recovering any information that may have been lost in the time-integration of equation 4.5, and it captures the *instantaneous* magnitude of vorticity transport due to 2-D convection, viscous generation, and 3-D effects. A series of flowfield snapshots is included beneath the plot in figure 4.5 as a reference for the state of the flow at various points in the evolution of the vorticity transport terms.

The early portion of figure 4.5 ($s \leq 7.0$), which corresponds to the growth stage of the sharp-edge vortex (flowfield snapshots A and B), reveals a familiar trend in the behavior of the various mechanisms of vorticity transport. The 2-D convection term (purple line) acts to add positive circulation to the control volume, the generation term (blue line) acts to add negative circulation near the blade surface, and the combined 3D effects term (green line) remains quite small. This behavior persists until roughly $s = 7.0$, at which point the sharp-edge vortex "bursts." In this state, the flow becomes disorganized, the vortex no longer has a recognizable "core," and the magnitude of the 3-D effects term begins to undergo oscillations of a significant magnitude [98, 100, 101]. These oscillations do not result in a large net transport of circulation, as the time-integrated 3-D effects term remains small throughout figure 4.4, but can lead to redistribution of vorticity that significantly alters the ensuing evolution of the flowfield. In this way, the combined 3-D effects term can only be seen as small only if the vortex is still coherent, or if the vorticity field is not in a state of disorganization.

The remainder of this chapter focuses on the growth stage of the sharp-edge vortex, or the portion of the reverse flow region that precedes the onset of vortex burst ($s \leq 7.0$ in figure 4.5). The latter portions of the reverse flow region, or those that resemble a disorganized wake, are not expected to have as dramatic of an impact on the rotor blade loads and are difficult to model in a non-empirical fashion. The growth stage of the sharp-edge vortex, however, still represents a significant portion of the reverse flow region, and will be studied at length in the following sections, beginning with the impact of 3-D effects on this period of vortex growth.

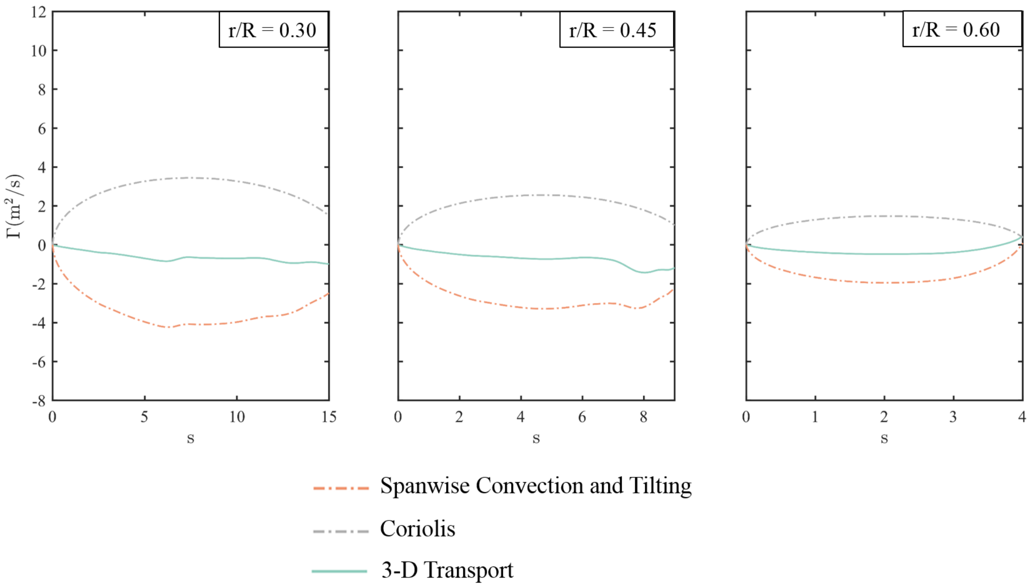

Figure 4.6: The contribution of spanwise convection/vortex tilting and Coriolis forces to the total 3-D vortex dynamics for three radial stations ($0.30 \leq r/R \leq 0.60$) at the baseline forward flight condition ($\mu = 0.80$, $\theta_0 = 11°$)

4.3 3-D Effects in the Baseline Case

In the previous section, figure 4.4 appeared to suggest that 3-D vorticity transport mechanisms play a small, almost negligible role during the growth stage of the sharp-edge vortex. Even prior to vortex burst, this is a somewhat unexpected result. Chapter 3 found that the core of the sharp-edge vortex is characterized by substantial spanwise flow throughout the reverse flow region, and several 3-D mechanisms of vorticity transport (namely, the spanwise convection and Coriolis terms) scale directly with the magnitude of spanwise flow. Figure 4.6 attempts to address this discrepancy by breaking the combined 3-D effects term (i.e., the green line in figure 4.4) into its constituent components. Again, reduced time is plotted on the abscissa in figure 4.6, but each line now corresponds to the the total circulation transported into or out of the sharp-edge vortex due to either spanwise convection/vortex tilting (orange line) or Coriolis forces (grey line). The green line, representing the combined 3-D effects in the flow, is simply the sum of the orange and grey lines and is included in figure 4.6 as a reference.

Figure 4.6 reveals that the individual components of the 3-D effects term are not necessarily small, but their directions are oriented such that the net impact of 3D effects on vortex growth is minimal. The spanwise convection/tilting term, for instance, acts as a vorticity "sink," meaning it contributes a negative circulation to the control volume, and carries a similar order of magnitude as the 2-D convection convection term. The Coriolis term, meanwhile, acts as a "source" of vorticity and is also roughly of O(1). Figure 4.6 shows these two terms are oriented opposite of one another in the reverse flow region. If the two terms are roughly the same order of magnitude, as they are in figure 4.6, this phenomenon results in the mutual cancellation of the spanwise convection/tilting term and the Coriolis term. The combined influence of these two mechanisms is in turn an order of magnitude lower than the 2-D convection of vorticity, and the net contribution of 3-D effects to vortex growth in reverse flow is quite small – despite the presence of a significant spanwise flow.

At this stage, it is important to recognize that the main conclusion derived from figure 4.4 and 4.6 (i.e., that 3-D effects are unimportant to vortex evolution in reverse flow) is at odds with previous studies that address the impact of rotation on vortex growth. These works, which nearly universally deal with a rotating wing in hover, generally agree that the presence of rotation has a "stabilizing" effect on sharp-edge vortices, such that the shedding of a vortex is delayed on a rotating wing when compared to an equivalent rectilinear motion [98, 102, 103, 104]. The discrepancy between hover, where 3-D effects have a notable impact, and reverse flow, where 3-D effects appear to be insignificant, can be addressed by comparing the direction of 3-D vorticity transport in the two configurations. Consider as a starting point a simplified expression for Coriolis transport on the sharp-edge vortex, given by equation 4.6:

$$-\oint_C \left(2\overrightarrow{\Omega} \times \overrightarrow{u}\right) \cdot \overrightarrow{\mathrm{d}l} = -2\Omega \int_{C_2} u_z \mathrm{d}l, \tag{4.6}$$

where C_2 corresponds to the bottom edge of the control volume sketched in figure 4.3. The purpose of equation 4.6 is to illustrate that the net vorticity transport due to Coriolis force is oriented with the negative of the spanwise flow direction ($-u_z$). This orientation is true for a sharp-edge vortex in both hover and in the reverse flow region of a rotor in forward flight.

Next, consider an expression for the convection of vorticity along the blade span, given by equation 4.7. As discussed in section 4.1, this expression is contained within the spanwise convection/tilting term and determines the direction of the orange line in figure 4.6.

$$\int_S -u_z \left(\frac{\partial \omega_z}{\partial z}\right) \mathrm{d}A \tag{4.7}$$

In equation 4.7, the orientation of the spanwise convection term is shown to depend

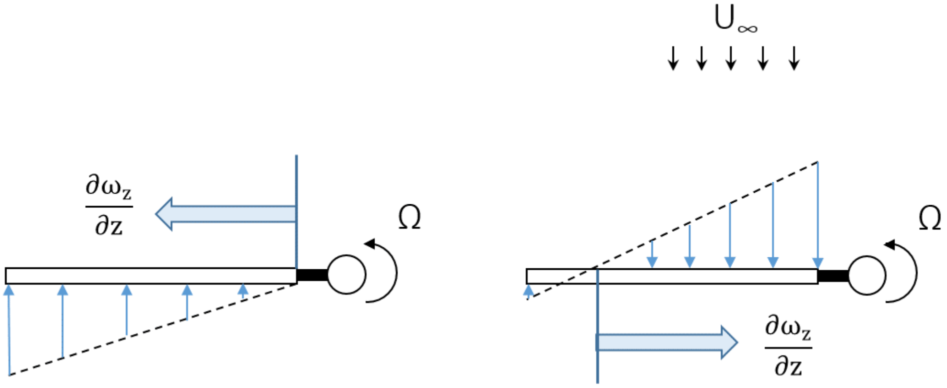

(a) Hover. (b) Reverse flow.

Figure 4.7: The direction of spanwise vorticity gradients in hover and reverse flow.

on both the direction of spanwise flow (u_z) and the direction of the spanwise gradient in vorticity ($\partial\omega_z/\partial z$). Figure 4.7 illustrates the orientation of the spanwise vorticity gradient in hover versus reverse flow. In hover, the spanwise gradient in vorticity is pointed outboard, in the $+z$ direction, since the local freestream increases as one moves outboard. The spanwise convection term is thus aligned with the negative of the spanwise flow, just like the Coriolis term; spanwise convection and Coriolis transport then act in the same direction and result in a large net 3D effect on the developing vortex. In reverse flow, the direction of the spanwise gradient in vorticity is flipped. Because the magnitude of the local freestream increases as one moves inboard in reverse flow, the spanwise gradient in vorticity is pointed inboard, in the $-z$ direction, and the spanwise convection term is now aligned with the positive of the spanwise flow. Thus, the reverse flow region sees the Coriolis and spanwise convection terms *opposing* one another due to the direction change in vorticity gradient, a phenomenon that is expected to occur in the reverse flow region at any arbitrary forward flight condition.

4.4 Generalizing Vorticity Transport in Reverse Flow

The preceding section uncovered a unique feature of vorticity transport in the reverse flow region of a rotor in forward flight: the spanwise convection and Coriolis transport terms are oriented in directions that oppose one another. If the magnitude of these two terms is roughly equal, as was the case for the baseline forward flight condition (see figure 4.6), the combined impact of 3-D vorticity transport is negligible in reverse flow, and the growth of the sharp-edge vortex is governed by 2-D flow mechanisms alone. One must keep in mind, however, that the similar magnitude of spanwise convection and Coriolis effects has thus far been observed only for the baseline case ($\mu = 0.80$, $\theta_0 = 11^\circ$); it remains unclear whether one can expect a cancellation of these terms at other flight conditions and blade geometries. This section will attempt to generalize the physics of vorticity transport in the reverse flow region and comment on where in the parameter space 3-D effects are expected to have an insignificant impact on vortex growth.

The ultimate goal of this section is to arrive at some non-dimensional parameter, based only on the forward flight conditions and the properties of the rotor, that will allow one to predict the importance of 3-D effects on the development of the sharp-edge vortex. This goal can be achieved by backing out a parameter that reflects the relevant physics of the reverse flow region. Recall that in the case of reverse flow, 3-D effects were found to be negligible when the spanwise convection and Coriolis components of the vorticity transport equation were roughly of the same magnitude. The ratio of these two components, then, can be seen as a strong indicator of whether 3-D effects will be significant. The following series of equations introduces a non-dimensional ratio of the Coriolis and spanwise convection terms:

$$\frac{Co}{Sp}, \tag{4.8}$$

where Co and Sp are abbreviations for the Coriolis and spanwise convection/tilting integrals, respectively, and are defined according to the following expressions:

$$Co = \oint_C \left(2\overrightarrow{\Omega} \times \overrightarrow{u}\right) \cdot \overrightarrow{\mathrm{d}l}, \tag{4.9}$$

$$Sp = \oint_C u_z \left(\overrightarrow{\omega}_{2D} \cdot \hat{n}\right) \mathrm{d}C. \tag{4.10}$$

If the ratio presented in equation 4.8 is roughly O(1), one can reasonably expect that the Coriolis and spanwise convection/tilting terms will be approximately equal and oriented opposite one another, and the combined 3-D effects term will be small. The remainder of this section is devoted to simplifying the ratio Co/Sp into an expression that can be easily predicted based on the forward flight condition of the rotor, and thus identifying a simple metric that indicates the relative importance of 3-D effects in the growth of the sharp-edge vortex.

4.4.1 The Coriolis Term

Let us begin by attempting to simplify the Coriolis term stated in equation 4.9. The cross-product contained within the integrand of this term can be expanded to $2\Omega\Big(u_z\hat{x} - u_x\hat{z}\Big)$ by noting that the rotation vector $\overrightarrow{\Omega}$ contains only a $\hat{y}$ term. If one also notes that the contour C is defined only in the x-y plane, the Coriolis term becomes:

$$Co = 2\Omega \int_{C_2} u_z \mathrm{d}l, \tag{4.11}$$

where again, C_2 is defined as the bottom edge of the control volume shown in figure 4.3. The fact that the net Coriolis effect can be determined knowing only the spanwise flow along C_2 is significant. As an illustration, the left-hand side of figure 4.8 shows a single snapshot of the spanwise flowfield at $r/R = 0.45$ with control volume C overlain atop. This figure illustrates that C_2, or the bottom edge of the control volume, is defined well outside the core of the sharp-edge vortex, and thus the spanwise flow along C_2 is nearly uniformly equal to the "background" spanwise flow incurred by the blade's orientation relative to the forward flight velocity of the rotor. With this in mind, the Coriolis term can now be further simplified to:

$$Co = 2\Omega \int_{C_2} u_z \mathrm{d}l \approx 2\Omega U_z L, \tag{4.12}$$

where U_z represents the magnitude of the "background" spanwise flow at a given time, and L represents the length of control surface C_2.

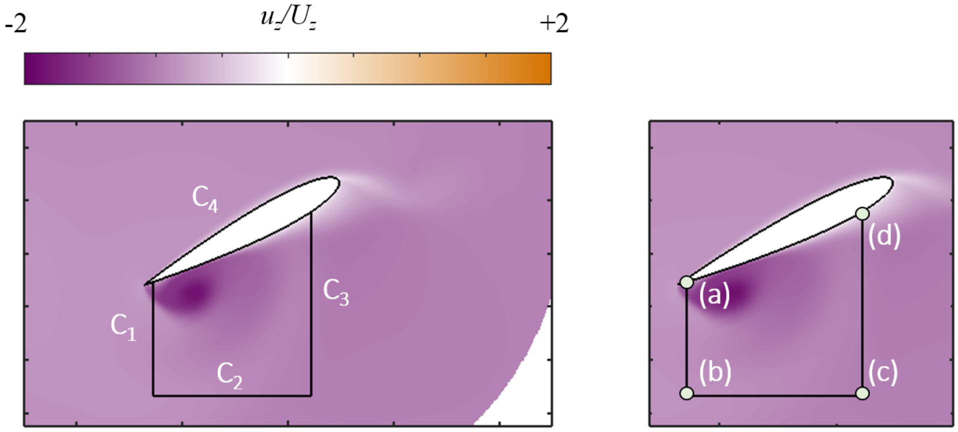

Figure 4.8: Definition of the control volume C overlain with contours of spanwise flow (u_z) for $r/R = 0.45$ at the baseline forward flight condition ($\mu = 0.80$, $\theta_0 = 11°$).

Figure 4.9 compares the simplified version of the Coriolis term, calculated by assuming u_z is constant (and equal to U_z) along C_2, with the actual integrated Coriolis term extracted from the baseline CFD simulation. The figure shows close agreement between equation 4.12 and the actual Coriolis transport, and suggests that $2\Omega U_z L$ is a very reasonable approximation of the net Coriolis transport in the sharp-edge vortex. The Coriolis term has thus been simplified to the point that each of the parameters in equation 4.12 can be extracted from the forward flight condition of the rotor. Consistent with the concept of a Coriolis force, equation 4.12 is dependent only on the rotation rate of the rotor and the instantaneous magnitude of spanwise flow, and does not show any dependency on radial station.

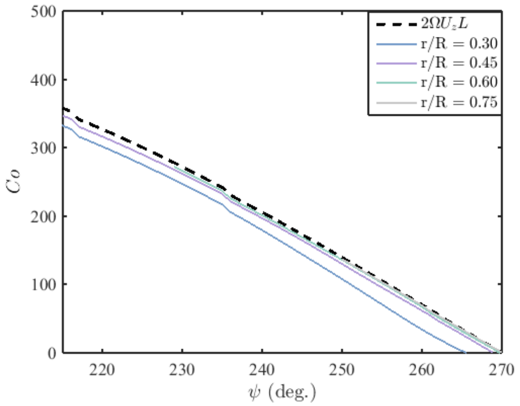

Figure 4.9: Evolution of the integrated Coriolis term (solid lines) and an analytical approximation (dashed line) for multiple radial stations at the baseline forward flight condition ($\mu = 0.80$, $\theta_0 = 11°$).

4.4.2 The Spanwise Convection/Tilting Term

Next, we will attempt a similar simplification of the spanwise convection/tilting term defined in equation 4.10. Unlike the Coriolis term, the integral in equation 4.10 does not lend itself to a clear-cut simplification, and will require a few physical assumptions in order to arrive at a usable expression.

Begin by noting that because of the no-slip condition at the surface of the blade, the value of the integrand in equation 4.10 is equal to zero everywhere along control surface C_4 (i.e., $u_z = 0$ along C_4). The spanwise convection/tilting term can now be rewritten using the following series of line integrals:

$$\oint_C u_z\Big(\overrightarrow{\omega_{2D}} \cdot \hat{n}\Big)\mathrm{d}C = \int_{C_2}\Big(-u_z\omega_y\Big)\mathrm{d}x - \int_{C_1}\Big(u_z\omega_x\Big)\mathrm{d}y + \int_{C_3}\Big(u_z\omega_x\Big)\mathrm{d}y, \quad (4.13)$$

where the appropriate component of vorticity has been included for each portion of

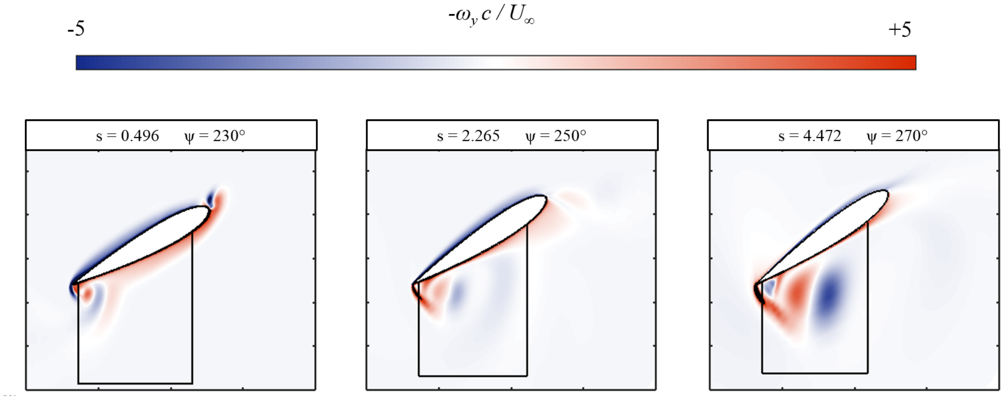

Figure 4.10: Flowfield snapshots showing contours of the y-component of vorticity in the reverse flow region for $r/R = 0.45$ at the baseline forward flight condition ($\mu = 0.80$, $\theta_0 = 11°$).

the contour integral. An analytical estimation of the net spanwise convection/tilting term can be found by approximating each of the line integrals in equation 4.13 individually.

Consider the first term on the right-hand side of equation 4.13 (i.e., the integral over C_2). The integrand of this term consists of two flowfield parameters. The first parameter, or the local spanwise flow (u_z), has already been discussed in relation to the control volume C; that is, the value of u_z was found to be reasonably constant along C_2 and equal to the "background" spanwise flow (U_z). The C_2 component of equation 4.13 can then be re-written as:

$$\int_{C_2} \Big(- u_z \omega_y \Big) \mathrm{d}x \approx -U_z \int_{C_2} \omega_y \mathrm{d}x, \tag{4.14}$$

where U_z is again equal to the "background" spanwise flow at a given time in the reverse flow region and is known from the forward flight condition alone.

The second parmater in the C_2 integral is the component of vorticity aligned with the vertical, defined as $\omega_y = \partial u_x/\partial z - \partial u_z/\partial x$. Compared to the more frequently-studied spanwise component of vorticity (ω_z), the evolution of the y-component of vorticity (ω_y) is not as intuitive, and it would thus be beneficial to briefly address how ω_y evolves throughout the reverse flow region. Figure 4.10 provides a series of ω_y contours for the 45% radial station at the baseline forward flight condition. This figure reveals two important sources of y-component vorticity in relation to our control volume C. The first is a bundle of adjacent positive/negative vorticity that occupies the same spatial region as the sharp-edge vortex. This vorticity is clearly visible in the $\psi = 250°$ and $\psi = 270°$ snapshots, and is believed to arise from the flow gradient (i.e., $\partial u_z/\partial x$) incurred by the presence of spanwise flow through the vortex core. The second is a negative "background" y-component of vorticity that persists throughout the flowfield, even outside the vortex core. This vorticity arises from the fact that our flowfields are presented in a rotating frame of reference, and the control volume itself is associated with its own y-vorticity equal to -2Ω, similar to the vorticity found in solid-body rotation.

Returning to the integral in equation 4.14, one may correctly note that the control surface C_2 is defined far from the core of the sharp-edge vortex. It is thus only subject to the "background" vorticity of -2Ω along its length. The ω_y term can now be assumed constant in equation 4.14, and the integral simplifies to:

$$-U_z \int_{C_2} \omega_y \mathrm{d}x \approx U_z \big(2\Omega\big) L, \tag{4.15}$$

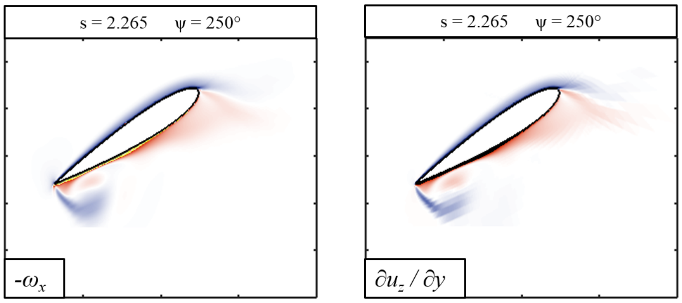

Figure 4.11: Flowfield snapshots showing contours of the x-component of vorticity (left) and contours of $\partial u_z/\partial y$ (left) in the reverse flow region for $r/R = 0.45$ at the baseline forward flight condition ($\mu = 0.80$, $\theta_0 = 11°$).

where again, L is the length of control surface C_2. With the expression above, the C_2 integral in equation 4.13 has been reduced to a simple analytical equation containing only terms from the flight condition.

Next, we will attempt to find a simplified expression for the second term on the right-hand side of equation 4.13, or the integral over C_1. This integral again consists of two terms: the local spanwise flow (u_z) and the x-component of vorticity, defined by $\omega_x = \partial u_z/\partial y - \partial u_y/\partial z$. As illustrated in figure 4.8, the control surface C_1 cuts through the shear layer located near the sharp edge of the blade, meaning neither u_z nor ω_x can be assumed to be constant along the length of C_1.

Thus, a physical assumption is needed in order to further simplify the integral over C_1. Toward this end, consider the individual gradients that make up the x-component of vorticity (i.e., $\partial u_z/\partial y$ and $\partial u_y/\partial z$). One may expect the in-plane gradient, $\partial u_z/\partial y$, to be of a substantially higher magnitude than the spanwise gradient, $\partial u_y/\partial z$, due to the proximity of the shear layer to the surface of the blade. Figure 4.11, which shows contours of ω_x (left-hand side) and contours of $\partial u_z/\partial y$

(right-hand side), provides support for this assumption. The two snapshots in figure 4.11 show nearly identical ω_x and $\partial u_z/\partial y$ contours, suggesting that contribution of $\partial u_y/\partial u_z$ is quite small compared to the total magnitude of ω_x. The x-component of the vorticity vector can now be reasonably simplified to the following form:

$$\omega_x \approx \frac{\partial u_z}{\partial y}, \tag{4.16}$$

Substituting this expression for ω_x in equation 4.13, the integral over C_1 can be re-written as:

$$\int_{C_1} \big(-\omega_x u_z \big) \mathrm{d}y \approx \int_{C_1} u_z \Big(\frac{\partial u_z}{\partial y} \Big) \mathrm{d}y \tag{4.17}$$

The expression in equation 4.17 is significant. If one defines the vertices of our control volume based on the right-hand side of figure 4.8, the integral in equation 4.17 can now be evaluated in terms of u_z via a simple integration by parts. This process results in the following simple expression for the integral over C_1:

$$-\int_{C_1} u_z \Big(\frac{\partial u_z}{\partial y} \Big) \mathrm{d}y \approx -\frac{1}{2} u_{z,b}^2 \tag{4.18}$$

where $u_{z,b}$ represents the spanwise flow at point (b) in figure 4.8 (i.e., the spanwise flow at the intersection between C_1 and C_2). Equation 4.18 has thus re-written the complex line integral over C_1 as a simple function of the spanwise flow at a single point.

The line integral over control surface C_3 can be evaluated in a similar fashion.

That is, if one assumes $\omega_x \approx \partial u_z/\partial y$, the integral over C_3 from equation 4.13 assumes the following form:

$$\int_{C_3} u_z \Big(\frac{\partial u_z}{\partial y} \Big) \mathrm{d}y \approx -\frac{1}{2} u_{z,c}^2 \tag{4.19}$$

where $u_{z,c}$ is, again, the spanwise flow at point (c), or the value of the spanwise flow at the intersection between C_2 and C_3.

At this stage, let us return to the original line integral expression for the net spanwise convection/tilting term provided in equation 4.13. Collecting the results of equations 4.15, 4.18, and 4.19, this original expression for Sp can be approximated as follows:

$$\oint_C u_z \Big(\overrightarrow{\omega_{2D}} \cdot \hat{n} \Big) \mathrm{d}C = 2\Omega U_z L - \frac{1}{2} u_{z,b}^2 + \frac{1}{2} u_{z,c}^2 \tag{4.20}$$

In equation 4.20, one may note that points (b) and (c) both lie on control surface C_2; figure 4.8 illustrated that the spanwise flow along C_2 is nearly uniformly equal to the "background" spanwise flow (U_z). It follows that $u_{z,b}$ is equal to U_z, just as $u_{z,c}$ is equal to U_z, meaning the latter two terms in equation 4.20 roughly cancel one another out. The complete spanwise convection/tilting term can at last be reasonably approximated by:

$$Sp \approx 2\Omega U_z L \Big(1 - \frac{1}{2} \tan\alpha \Big), \tag{4.21}$$

where the $\big(1 - \frac{1}{2}\tan\alpha\big)$ term has been added to correct for the presence of non-zero

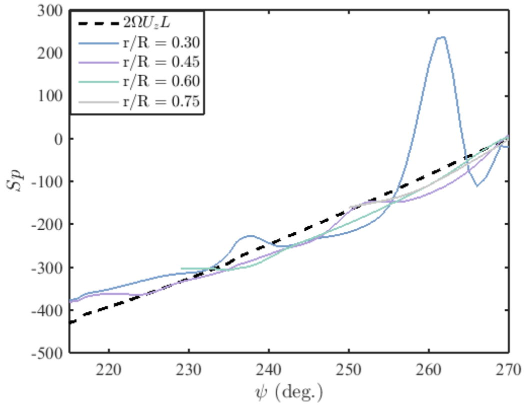

Figure 4.12: Evolution of the integrated spanwise convection/tilting term (solid lines) and an analytical approximation (dashed line) for multiple radial stations at the baseline forward flight condition ($\mu = 0.80$, $\theta_0 = 11°$)..

spanwise gradients along surfaces C_1 and C_3.

Figure 4.12 tests the validity of the approximation made in equation 4.21 with the actual spanwise convection/tilting term extracted from the numerical simulation. This figure demonstrates that equation 4.21 is a reasonable approximation of the spanwise convection/tilting term, at least during the vortex growth stage of the reverse flow region ($215° \leq \psi \leq 260°$). Note that this approximation is not expected to hold in cases where spanwise gradients, specifically the $\partial u_y/\partial z$ component of ω_x, are not small. In the context of the reverse flow region, such a scenario is most likely to occur following vortex "burst," or after the sharp-edge vortex has grown to such a size that it is no longer coherent. Figure 4.12, as an example, shows indication of vortex burst with the large spike in the $r/R = 0.30$ curve. Near $\psi = 260°$, the vortex at $r/R = 0.30$ becomes disorganized and spanwise gradients become significant, violating the main assumption behind equation 4.21. For points in the flow where the vortex remains coherent, however, equation 4.21 appears to be an adequate prediction of the magnitude of the spanwise convection/tilting term.

4.4.3 The Combined 3-D Effects Term

The current analysis has now provided an estimation of the net Coriolis transport (equation 4.12) and the net spanwise convection/tilting (equation 4.21) with a basis in the physics of the flow. Putting these two expressions together, the ratio of Coriolis transport to spanwise convection/tilting can at last be approximated as follows:

$$\frac{Co}{Sp} \approx \frac{2\Omega U_z L}{2\Omega U_z L\Big(1 - 1/2\tan(\alpha)\Big)} \approx \frac{2\Omega U_z L}{2\Omega U_z L} \approx 1 \tag{4.22}$$

The equation above embodies the main hypothesis of this section. That is, if spanwise gradients ($\partial u_y/\partial z$) are small compared to in-plane gradients, which is expected to be the case as long as the vortex remains coherent, then the Coriolis and spanwise convection/tilting terms will be roughly the same magnitude, and the net 3D effects on the sharp-edge vortex will be negligible in reverse flow. This hypothesis is expected to be most applicable to times where the sharp-edge vortex is within its growth stage, prior to the onset of "vortex burst," and does not explicitly depend on the advance ratio or current radial station.

As a way of further validating the hypothesis presented in equation 4.22, the vorticity transport analysis was repeated for the forward flight condition described in Chapter 3, which has a different rotation rate ($\Omega = 900RPM$), collective ($\theta_0 = 10°$), and advance ratio ($\mu = 0.60$) compared to the baseline case. Figure 4.13 shows the magnitude of various 3D mechanisms of vorticity transport for the baseline (top row) and secondary (bottom row) forward flight conditions. In each subplot, reduced time is plotted on the abscissa, and circulation contribution is plotted on the ordinate. Figure 4.13 plots only the Coriolis, the spanwise convection/tilting, and the combined 3D effects term, as the purpose of this figure is to observe if the combined 3D effects term (green line) is small over multiple flight conditions and radial stations. For both flight conditions, figure 4.13 reveals that the Coriolis and spanwise convection/tilting terms are consistently equal and opposite of one another. The more inboard stations ($r/R < 0.45$) do show brief spikes in the net 3D effects term near the end of the reverse flow region, indicating the onset of vortex burst, but on the whole, figure 4.13 suggests that the assumptions inherent to equation 4.22 are very reasonable for parameter space presented here. This adds weight to the notion that the net 3D effects term will always be small so long as the sharp-edge vortex remains coherent.

As a final comment, it is important to recognize that the ratio Co/Sp is different from the more well-known Rossy number (Ro). Numerous hovering wing studies can be found throughout the literature that cite a Rossby number of O(1) as an indicator of significant 3D effects on vorticity growth and vorticity transport. In those studies, the Rossby number physically represents the ratio of *in-plane* convection forces and Coriolis forces, and it is defined as $Ro = z/c$ (or the local aspect ratio). In the current work, the ratio Co/Sp physically represents the ratio of *spanwise* convection forces and Coriolis forces, a more appropriate metric considering the direction of spanwise gradients in reverse flow. To illustrate this idea, figure 4.13

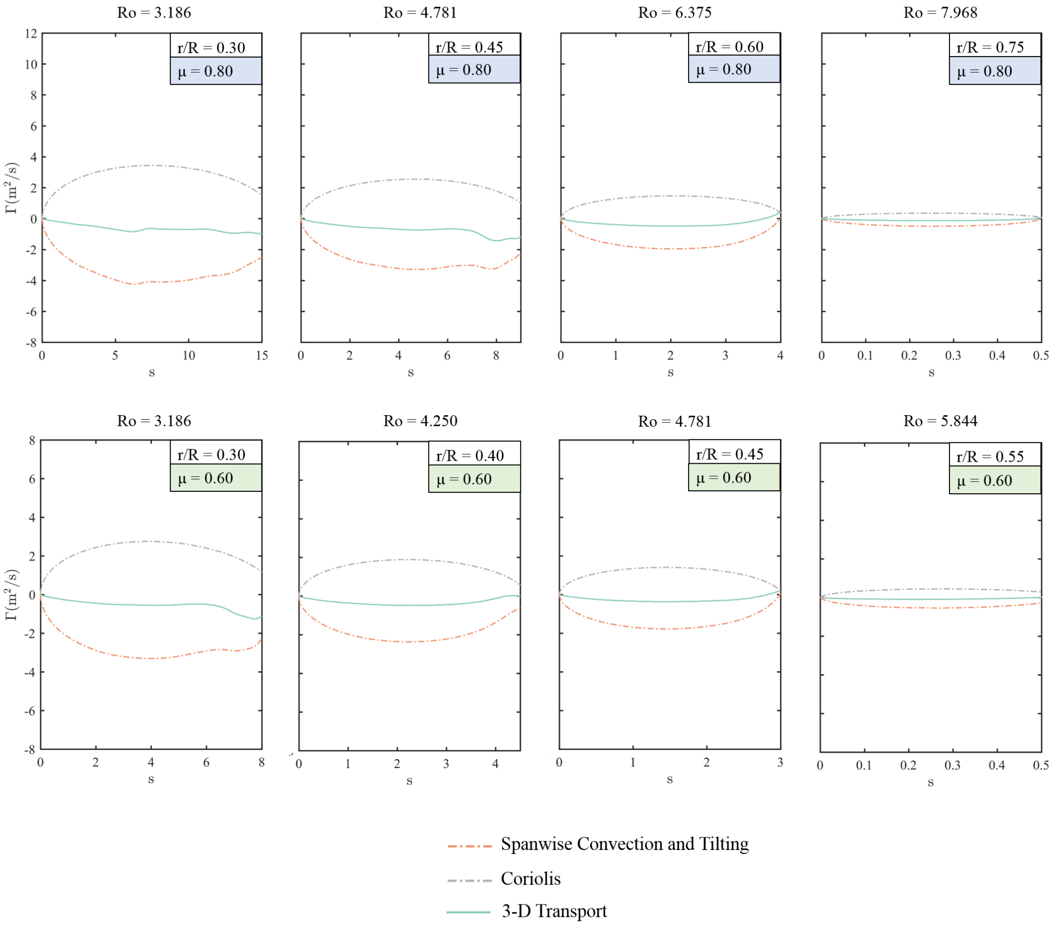

Figure 4.13: The magnitude of the Coriolis transport (grey), spanwise convection/tilting (orange), and net 3D effects term (green) in the reverse flow region for the baseline forward flight condition ($\mu = 0.80$, $\theta_0 = 11°$) and the secondary forward flight condition ($\mu = 0.60$, $\theta_0 = 10°$).

also includes the local Rossby at each spanwise station. Although the local Rossby number is of O(1) for the inboard portions of the blade, the combined 3D effects term remains low along the entire blade span, and there does not appear to be a significant dependence in its magnitude on radial station, as would be predicted by the changing Rossby number. This demonstrates the advantage of using Co/Sp over Ro when describing 3D effects in the reverse flow region of a rotor in forward flight.

4.5 Modeling the Sharp-Edge Vortex

Thus far, the previous sections found that as long as the sharp-edge vortex remains coherent, the impact of 3-D effects on vorticity transport is small, and the growth of the sharp-edge vortex is dominated by 2-D (or "in-plane") flow physics for an arbitrary forward flight condition. This is an impactful conclusion, because it suggests that a 2D predictive model of the reverse flow region may prove to be reasonably accurate without resorting to a computationally expensive 3D flowfield simulation. This section seeks to develop a low-order representation of the reverse flow region while including only the 2D mechanisms of the flow. Note that the goal of this section is not necessarily to present a model of the lowest order possible, but rather to identify an avenue for accurately predicting the strength of the sharp-edge vortex in reverse flow, and to reinforce our previous conclusions regarding the role of 3-D effects in vorticity transport.

Even without the inclusion of 3D effects, the problem of vortex formation at a sharp edge is a highly non-linear and difficult one to solve. The instantaneous rate at which a sharp-edge vortex grows is dependent on several properties of the flow, including (1) the wing kinematics, (2) the current strength of the sharp-edge vortex, (3) the current state of the trailing wake, and (4) the current state of the boundary layer, all of which of continuously interacting with one another. As discussed in section 1.3.2.3, various modeling efforts have been made to reduce these non-linear wake interactions to a simple set of equations, but the resulting models often require ad hoc empirical corrections to achieve a useful degree of accuracy [42, 105, 106]. An accurate, non-empirical prediction of vortex formation on a thin wing necessitates solving a set of non-linear differential equations, and thus requires a numerical time-stepping procedure to arrive at a reasonable solution.

Thankfully, numerous numerical models can be found in the literature that address the problem of vortex formation in a reasonably low-order fashion. The current work employs one such model, the discrete vortex method, to predict the strength of the sharp-edge vortex in the reverse flow region of the baseline forward flight condition. Discrete vortex models have long been employed to solve attached [64] and, more recently, separated flows [49, 50, 55, 107] over both 2-D and 3-D wing geometries. The concept behind a discrete vortex method is simple: one represents the rotational portions of a flowfield with collection of discrete, ideal vortices, and allows the vortices to convect based on the velocity induced by each of other point vortices in the flow. New vortices are then generated at each time step based on the boundary conditions of the flow. This formulation allows one to solve the problem of flow separation about a sharp edge with potential flow-based methods; the viscous generation of vorticity is modeled by the strategic placement

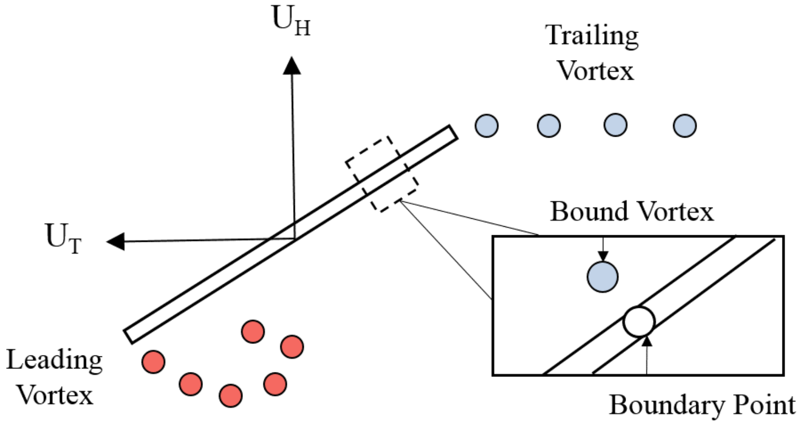

Figure 4.14: Overview of the discrete vortex method used to predict the strength of the sharp-edge vortex in reverse flow.

of vortex particles throughout the flow. The fidelity of vortex models ranges from the very basic [52, 71] to the very complex [70, 76], with methods available for incorporating viscous diffusion and turbulence (among other effects), but the current work's methodology most strongly resembles the low-order inviscid model detailed by Spalart [69].

Figure 4.14 shows the basic formulation of the discrete vortex model developed in the current work. For a given radial station of the rotor, the NACA 0012 blade section is simplified as an infinitely thin plate undergoing a simultaneous surging (U_T), heaving (U_H), and pitching (θ) maneuver, which is intended to mirror the local freestream, flap, and pitch oscillations, respectively, experienced by a rotor blade element in forward flight. The plate itself is discretized into a series of $N = 32$ boundary points, which includes the sharp leading and trailing edges of the plate. At each time step in the surge/pitch motion, one bound vortex is placed a small distance ($d_0 = 0.001c$) from each of the 32 boundary points, and the strength of each new bound vortex is determined by enforcing the flow tangency boundary condition. In equation form, the flow tangency condition can be written as:

$$\Psi_i = \Psi_{i-1} \tag{4.23}$$

where Ψ_i and Ψ_{i-1} are the values of the streamfunction at adjacent boundary points. Enforcing this condition along the plate surface results in a system of $N-1$ equations for N new bound vortices at each time step. The system is closed by evoking Kelvin's circulation theorem, or the notion that the strength of all vortices in the flow must collectively sum to zero:

$$\frac{\mathrm{D}\Gamma}{\mathrm{D}t} = 0 \tag{4.24}$$

Following the calculation of the bound vortex strength, two of these vortices, namely the vortices corresponding to the leading and trailing edges of the blade section, are released from the plate and denoted as "free" wake vortices. The entirety of the wake, which is comprised of the vortices released from the edges of the plate at the current and previous time steps, is then convected a short time Δt based on the velocity induced by all other vortices in the flow. The time step employed in this method was equal to $\Delta t = 0.015c/(\Omega r)$, which was sufficient for the strength of the sharp-edge vortex to converge [54, 108]. Note that the methodology described above accounts for each of the major sources of vorticity in the flow; the vortices shed from the leading edge model the sharp-edge vortex in reverse flow, the vortices

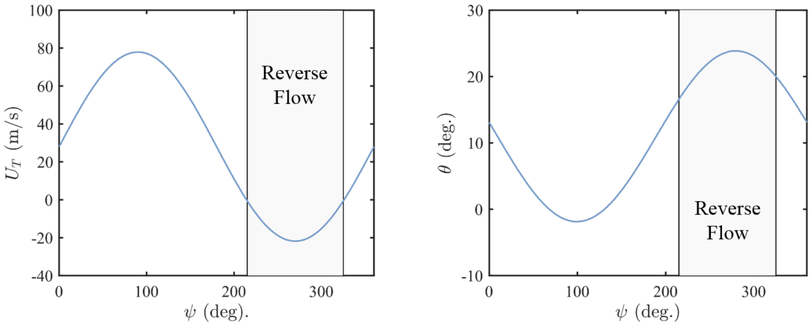

Figure 4.15: The equivalent surging (left) and pitching (right) kinematics for the 45% radial station at the baseline forward flight condition.

shed from the trailing edge model the trailing wake, and the bound vortices model the vorticity contained within the boundary layer.

Figure 4.15 shows the kinematics of a simultaneous surge (left) and pitch (right) maneuver that will serve as an illustration of the usefulness and limitations of the discrete vortex model. These kinematics were extracted from the time-history of the local freestream velocity (U_T) and pitch input (θ) for the 45% radial station at the rotor's baseline forward flight condition. As a way of avoiding any start-up transients early in reverse flow, the discrete vortex model was run for the entire "revolution" of the rotor blade section ($0° \leq \psi \leq 360°$), but vortices were only released from both edges of the plate during its passage through reverse flow (i.e., the flow is assumed unsteady but attached outside of the reverse flow region).

Figure 4.16 provides the results of running the discrete vortex model for the 45% radial station. The top plot of this figure shows a quantitative comparison of the positive circulation contained within our control volume for the high-fidelity CFD simulation (green line) and the low-order 2D vortex method (blue). The bottom two

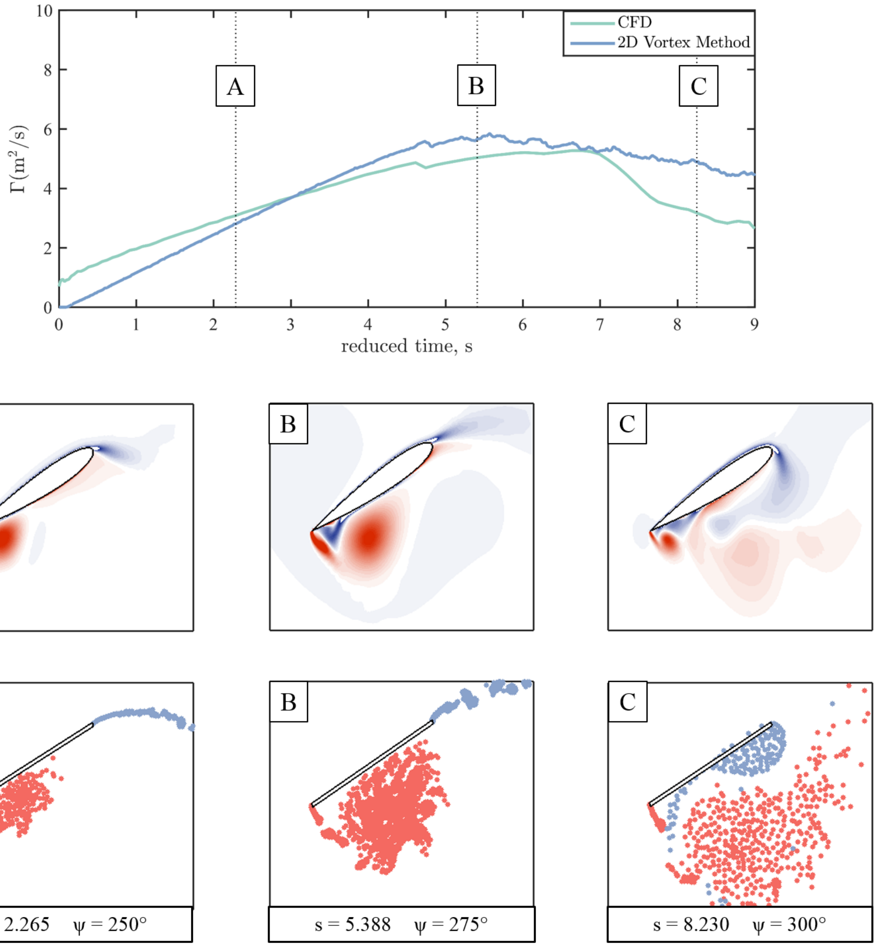

Figure 4.16: Comparison between the CFD simulation and the results of the 2-D vortex method for the 45% radial station. The top row compares the amount of positive circulation within the control volume throughout reverse flow, and the bottom two rows compare flowfield snapshots at various times.

rows present a side-by-side comparison of the state of the flow in the CFD (middle row) and the panel method (bottom row) at various points throughout the reverse flow region. Both qualitatively and quantitatively, figure 4.16 reveals reasonably good agreement between the low and high fidelity simulations, at least prior to the onset of vortex burst. Early in reverse flow ($s \leq 3.0$), for instance, the sharp-edge vortex undergoes consistent growth, and the vortex method/CFD exhibit good agreement (see point A in figure 4.16). This agreement continues through the vortex reaching its peak strength, where its size is roughly comparable to the airfoil chord (point B in figure 4.16). After reaching a critical size, the sharp-edge vortex bursts, and although the vortex method is still able to capture the basic structure of the flow, the two simulations begin to disagree (point C in figure 4.16). The 2-D vortex method thus appears to be a very reasonable approximation for the evolution of the sharp-edge vortex prior to the onset of vortex burst, at which point 3-D effects become a non-negligible factor in vorticity transport.

Figure 4.17, which shows a comparison between the CFD and 2D method for the 30%, 45%, and 60% radial stations, reveals very similar trends in the accuracy of the discrete vortex method. The $r/R = 0.30$ case again exhibits a reasonably similar growth stage ($s \leq 6.0$) and maximum strength compared to the CFD; the only significant discrepancy arrives near the exit of the reverse flow region ($s \geq 8.0$), when the flow structures become disorganized. Likewise, the $r/R = 0.60$ case shows very close agreement with the CFD throughout the entirety of the reverse flow region, as this case does not travel enough chords in reverse flow to reach the point of vortex burst.

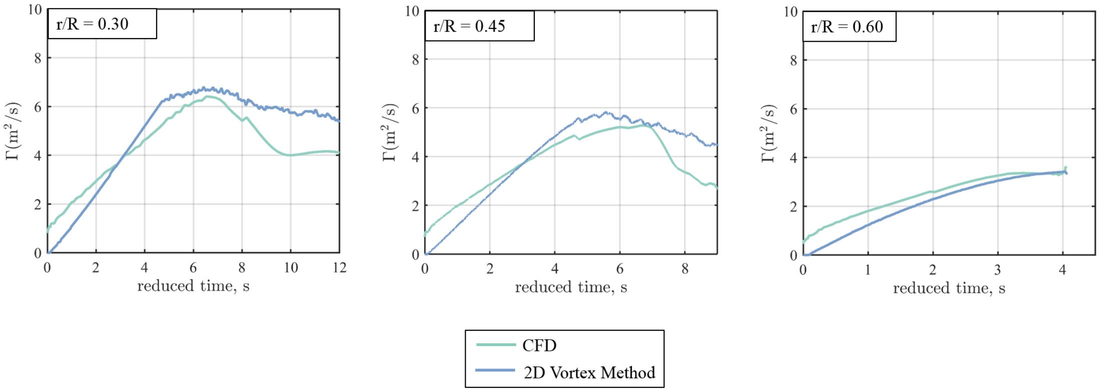

Figure 4.17: Comparison of the amount of positive circulation within the control volume in the CFD simulation (green) and the the 2-D vortex method (blue) for a sweep of radial stations ($0.30 \leq r/R \leq 0.60$).

At this point, let us briefly consider the implications of the results seen in figures 4.16 and 4.17. A simple vortex method, based only the 2-D kinematics and physics of the reverse flow region, was able to predict, with reasonable accuracy, the evolution of the sharp-edge vortex up until the onset of vortex burst. In addition to providing an avenue for modeling reverse flow, this observation reinforces the conclusions of the previous two sections. That is, during the growth stage of the sharp-edge vortex, the Coriolis and spanwise convection/tilting terms of the vorticity transport equation are roughly equal and opposite of one another, leaving only 2-D mechanisms to dominate the development of the sharp-edge vortex. The conclusions of this section thus imply that attempts to predict the strength of the sharp-edge vortex do not require full 3D simulations (assuming the vortex does not burst until near the exit of reverse flow), and that many recent attempts to further reduce the order of discrete vortex methods have a broad application in reverse flow aerodynamics.

4.6 Chapter Summary

In previous sections of this thesis, the reverse flow region of a rotor in forward flight was characterized by two large vortical structures: one vortex located at the sharp edge of the rotor blade, and a second vortex emanating from the blunt edge of the rotor blade. This chapter focused on understanding the physical mechanisms that govern the sharp-edge vortex, and leveraging that understanding into a low-order method for predicting its strength and behavior.

CFD simulations, with their high volumetric resolution, were first employed to quantify the 2-D and 3-D mechanisms of vorticity transport at play within the sharp-edge vortex. The ensuing analysis uncovered a critical observation regarding the physics of the sharp-edge vortex: in the baseline forward flight condition, the transport of vorticity due to 3D effects is negligible for a significant portion of the reverse flow region. This observation was attributed to the direction of spanwise gradients on the rotor. In the reverse flow region, transport due to Coriolis forces and transport due to spanwise convection are oriented opposite of one another; if these effects are roughly the same magnitude, their combined effect is small compared to 2D mechanisms of vorticity transport. An analytical investigation revealed that this cancellation of Coriolis and spanwise convection forces can be expected for any forward flight condition or advance ratio, as long as the vortex has not undergone “vortex burst,” wherein its structure becomes disorganized.

Next, a low-order discrete vortex method was proposed for modeling the sharp-edge vortex. The CFD simulations had suggested that the growth of the sharp-edge vortex could be accurately captured based only on the 2-D physics of the flow, and thus the discrete vortex model considered only the 2-D (or "in plane") freestream velocity and pitching kinematics of a given radial station. Consistent with the previously observed role of 3-D effects, the low-order vortex method was able to predict the strength of the sharp-edge vortex quite well, only deviating from the CFD solution after the vortex had "burst" near the exit of the reverse flow region. Such agreement was also observed at a number of other radial stations for the baseline forward flight condition of the rotor.

The model proposed in this chapter represents a strong step forward in predicting the flow on a high advance ratio rotor. The discrete vortex method described here is capable of capturing the sharp-edge vortex during its growth stage, where its impact on the aerodynamic forces is expected to be high, and takes advantage of the negligible impact of 3-D effects, a feature unique to the reverse flow region. Although it becomes somewhat inaccurate after the onset of "vortex burst," the model still demonstrates that a discrete vortex method, even a simplified 2-D version, is well-suited to predicting the coherent flow structures that result from separation on a high advance ratio rotor.

Chapter 5: Analysis of the Blunt-Edge Vortex

This chapter is aimed at understanding and modeling the second vortical structure observed in the reverse flow region: the vortex that forms from the shear layer emanating from the blunt edge of the blade. Because this "blunt-edge" vortex appears to form prior to the blade's transition into reverse flow, the current chapter takes a somewhat different approach compared to our study of the sharp-edge vortex. In the previous chapter, the formation of the sharp-edge vortex was assumed to coincide with the blade's entrance into reverse flow, and the analysis was concerned with exploring where the vorticity generated at the sharp edge was transported following its formation. In the current chapter, the blunt-edge vortex cannot be assumed to form at a specific point in the blade's revolution, as the rounded edge of an airfoil is capable of supporting a finite pressure gradient. In turn, this chapter is concerned with where the blunt-edge vortex begins to form and how the various unsteady features of the rotor affects its formation process.

To begin, it must be mentioned that the behavior of the blunt edge vortex qualitatively resembles that of a classical dynamic stall vortex in that both flow structures result from boundary layer separation about a rounded edge. One may then assume that the wealth of experimental and numerical data in the literature regarding classical dynamic stall, which nearly universally approaches the problem as a pitching wing in a constant freestream, is applicable to the blunt-edge vortex observed in our rotor experiments. While it is true that a rotor blade undergoes a large pitching oscillation at high advance ratio, one must also keep in mind that the aerodynamic environment of a rotor at high advance ratio is more complex than what is captured by conventional dynamic stall experiments. Figure 5.1, for example, shows the local freestream velocity (U_T), pitch angle (θ), and "freestream" spanwise flow (U_Z) experienced by three blade elements at the baseline forward flight condition of our rotor system ($\mu = 0.80$, $\theta_0 = 11°$). Dynamic stall experiments have been performed that capture a similar pitch oscillation to what is seen in figure 5.1, but very few address the variation in local freestream or spanwise flow. The local freestream, in particular, undergoes a very large oscillation at high advance ratio, the magnitude of which can be defined according to:

$$U(t) = U_0\Big(1 + \lambda \sin(\psi)\Big), \tag{5.1}$$

where U_0 is a mean velocity (defined by $U_0 = \Omega r$) and λ is a non-dimensional surge amplitude (defined by $\lambda = (r/R)/\mu$). For the inboard portions of our rotor system, the amplitude of the freestream oscillation can become quite large, up to $\lambda = 2.67$ for $r/R = 0.30$, and this freestream unsteadiness undoubtedly impacts the timing of blunt-edge vortex formation.

This chapter details a set of 2-D experiments designed to observe the formation of a blunt-edge vortex when both the pitch angle and freestream undergo large

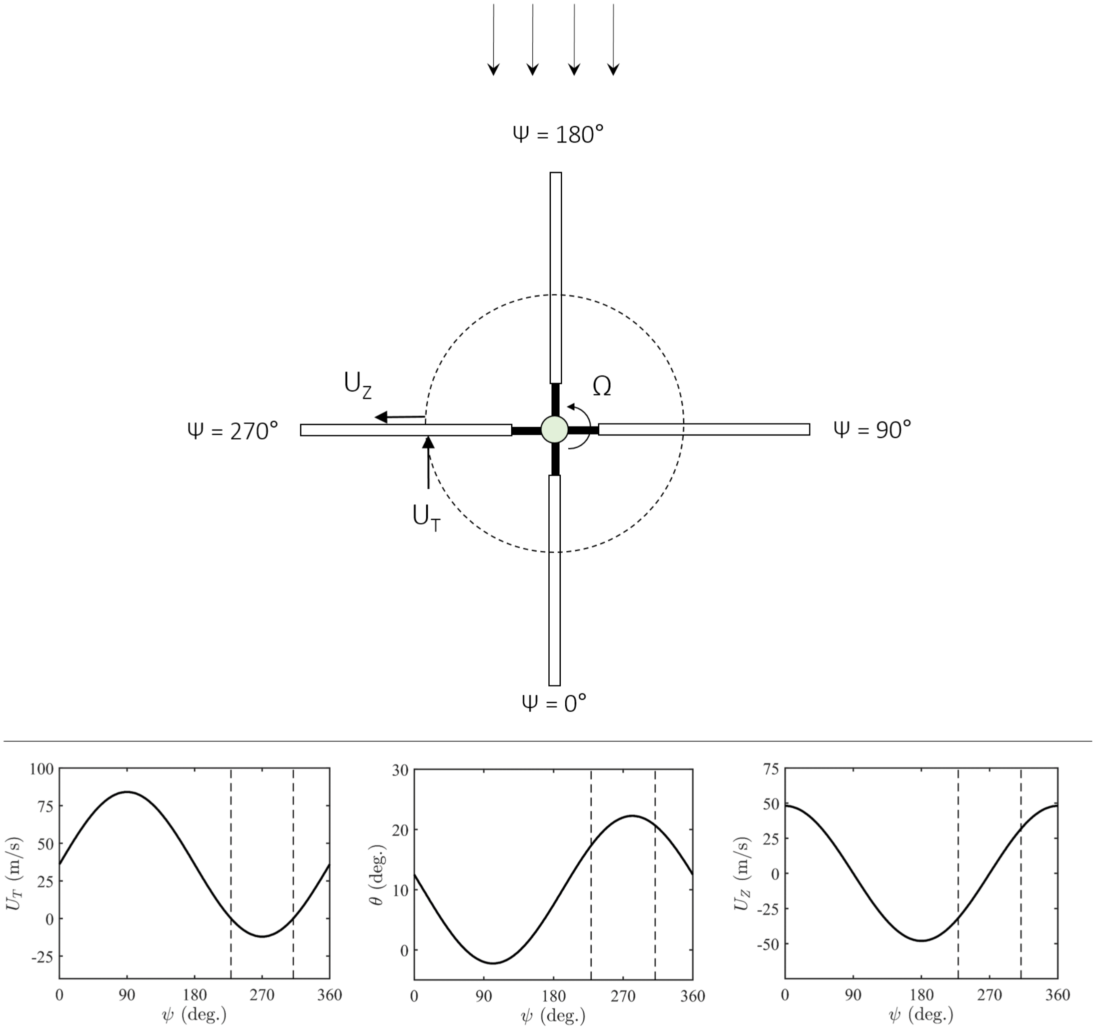

Figure 5.1: Illustration of the variation in local freestream (U_T), pitch angle (θ), and spanwise flow (U_Z) for the 45% radial station of our rotor system at the baseline forward flight condition ($\mu = 0.80$, $\theta_0 = 11°$).

variations in time. The 2-D nature of these experiments allows us to isolate the effect of an unsteady freestream velocity, a feature of the rotor flowfield that has been seldom explored in a fundamental context, and resolve a greater portion of the blade oscillation than would be possible in a 3-D rotor experiment. The 2-D experiments found in this chapter were performed in a water-filled tow tank on a simultaneously surging and pitching NACA 0012 airfoil (see chapter 2 for details of the test article and facilities). The following sections provide a more detailed discussion of the parameter space explored before presenting the experimental results and analysis.

5.1 Kinematics

The kinematics of these experiments were chosen as a way of recreating the conditions of blunt-edge vortex formation on our rotor system at its baseline configuration. The primary variables of interest were the non-dimensional surge amplitude (λ) and the surge reduced frequency (k), which collectively control the properties of the unsteady freesteam oscillation. In terms of rotor parameters, the surge amplitude has already been defined as $\lambda = (r/R)/\mu$, where μ is the advance ratio of the rotor and r/R is the radial station. In the same way, the 2D reduced frequency can be related to the properties of the rotor through:

$$k = \frac{\Omega c}{2U_0} = \frac{1}{2}\Big(\frac{1}{AR}\Big)\Big(\frac{1}{r/R}\Big), \tag{5.2}$$

where AR is the aspect ratio of the blade, equal to $AR = 10.625$ for the rotor considered here. In the current 2-D experiments, the surge amplitude was varied

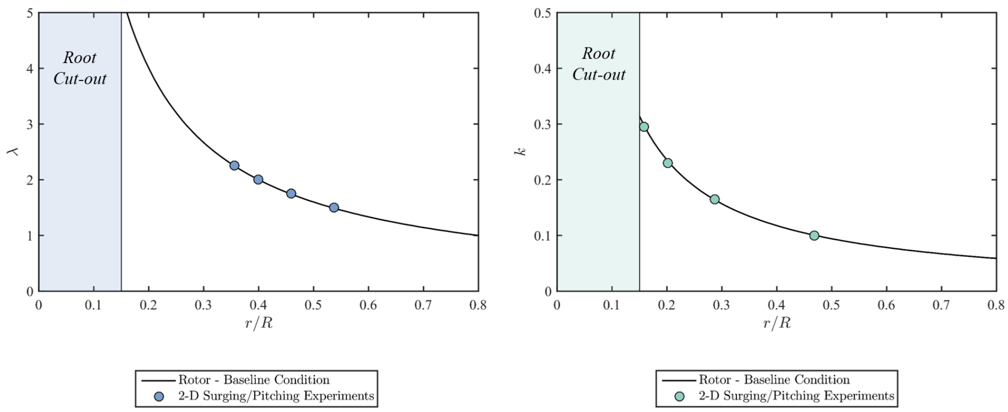

(a) The surge amplitude. (b) The reduced frequency.

Figure 5.2: The surge amplitudes (λ) and reduced frequencies (k) from the 2-D surging/pitching wing experiments compared to equivalent values found on the rotor system at the baseline forward flight condition ($\mu = 0.80$, $\theta_0 = 11°$).

over the range $1.50 \leq \lambda \leq 2.25$, and the reduced frequency was varied over the range $0.100 \leq k \leq 0.300$. These variations are intended to illuminate how a change in the unsteady freestream impacts the features of the flow that lead to separation at the rounded edge of the wing.

The exact values of λ and k in our 2D experiments each correspond to a radial station on our rotor system at its baseline forward flight condition. Figure 5.2 shows a comparison of the non-dimensional amplitude and frequency found along the span of the rotor blade and the test points evaluated in the 2-D surging/pitching wing experiments. Illustrated in figure 5.2, the portion of the λ-k parameter space explored here has a clear application to a rotor in forward flight, covering a significant number of inboard radial stations for the baseline rotor condition. Note that although the non-dimensional amplitude and frequency are representative of a real rotor, the mean Reynolds number of the current experiments is lower than what is typical of a spinning rotor in forward flight (see table 2.2 for an idea of full-scale Reynolds numbers). In all experiments presented in this chapter, the mean Reynolds number was held constant at $Re = U_0 c/\nu = 2.0 \times 10^4$. Its low order of magnitude is a limitation of the test facility.

A dynamic pitch oscillation was also introduced during each run of the experiment to coincide with the surging motion of the wing. The pitch oscillation takes the same basic form as the surge, or:

$$\theta(t) = \theta_0 + \theta_1 \Big(\sin(\psi + \phi) \Big) \tag{5.3}$$

where θ_0 is the mean pitch angle, θ_1 is the pitch amplitude, and ϕ is a phase-shift relative to the freestream oscillation. The pitching kinematics were held constant at a certain set of conditions ($\theta_0 = 15^\circ$, $\theta_1 = 8^\circ$, and $\phi = \pi$) for all experimental cases considered here as a way of isolating the less-studied effects of an unsteady freestream velocity. Very similar values of the pitching parameters were explored in a number of classical (i.e., pitching only) dynamic stall experiments [36, 37, 38], and also are a reasonable approximation of the pitching parameters of the rotor's baseline case ($\theta_0 = 11^\circ$, $\theta_1 \approx 12^\circ$, $\phi \approx \pi$).

Figure 5.3 collects the kinematics of each 2-D surging/pitching test point into a concise series of subplots. The complete test matrix consists of a sweep of four surge amplitudes at constant reduced frequency (figure 5.3(a)) and a sweep of four reduced frequencies at constant surge amplitude (figure 5.3(b)). The pitch kinematics (figure 5.3(c)) and mean Reynolds number ($Re_0 = 2 \times 10^4$) are held constant for

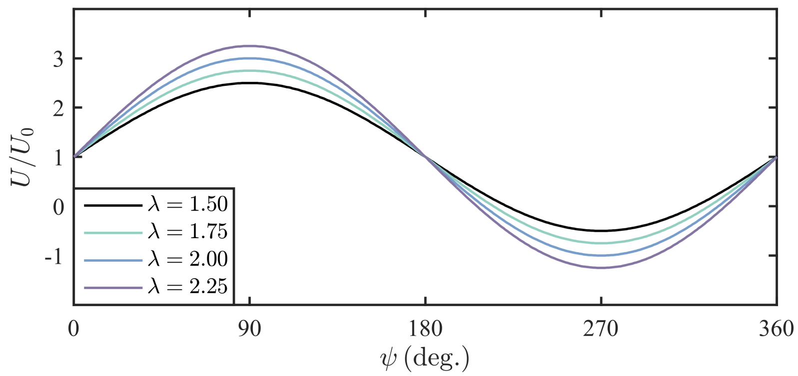

(a) Surge amplitude sweeps at constant reduced frequency ($k = 0.165$).

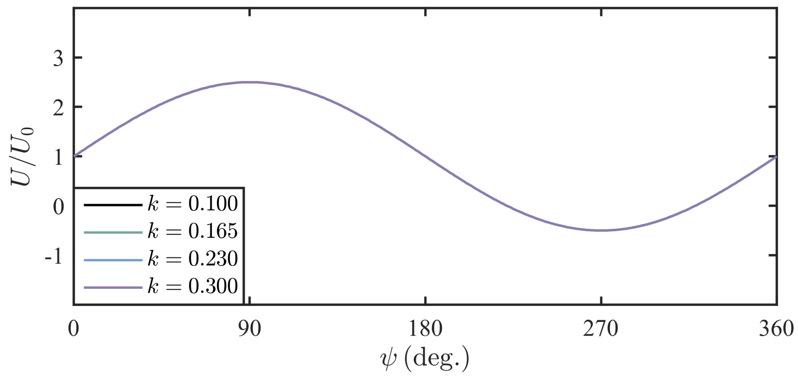

(b) The reduced frequency sweeps at constant surge amplitude ($\lambda = 1.75$).

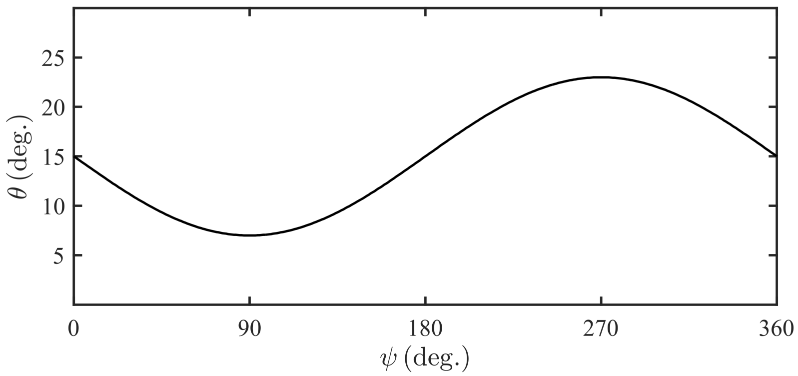

(c) The pitch angle (constant for all cases).

Figure 5.3: The complete kinematics for the 2-D surging and pitching wing experiments, consisting of a sweep in surge amplitude and reduced frequency.

each test point. Note that all four reduced frequency cases undergo the same $U(t)$ variation in non-dimensional, azimuthal time ($\psi = \Omega t$) but were in fact performed at increasing values of dimensional frequency (Ω). The higher reduced frequency cases thus have a higher value of dimensional acceleration, a fact that is not necessarily evident in figure 5.3(b).

5.2 Basic Flow Morphology

Figure 5.4 presents a series of flowfield snapshots that illustrate the basic stages of vortex formation for the wing at a baseline surge ($\lambda = 1.75$, $k = 0.165$) and pitch ($\theta_0 = 15°$, $\theta_1 = 8°$, $\phi = \pi$) condition. Each snapshot is overlain with contours of counter-clockwise vorticity (red) and clockwise vorticity (blue). The flowfields in figure 5.4 were collected over the range $160° < \psi < 270°$, which captures a significant portion of the wing's deceleration into reverse flow, or the time at which a vortex is presumed to roll up about the blunt-edge of the wing. Note that each snapshot only includes measurements on the upper surface of the wing, where the blunt-edge vortex is expected to form, while the underside of the wing is masked due to a laser shadow.

Qualitatively, the vortex in figure 5.4 behaves in a similar fashion to the blunt-edge vortex observed in the rotor experiments of chapter 3. In addition, one can identify several unique stages in the formation process of this vortex by considering each flow snapshot in chronological order. At flow snapshot (1), for instance, the instantaneous velocity and pitch angle are at their mean values, and no appreciable

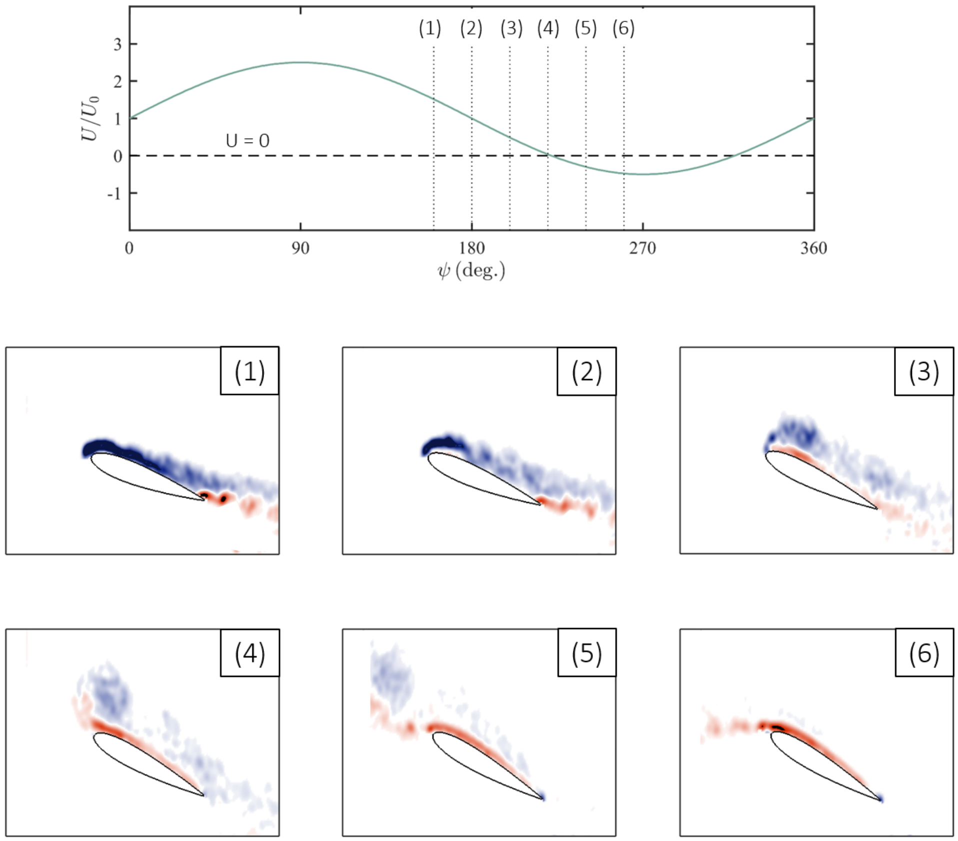

Figure 5.4: Evolution of the blunt-edge vortex on the surging and pitching wing at its baseline kinematics ($\lambda = 1.75$, $k = 0.165$, $\theta_0 = 15°$, $\theta_1 = 8°$)

flow separation is observed on the surface of the surface of the wing. The height of the boundary layer appears somewhat large, but the vorticity in this region still remains of the same sign and roughly follows the surface of the blade. This state of the flow, wherein the boundary layer is thick but attached, continues through flowfield snapshot (2). At snapshot (3), a shear layer is visible at the blunt-edge of the wing, and a region of counter-clockwise vorticity can be seen beneath the shear layer, indicating that the sign of the local shear stress has reversed. The shear layer continues to feed the vortex until shortly after the wing passes into reverse flow, an event represented by snapshot (4), at which point the vortex is "pinched off" from the surface of the wing. In snapshots (4) and (5), the wing has transitioned fully into the reverse flow portion of its surge profile, and the blunt-edge vortex is simply convecting in the direction of the freestream, just as it was in the rotor experiments of chapter 3.

5.3 Flowfield Statistics

The flow morphology outlined in figure 5.4 includes a number of events that differentiate it from the more conventional dynamic stall process. For one, the transition to reverse flow appears to act as a "cut-off" for the growth of the blunt-edge vortex; in a conventional dynamic stall, the primary vortex is not shed until it reaches some critical size. Likewise, the boundary layer in figure 5.4 separates suddenly near the leading edge of the wing; in conventional dynamic stall, flow separation generally begins at the trailing edge and gradually works its way toward the leading edge.

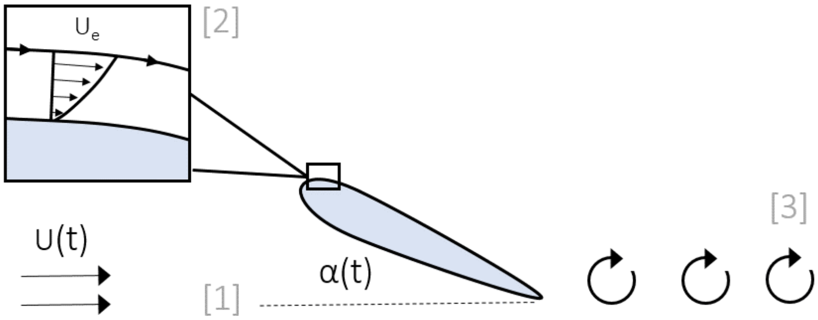

Figure 5.5: Illustration of the various features of a surging/pitching wing that impact the likelihood of flow separation, including [1] the instantaneous wing kinematics, [2] unsteady effects in the boundary layer, and [3] the state of the trailing wake.

This latter point, or the presence of a leading edge separation, is of particular interest to the present analysis. The changing freestream has an important impact on the timing of separation at the leading edge, and such freestream unsteadiness is rarely captured by predictive models of dynamic stall. This chapter is interested in exploring these unsteady effects with our experimental measurements, but first, it is important to understand what specific features of the flowfield are expected to be impacted by the presence of an unsteady freestream.

Figure 5.5 presents a simple illustration of the NACA 0012 wing at an arbitrary point in its deceleration, prior to the entrance of the reverse flow region. The state of the boundary layer at this point, and thus the likelihood of flow separation at the leading edge, is a function of three features of the surrounding flowfield, each of which is labeled in figure 5.5. The first is the instantaneous velocity ($U(t)$) and pitch angle ($\theta(t)$). These wing kinematics determine the “quasi-steady” features of the boundary layer, including the local momentum and pressure gradient, and represent the minimum of what must be included in a flow separation model. The second flow feature is the presence of unsteadiness in the boundary layer itself. During a wing's deceleration, fluid particles experience a different local time rate of change compared to the surrounding flow, and this local time-deceleration value has an important influence on the local shear stress along the wing surface [75, 109, 110]. The final flow feature is the presence of unsteadiness in the external flow, which prior to separation, is concentrated in the trailing wake. When a wing decelerates, the magnitude of its bound circulation inevitably decreases over time, and an equivalent magnitude of circulation must be shed into the trailing wake to uphold Kelvin's theorem. The orientation of this trailing circulation is such that the likelihood of separation increases during a freestream deceleration.

With these features in mind, a complete picture of unsteady effects on our surging and pitching wing will thus require an understanding of the state of the trailing wake, the state of the boundary layer, and ultimately, how these features combine to change the timing of vortex formation. Each of these properties can be estimated from flowfield measurements via a series of simple statistics and calculations. We will begin by considering a representation for the state of the trailing wake. At a given time in the surging/pitching maneuver, the velocity induced on the leading edge by the wake is proportional to the amount and distribution of circulation within the wake, the most impactful of which is found in the "near wake" immediately behind the trailing edge of the wing. Figure 5.6 shows a simple control volume, of width $c/4$, employed in the present work to compute the "strength" of the near wake at a given time. A value for the strength of the near wake is calculated

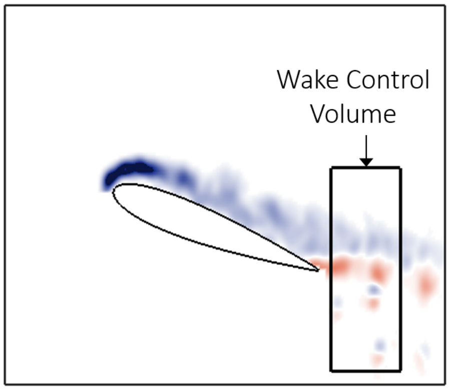

Figure 5.6: Sketch of the control volume used to calculate the total clockwise (blue) circulation in the near wake throughout the deceleration portion of the surging/pitching maneuver.

by performing a numerical area integral of all clockwise (blue) vorticity contained within this control volume. If the calculation is repeated for each flowfield snapshot, one can quantitatively observe how the state of the wake evolves throughout the course of the surging/pitching oscillation.

We now consider our next flow property: the state of the boundary layer at a given time in the surging/pitching motion. While the literature is ripe with numerous statistics regarding the state of a boundary layer near the surface of an airfoil, including the well-known displacement and momentum thicknesses, the current work employs a simple calculation of the dimensional boundary layer height. As an illustration of this calculation, figure 5.7 shows a snapshot of the baseline surging and pitching case, now featuring a line drawn normal to the wing surface at a distance $c/5$ from the leading edge. The velocity perpendicular to this line can be estimated based on the x and y components of the flowfield measurement, giving us

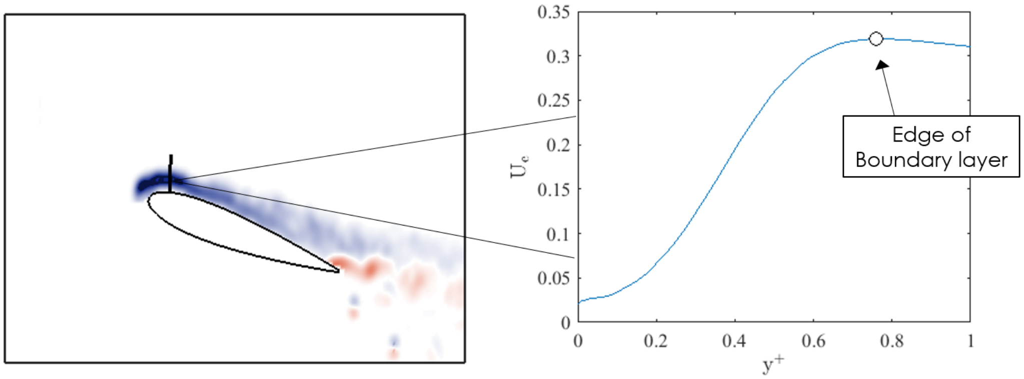

Figure 5.7: Calculation of the boundary layer height for a position $c/5$ from the leading edge at a given time in the baseline surge and pitch maneuver.

an estimation of the surface-tangent component of velocity along the line (except for a region near the surface that is obstructed by laser reflections). In figure 5.7, the surface-tangent velocity is seen to first increase as one moves away from the wing, a consequence of the no-slip condition at the surface, before ultimately decreasing as one moves further away, a consequence of the far-field boundary condition. The "edge" of the boundary layer is thus identified as a local maximum in the surface tangent velocity. Note that the current work performs this calculation at 10 different points over the range $c/5 \leq x/c \leq 2c/5$, then averages the resulting heights at each time step to arrive at a smooth evolution of the leading edge boundary layer height in time.

At this point, we have outlined methods for measuring (1) the strength of the near wake and (2) the height of the boundary layer. One must keep in mind, however, that the ultimate goal of this chapter is to understand and predict how these features combine to influence the timing and onset of vortex formation. The current analysis would thus benefit from a quantitative measurement of when vortex formation begins that can be compared to the trends in wake strength and boundary layer height. Such a measurement is seldom found in the literature, as the initial accumulation of vorticity in the boundary layer is difficult to observe, and so the current work has developed a novel method for estimating the initial stages of vortex formation that makes use of a number of basic flowfield statistics. To illustrate this method, consider the following relation, which links the final strength of the blunt-edge vortex to a time history of its growth rate:

$$\Gamma_f = \int_{t_i}^{t_f} \left(\frac{\mathrm{d}\Gamma}{\mathrm{d}t}\right) \mathrm{d}t. \tag{5.4}$$

In equation 5.4, Γ_f represents the final strength of the blunt-edge vortex after being shed from the wing, $\mathrm{d}\Gamma/\mathrm{d}t$ represents the growth rate of the vortex; t_i represents the time at which vortex growth begins; and t_f represents the time at which vortex growth ends. Equation 5.4 is useful in the sense that it can be manipulated to isolate the time at which vortex formation begins, or t_i, and the remaining terms of the equation can be approximated by a series of simple flowfield calculations.

The final strength of the blunt-edge vortex, for instance, can be captured by acknowledging that the vortex convects with the local freestream velocity after shedding from the wing. The right-hand side of figure 5.8 shows a vertical flux plane that lies directly in the path of the blunt-edge vortex. If one were to compute the flux of clockwise (blue) vorticity through this plane, the convection of the blunt-edge vortex would appear as a "spike" in the vorticity flux measurement. The current

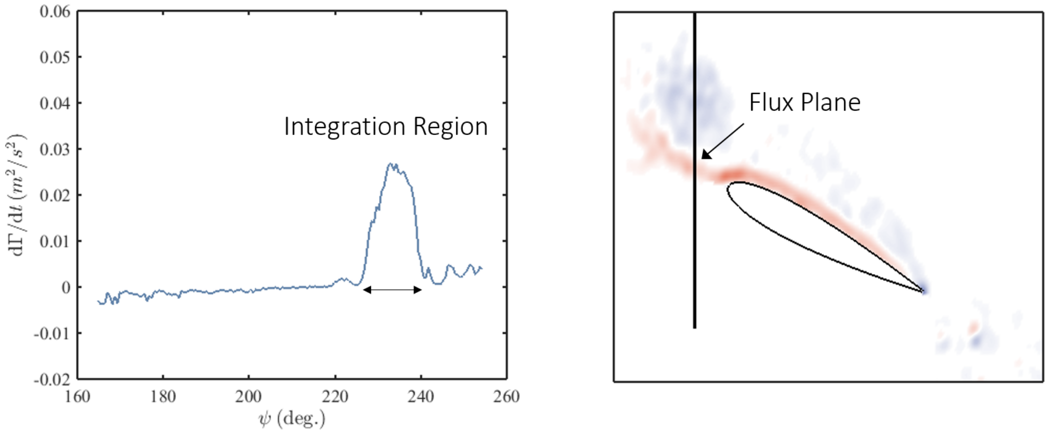

Figure 5.8: Calculation of the final vortex strength following its shedding from the surface of the wing.

work uses a temporal integration of this spike, the bounds of which are denoted as 10% of the maximum flux value, as an estimate of the final vortex strength. This allows the variable Γ_f in equation 5.4 to be represented by a numerical value at each time in the surge/pitch maneuver.

The time history of the vortex growth rate ($d\Gamma/dt$) can be computed in a similar fashion. Figure 5.4 illustrated that the blunt-edge vortex is fed via a shear layer during its growth state, and the shear layer emanates from the separated flow near the rounded leading edge of the wing. The growth rate of the blunt-edge vortex can thus be approximated by calculated the instantaneous flux of vorticity in the shear layer at each time step. The right-hand side of figure 5.9 illustrates a simple control volume used to accomplish this task. The growth rate of the blunt-edge vortex at a given time is represented by the flux of clockwise (blue) vorticity out of this control volume, which is assumed to be equivalent to the flux of vorticity into

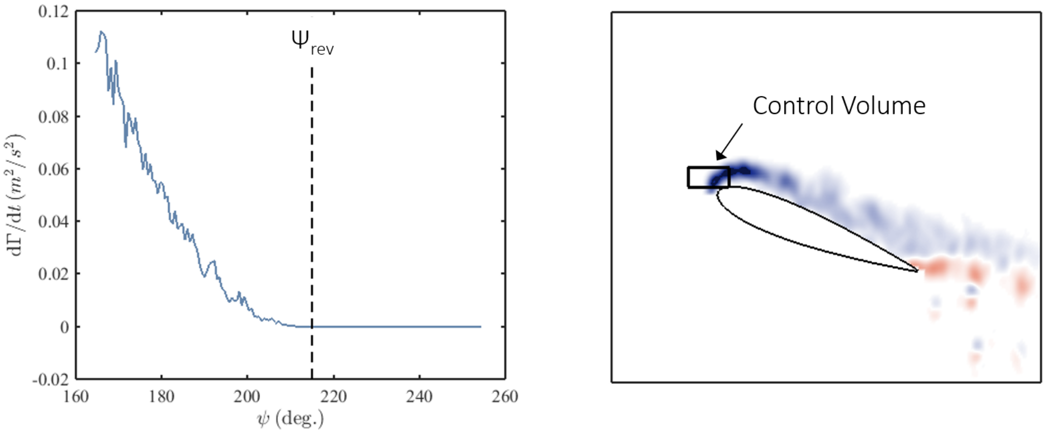

Figure 5.9: Calculation of the vortex growth rate by way of the flux of vorticity through the leading-edge shear layer.

the vortex.

The only remaining terms without a numerical representation in equation 5.4 are the time at which vortex growth begins (t_i) and the time at which vortex growth ends (t_f). Keeping with the flow morphology of figure 5.4, the time at which vortex formation ends (t_f) can be assumed to coincide with the timing of freestream reversal (t_{rev}), as the reverse flow region was observed to "cut off" the growth of the sharp-edge vortex. If t_f is replaced by the known quantity t_{rev} in equation 5.4, t_i becomes the sole unknown, and it can be backed out of equation 5.4 for each variation of the surging kinematics. This procedure, wherein t_i is reverse engineered based on a computation of the final vortex strength (Γ_{rev}) and shear layer flux ($d\Gamma/dt$), is employed in the following sections to determine the timing of vortex formation.

As a short summary, this section has detailed a methodology for measuring the strength of the wake at a given time, the height of the boundary layer, and finally the time at which vortex formation begins. The following sections will address trends in the timing of vortex formation (ψ_{vort}) across a wide parameter space of surge amplitudes (λ) and reduced frequencies (k). Using the information obtained from the boundary layer and wake measurements, we will also identify what features of the flow must be captured in order to predict the onset of vortex formation.

5.4 Variation in Surge Amplitude

The purpose of this section is to understand the effect of surge amplitude on the timing of vortex formation. To obtain the results presented here, experiments were run over a sweep of four surge amplitudes ($1.50 \leq \lambda \leq 2.25$) at constant reduced frequency ($k = 0.165$), pitch kinematics ($\theta_0 = 15°$, $\theta_1 = 8°$, $\phi = \pi$), and mean Reynolds number ($Re = 2.0 \times 10^4$). The various flowfield statistics, including the timing of vortex formation, the height of the boundary layer, and the strength of the near wake, were computed throughout the surge/pitch motion for each individual test point.

Figure 5.10 shows how the timing of vortex formation (ψ_{vor}) is affected by a change in the non-dimensional surge amplitude (λ). In this figure, the onset of vortex formation is seen to uniformly shift toward earlier times in the surge/pitch oscillation as the surge amplitude increases to higher values. This observation sounds straightforward, in that a more aggressive surge maneuver should intuitively result in an earlier flow separation, but it remains unclear what physical feature of the flow is causing the earlier onset of separation. It is thus important that we explain the

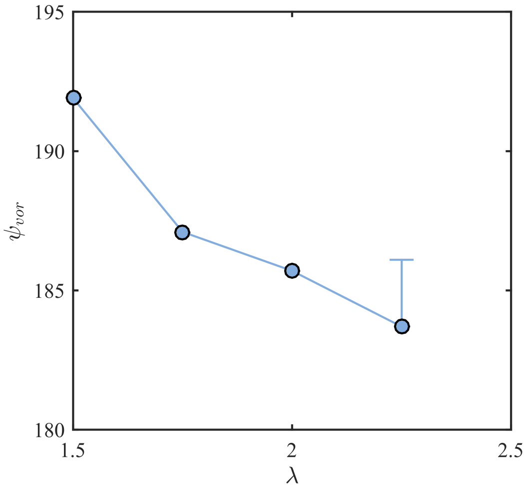

Figure 5.10: The effect of surge amplitude (λ) on the timing of vortex formation (ψ_{vor}) for constant pitching kinematics and reduced frequency.

trends in figure 5.10 using the behavior of the boundary layer and the near wake, such that we can understand what flow features are most important in the context of low-order modeling.

To begin, figure 5.11 shows the variation in the height of the boundary layer (δ) for each test point in the period immediately before the onset of vortex formation ($170° < \psi < 185°$). The lines in figure 5.11 appear to all behave in a very similar fashion, with no clear trend in the boundary layer height for different values of the surge amplitude (λ). This behavior is somewhat expected for the "quasi-steady" features of the boundary layer, as the instantaneous freestream velocity does not have a large dependence on λ over the range $170° < \psi < 185°$, but is not necessarily expected for the unsteady features of the boundary layer, as each surge amplitude case corresponds to a different value of freestream acceleration. Figure 5.11 would appear to suggest that the unsteady properties of the boundary layer are relatively

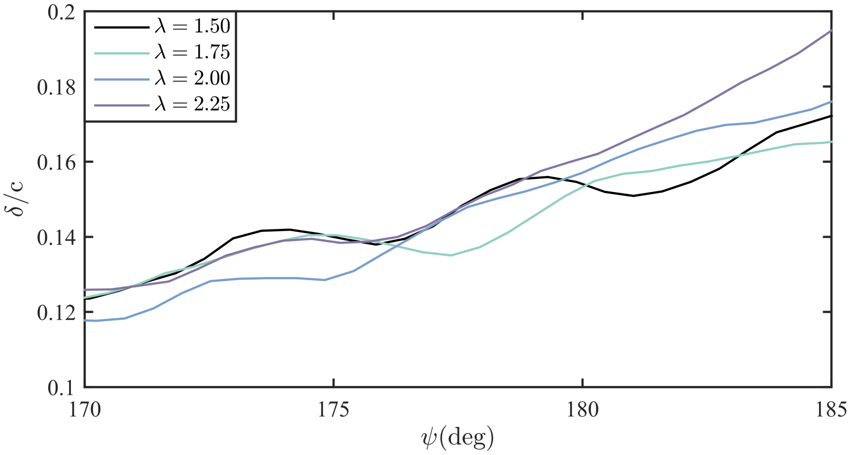

Figure 5.11: The effect of surge amplitude (λ) on the height of the boundary layer (δ) in the period of the oscillation ($170 < \psi < 185$) immediately preceding flow separation.

invariant leading up to the onset of flow separation.

The insignificance of unsteady effects in the boundary layer can be explained by briefly considering the various physical mechanisms that influence the instantaneous boundary layer height. For illustrative purposes, the non-dimensional form of the unsteady, laminar boundary layer equations are introduced in two dimensions as follows:

$$\left(\frac{L}{TU}\right)\frac{\partial u^*}{\partial t^*} + u^*\frac{\partial u^*}{\partial x^*} + v^*\frac{\partial u^*}{\partial y^*} = -\frac{\partial p^*}{\partial x^*} + \frac{\partial^2 u^*}{\partial (y^*)^2}, \tag{5.5}$$

where T is a characteristic time scale, U is a characteristic velocity, and the terms marked with a "*" are all of O(1). If one were to set T equal to the inverse of the oscillation frequency ($T = 1/\Omega$), and U equal to the instantaneous freestream velocity ($U = U(t)$), unsteady effects in the boundary layer can be seen to scale with an "instantaneous" form of the reduced frequency, or $k_{inst} = \Omega c/U(t)$. Figure 5.12

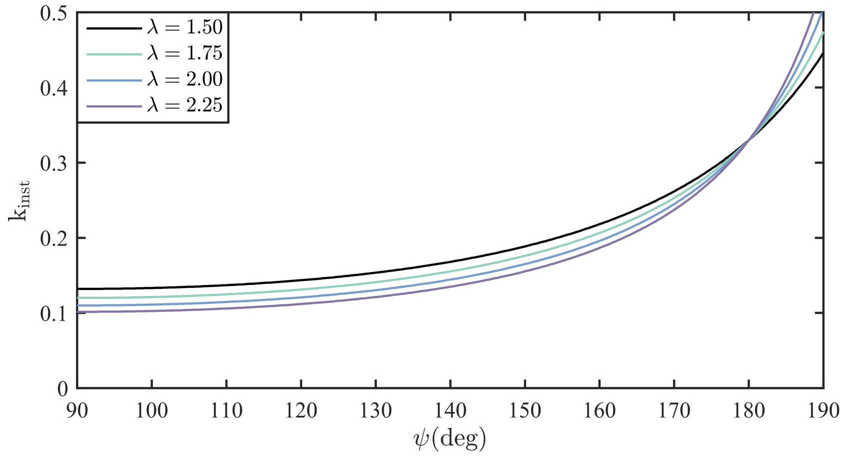

Figure 5.12: The predicted magnitude of unsteady boundary layer effects (k_{inst}) throughout the deceleration portion of the surge/pitch maneuver for various surge amplitudes.

plots a time history of k_{inst} as it evolves over the surge/pitch oscillation, and offers numerous insights into the expected order of magnitude of unsteady effects in the boundary layer. Specifically, the instantaneous reduced frequency is an order of magnitude lower than the other terms in equation 5.5 over the range $170^\circ < \psi < 185^\circ$, and its magnitude decreases with increasing values of the surge amplitude λ. Figure 5.12 thus agrees with the assertion that unsteady effects in the boundary layer are relatively insignificant over the chosen parameter space. Stated another way, the value of the instantaneous freestream is high enough in each case that the pressure gradient incurred by the spatial velocity gradients far outweighs the pressure gradient incurred by temporal velocity gradients, which is shown to hold at least over the parameter space investigated in figure 5.12 ($1.50 \leq \lambda \leq 2.25$).

If the trends in surge amplitude cannot be attributed to unsteady effects in the boundary layer, then the wake must play a significant role in the onset of sepa-

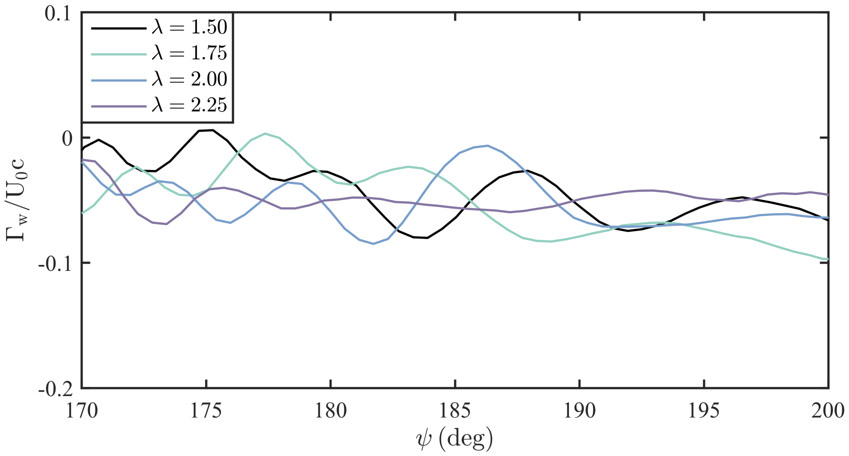

Figure 5.13: The impact of surge amplitude on the strength of the near wake (Γ_w) for four surge amplitudes at constant reduced frequency and pitch kinematics.

ration. Figure 5.13 plots the strength of the near wake (Γ_w) immediately preceding and following flow separation ($170° < \psi < 200°$). Again, this figure shows very similar results for each of the four surge amplitudes, implying that the difference in acceleration is not significant enough to cause variation in the dimensional wake strength. The role of the wake, however, can be made more clear by considering figure 5.13 in relation to the instantaneous velocity of the wing. As an illustration, figure 5.14 sketches the wing near separation ($180° < \psi < 190°$) for two representative surge amplitudes, one lower amplitude ($\lambda = 1.50$) and one higher amplitude ($\lambda = 2.25$). The flow near the leading edge in both cases can be broken down into a "quasi-steady" component due to the instantaneous surge/pitch motion of the wing (U_1 and U_2), and an unsteady component induced by the trailing wake (U_w). In dimensional form, figure 5.13 suggests that U_w is roughly the same magnitude for $\lambda = 1.50$ and $\lambda = 2.25$; the "quasi-steady" component, however, is lower for the high surge amplitude if $\psi > 180°$. The higher surge amplitude is thus subject to a

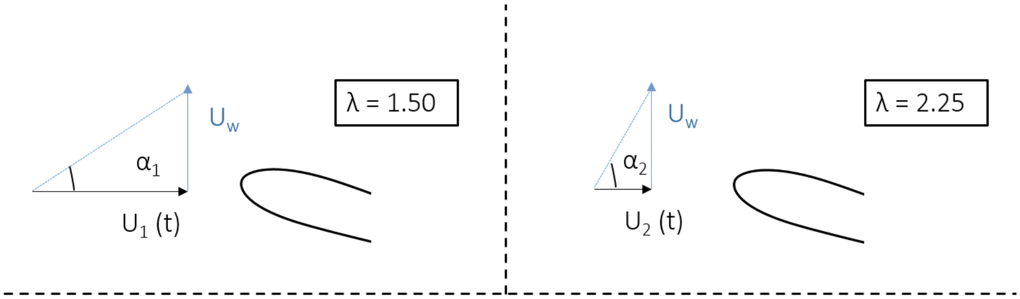

Figure 5.14: Illustration of how the wake-induced velocity, although relatively constant across the four surge amplitudes, acts to increase the effective incidence near the leading edge.

higher effective incidence, which can explain the earlier vortex formation observed in figure 5.10.

The preceding discussion suggests that it is the influence of the trailing wake, rather than unsteady boundary layer effects, that has the most profound impact on the timing of vortex formation under a change in surge amplitude. As a final comment, we must acknowledge that these two flow features are coupled; that is, the state of the wake affects the boundary layer height throughout the oscillation, and vice versa. With this in mind, the main takeaway of this section is that wake effects are sufficient to cause an increase in pressure gradient near the leading edge and thus induce separation, but they are not significant enough to have a dramatic impact on the height of the boundary layer prior to separation (see figure 5.11). In addition, unsteady effects in the boundary layer, which arise due to the change in dimensional acceleration associated with a change in surge amplitude, do not play a significant role in the onset of separation. These observations will prove to be very useful when we attempt to model the timing of vortex formation on a surging/pitching wing

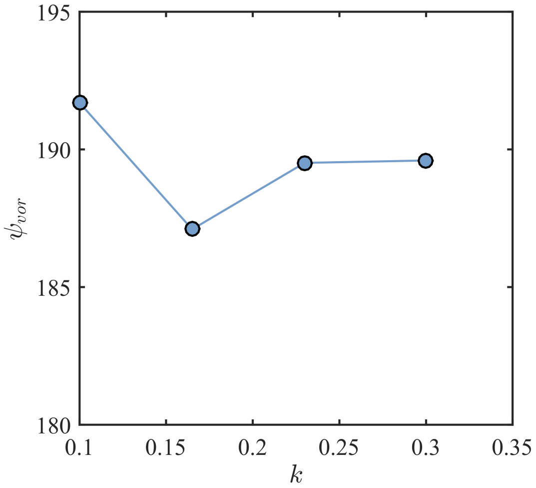

Figure 5.15: The effect of reduced frequency (k) on the timing of vortex formation (ψ_{vor}) for constant pitching kinematics and surge amplitude.

later in this chapter.

5.5 Variation in Reduced Frequency

The purpose of this section is to address the impact of reduced frequency on the timing of vortex formation. The experiments in this section were performed over a wide range of reduced frequencies ($0.100 \leq k \leq 0.300$), while the surge amplitude ($\lambda = 1.75$), pitching kinematics ($\theta_0 = 15°$, $\theta_1 = 8°$, $\phi = \pi$), and mean Reynolds number ($Re_0 = 2.0 \times 10^4$) were again held constant.

Figure 5.15 plots the timing of vortex formation (ψ_{vor}) against reduced frequency (k). Unlike the previously discussed trends in surge amplitude, figure 5.15 does not show a clear relation between the timing of vortex formation and a change in the reduced frequency. The plot instead appears relatively invariant (with a maximum change of only $\Delta\psi = 3°$) for a broad range of reduced frequencies, despite the

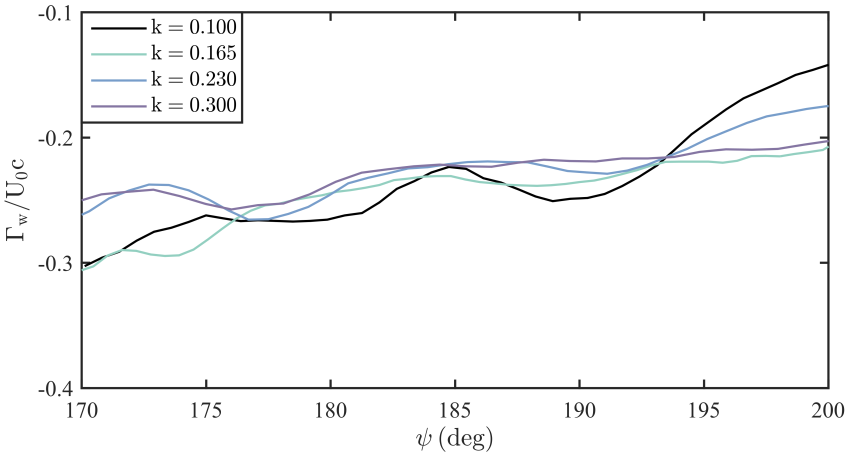

Figure 5.16: The impact of reduced frequency on the strength of the near wake (Γ_w) throughout the surge and pitch oscillation.

large difference in acceleration exhibited over $0.100 \leq k \leq 0.300$. The remainder of this section will relate the unexpected behavior of ψ_{vor} to the state of the wake and the boundary layer, with the goal of physically understanding why the onset of vortex formation is so insensitive to a change in reduced frequency.

Figure 5.16 begins by considering the effect of reduced frequency on the amount of clockwise circulation contained in the near wake. In this figure, the strength of the wake again appears to have a weak dependence on reduced frequency, but in the case of the wake strength, such a result is reasonably expected. Each reduced frequency undergoes the same variation in freestream and incidence in non-dimensional time (see figure 5.3(b)), and thus the wing is expected to shed the same amount of circulation over the period $170 < \psi < 200$ in each case. While it is true that higher reduced frequencies travel a fewer number of chords, and are in turn "closer" to the circulation shed from earlier time-steps, this phenomenon does not appear to have a notable impact on the evolution of the flowfield, at least for $k \leq 0.300$.

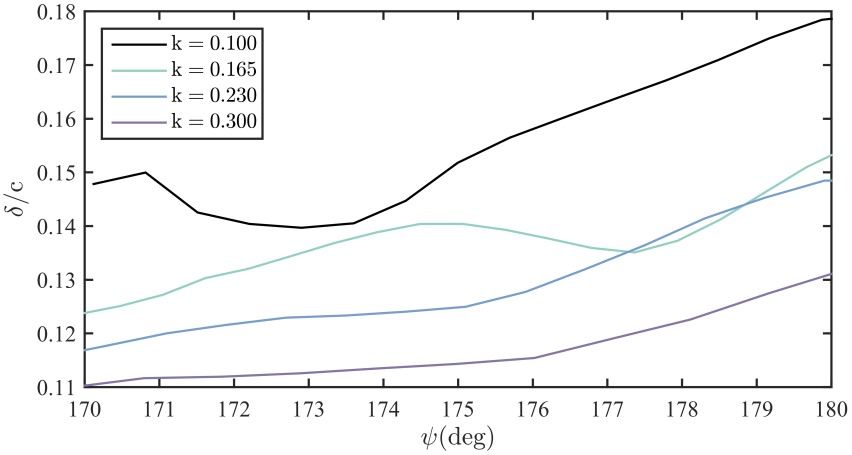

Figure 5.17: The effect of reduced frequency (k) on the height of the boundary layer (δ) in the period of the oscillation ($170 < \psi < 180$) immediately preceding flow separation.

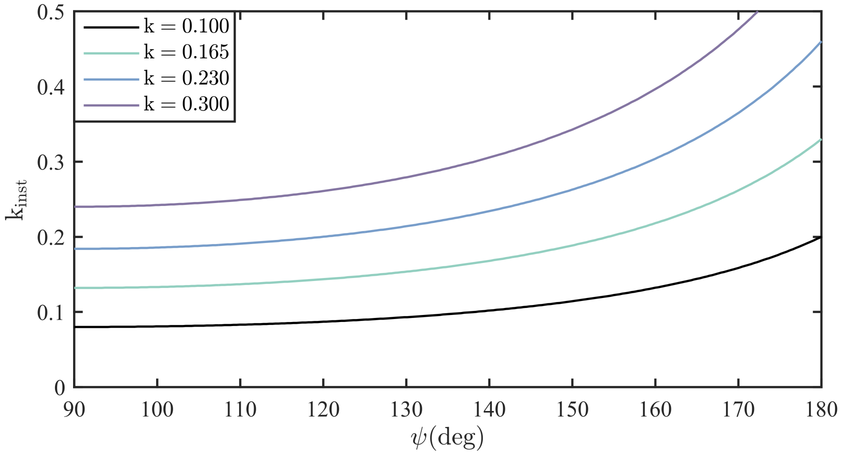

Figure 5.18: The predicted magnitude of unsteady boundary layer effects (k_{inst}) for various reduced frequencies.

If the wake does not show a strong variation with reduced frequency, the only remaining unsteady feature of the flow is the boundary layer. Figure 5.17 plots the height of the boundary layer (δ) versus cycle time during the period preceding flow separation ($170° < \psi < 180°$) for each of the four reduced frequencies. During this period, the boundary layer displays a clear inverse relationship with reduced frequency, as a higher frequency corresponds to a thinner boundary layer, and vice versa. Since neither the wake nor the instantaneous kinematics show much variation with ψ, the trends in figure 5.17 must be attributed to unsteadiness in the boundary layer, as acceleration scales directly with the reduced frequency. A change in reduced frequency is thus seen to primarily manifest as a change in the relative magnitude of unsteady boundary layer effects and, in turn, a change in the height of the boundary layer.

It is important to note that the trends in figure 5.17 are somewhat at odds with the weak dependence of ψ_{vor} discussed at the beginning of this section. One would expect a thinner boundary layer, and in turn a higher reduced frequency, to be consistently associated with a delay in the onset of vortex formation. One must keep in mind, however, that an increase in the boundary layer height also reduces the value of the boundary layer exterior velocity, so the trends in figure 5.17 do not necessarily imply earlier flow separation at lower values of k. In addition, the differences in boundary layer height in figure 5.17 are still reasonably small, especially considering the large range of reduced frequencies covered. Such an assertion is supported by figure 5.18, where the expected magnitude of unsteadiness (k_{inst}) is less than O(1) even for the highest reduced frequency. Together, figures 5.15 and 5.17

imply that an increase in reduced frequency does lead to a thinning of the boundary layer due to unsteady effects, but this does not significantly impact the timing of flow separation. Unsteady boundary layer effects remain secondary compared to the inviscid features of the flow, including the wing kinematics and wake contribution, up through $k = 0.300$.

5.6 Modeling the Blunt-Edge Vortex

The previous sections uncovered two main observations regarding the formation of a blunt-edge vortex on a wing undergoing a high-amplitude surging oscillation. First, the trailing wake appeared to play a critical role in the onset of vortex formation, as the wake-induced component of velocity becomes increasingly significant during the wing's freestream deceleration. Second, unsteady boundary layer effects were found to be secondary compared to "quasi-steady" features of the boundary layer, and the timing of vortex formation showed a weak dependence on dimensional acceleration for $k < 0.300$. Together, these observations serve as a guide for what features of the flow are most impactful in initiating vortex formation on a 2-D surging and pitching airfoil. The following section attempts to leverage this knowledge into a low-order prediction of the timing of vortex formation on a simultaneously surging/pitching wing. Unlike more conventional predictions of dynamic stall, the method outlined here directly accounts for large freestream variations, making it a particularly palatable avenue for modeling separation on a rotor at high advance ratio. In addition, the method is developed with the intent of minimizing the re-

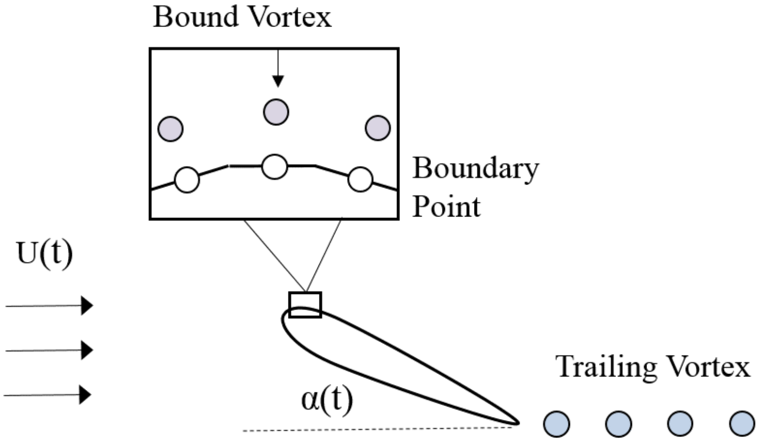

Figure 5.19: Illustration of the current method for predicting the inviscid flow around a surging/pitching airfoil with a finite thickness and a rounded leading edge.

quired number of empirical parameters, meaning its uses and limitations are clearly grounded in the physics of separation.

5.6.1 The Inviscid External Flow

As covered in chapter 2, physics-based predictions of flow separation generally involve the coupling of (1) a model for the inviscid flow outside the boundary layer, and (2) a separate treatment of the viscous flow within the boundary layer. In this way, one can think of the current modeling task as an extension of the discrete vortex method detailed in section 5.5. The unsteady, inviscid portion of the flow can be still be captured by strategic placement of point vortices in the flow, but the viscous flow near the wing surface must now also be included since separation is not always guaranteed about the rounded edge of an airfoil. In order to implement this boundary layer model, our inviscid methodology must be slightly adjusted to account for the shape of the airfoil's rounded leading edge.

Figure 5.19 illustrates the inviscid component of the separation model developed in this chapter. An airfoil with a finite thickness, in our case a NACA 0012, is discretized into $N = 40$ panels. Much like the discrete vortex method from section 5.5, the mid-point of each panel is designated as a boundary point, and a bound vortex is placed a distance $d_0 = 0.001c$ normal to each panel. At each time step, the strength of the N new bound vortices is determined by enforcing the flow tangency condition at each boundary point, and the system is closed by invoking Kelvin's theorem for the flow at large. The trailing wake, which was found to play an integral role in the onset of vortex formation for high surging amplitudes, is again incorporated by denoting the rearmost vortex as a "free" vortex at each time step and allowing it to convect. In addition, the Kutta condition is enforced by simply designating the sharp trailing edge of the airfoil as one of the boundary points. The streamfunction Ψ is then required to be finite at the sharp edge of the wing, removing the possibility of a singularity at the trailing edge, and thus ensuring that flow near the trailing edge behaves as expected.

The above methodology alone provides sufficient information for a calculation of the flow outside the boundary layer up until the onset of vortex formation. It is worthwhile to note, however, that the current method is also amendable to a prediction of the flow following the onset of separation, when the blunt-edge vortex is in its growth stage. After flow separation has been initiated, for instance, one can simply denote the bound vortex at the blunt edge of the wing as a "free" vortex and adjust its strength as follows:

$$\Gamma_{LE} = \left(\frac{U_{LE}^2}{2}\right)\Delta t \tag{5.6}$$

where U_{LE} is the slip velocity at the blunt leading-edge, and Δt is the time step in seconds. The new "free" leading edge vortex is then allowed to convect with the local flow velocity before bound vortices are calculated at the next time step. Such a process, wherein vortex particles are shed from the leading edge following separation, is implemented in later sections as a way of comparing the current method to more "classical" models of the dynamic stall process.

5.6.2 The Viscous Boundary Layer Flow

When predicting separation, a calculation of the inviscid external flow is typically only the first step; the real challenge of these methods lies in properly representing the boundary layer. Following the inviscid calculation, low-order predictions of separation generally extract the inviscid slip velocity at the surface of the airfoil, then use that slip velocity as a boundary condition for solving the boundary layer equations in two dimensions. The fidelity with which these two steps are combined ranges from the very basic [111, 112] to the much more rigorous [76, 78, 82]. The more involved methods, however, are typically reserved for applications that seek the value of skin friction along the entire surface of the airfoil. Since we are only interested in predicting the flow near the leading edge, the method presented in this section requires minimal computational effort, yet still captures the essential physics of blunt-edge vortex formation discussed in the previous sections.

As a starting point, let us consider the laminar form of the unsteady boundary layer equations in two dimensions, which expresses conservation of momentum in the region very close to the wing. In terms of the inviscid flow properties, this equation can be stated as follows:

$$\frac{\partial u}{\partial t} + u\frac{\partial u}{\partial x} + v\frac{\partial u}{\partial v} = \left(\frac{\partial U_e}{\partial t} + U_e\frac{\partial U_e}{\partial x}\right) + \nu\frac{\partial^2 u}{\partial y^2}, \tag{5.7}$$

where x and y are the directions tangent and normal to the wing surface, respectively; u and v are velocity components within the boundary layer; and U_e is the exterior velocity of the boundary layer (taken from the inviscid solution). Equation 5.7 represents the governing equation for the viscous component of our separation prediction. This equation is a second order partial differential equation in both space and time, and is notoriously difficult to solve, even when neglecting turbulence and 3D effects. The well-known integral methods can significantly simply equation 5.7 by integrating in the wing-normal direction [63, 75, 113], but for an unsteady flow, one is still left with a partial differential equation in space and time, which can require an excessively small time step to solve numerically. The presence of the unsteady term $\partial u/\partial t$ is a major computational barrier preventing timely, accurate solutions to equation 5.7.

The first step of the current boundary layer method is to assume that unsteady effects in the boundary layer are small. The analysis of section 6.5 suggests that this is a reasonable assumption, at least up through $k = 0.300$, and that the unsteady term in equation 5.7 can be assumed to be negligible for a significant portion of our parameter space. Such an assumption allows one to approach the flow in boundary layer using the steady form of equation 5.7, a partial differential equation in x and y that is much more manageable to solve computationally.

The elimination of the unsteady term also allows one to re-write equation 5.7 in a more mathematically convenient form. Consider, for example, the Görtler transformation of the steady boundary layer equations (stated in reference [112]), which re-posits equation 5.7 as follows:

$$f''' + ff'' + \beta\Big(1 - f'^2\Big) = 2\zeta\Big[f'\Big(\frac{\partial f'}{\partial \zeta}\Big) - f''\Big(\frac{\partial f}{\partial \zeta}\Big)\Big]. \tag{5.8}$$

In equation 5.8, the variable f represents a non-dimensional form of the stream-function in the boundary layer, ζ represents the non-dimensional wing-tangent direction, η represents the non-dimensional wing-normal direction (the 'prime' terms are derivatives in η), and β is a non-dimensional version of the local pressure gradient. Equation 5.8 is convenient in the sense that it groups all wing-tangent terms to a single side of the equation. The right-hand side of equation 5.8 can thus be physically interpreted as accounting for the wing-tangent momentum of fluid particles in the boundary layer, which inherently acts against the mechanisms of flow separation, while the left-hand side of equation 5.8 accounts for the interplay between viscous forces and the local pressure gradient.

The terms on the right-hand side of equation 5.8 also have an important computational implication. If these terms are assumed to be negligible, equation 5.8 no longer requires a spatial integration in ζ, and the flow in the boundary layer

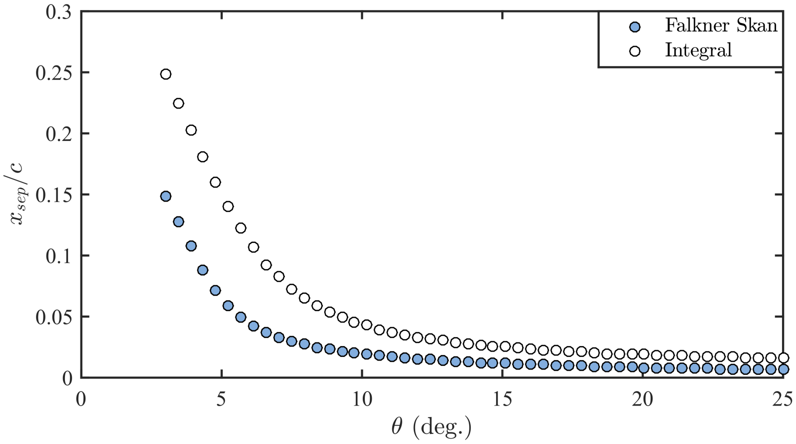

Figure 5.20: Prediction of the laminar separation on a 12% thick Joukowsky airfoil at static incidence using the Pohlhausen integral method (white) and the Falkner-Skan Method (blue).

can be solved locally in a computationally efficient fashion. The scenarios in which one can neglect the "non-similarity" terms on the right-hand side, however, are not particularly well-defined, and their magnitude generally varies depending on the specific flow application. With this in mind, a brief computational study was performed to assess the relative impact of non-similarity on our prediction of flow separation. The study involved computing the shear stress at the surface of a 12% thick Joukowsky airfoil at static incidence, which serves as a simple representation of pressure gradients expected on our surging and pitching wing. The shear stress was first calculated using the von Karman-Pohlhausen integral method [114], which accounts for the non-similarity terms in equation 5.8, then re-calculated using the "locally similar," or Falkner-Skan, approach, which solves equation 5.8 by setting its right-hand side equal to zero.

Figure 5.20 shows the results of predicting separation, or the point of vanishing wall shear, using the integral method (white) and the Falkner-Skan method (blue). The sweep of incidence angles is plotted on the abscissa, while the streamwise position of separation relative to the leading edge is plotted on the ordinate. Figure 5.20 reveals that the non-similarity terms act to delay the onset of flow separation to more downstream locations, consistent with their physical interpretation, but the importance of these terms decreases as one moves to higher incidence. The two methods predict nearly identical separation points for $\theta > 10^\circ$, suggesting that the local pressure gradient in this regime is of such a large magnitude that the non-similarity terms are immaterial. The behavior seen in figure 5.20 is particularly relevant to our surging/pitching wing experiments, as the onset of blunt-edge vortex formation occurs in this high incidence regime, where the two methods appear to provide very similar results.

The second step of the current boundary layer method is thus to assume that the terms on the right-hand side of equation 5.8 do not significantly impact the prediction of the separation point. The shear stress at a given point on the surface of our surging/pitching wing can then be predicted based on the Falkner-Skan formulation of the boundary layer equations:

$$f''' + ff'' + \beta\left(1 - f'^2\right) = 0. \tag{5.9}$$

Equation 5.9 is perhaps the simplest version of the boundary layer equations that can be seen as still capturing the basic physics of separation. Using equation 5.9, a solution for the shear stress at the surface of a body can be determined based on a single non-dimensional parameter β, defined as follows:

$$\beta = \frac{x}{U_e}\left(\frac{\partial U_e}{\partial x}\right), \tag{5.10}$$

where x is the wing-tangent distance between the current point and stagnation, and U_e is the exterior velocity of the boundary layer. The parameter β physically represents a non-dimensional form of the local pressure gradient, and solutions of equation 5.9 for various values of β are well-tabulated throughout the literature [115]. Of particular interest, the boundary layer profile with zero wall shear, or the position of laminar separation, is known to correspond to a β value of roughly $\beta \approx -0.1988$ [75]. The point of separation on a wing can thus be predicted simply by the stagnation point, the exterior velocity of the boundary, and derivatives of this exterior velocity, all of which can be easily extracted from the inviscid solution to the flow.

The following sections employ the Falkner-Skan method described above to predict the point of laminar separation on various surging and pitching airfoil motions. In each case, the exterior velocity of the boundary layer (U_e) is calculated using the inviscid panel method, while the viscous method predicts a surface shear stress based on the resulting value of β. Of particular importance, the next section will attempt to relate this simple prediction of laminar separation to the timing of vortex formation on our surging/pitching wing experiments.

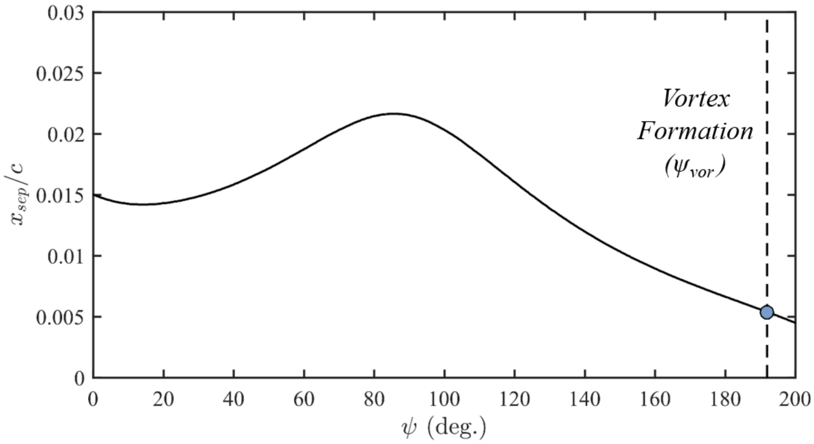

Figure 5.21: The predicted laminar separation point for a NACA 0012 airfoil undergoing a baseline surging ($\lambda = 1.50$, $k = 0.165$) and pitching motion ($\theta_0 = 15°$, $\theta_1 = 8°$, $\phi = \pi$).

5.6.3 Comparison with Surging/Pitching Wing Data

The previous section established that the position of laminar separation could be reasonably predicted based on a Falkner-Skan treatment of the boundary layer equations for the surging and pitching kinematics of interest here. A prediction of the laminar separation point, however, does not directly equate to an accurate prediction of vortex formation; a few additional physical features of the flow have yet to be addressed. This section will use the results of our surging/pitching wing experiments to finalize a method for predicting the onset of vortex formation, before ultimately comparing this prediction to the experimental measurements.

To begin, figure 5.21 plots the position of the laminar separation point (x_{sep}/c), as predicted by the panel method/Falkner Skan methodology, against non-dimensional cycle time (ψ) for a baseline surging and pitching case ($\lambda = 1.50$, $k = 0.165$). This figure reveals an important observation regarding the prediction of laminar separation. That is, the separation point qualitatively behaves as one would expect, with x_{sep} moving downstream during the pitch-down ($0° < \psi < 90°$) and upstream during the pitch-up ($90° < \psi < 270°$), but its quantitative value appears to be very close to the leading edge ($x_{sep} = 0$) throughout the entire surge and pitch oscillation. Such an observation appears to imply that the flow is separated at the leading edge very early in the wing's motion, which we know from observation is not true (see figure 5.4 for one example). There thus appears to be some physical mechanism keeping the flow attached beyond the separation point predicted by figure 5.21.

A likely reason for the apparent inaccuracy in figure 5.21 is that turbulence plays a role in the real flow. Turbulence is known to energize the flow in the boundary layer, and often maintains attachment far longer than an equivalent laminar flow. The laminar prediction of figure 5.21 inherently ignores any flow instabilities, and the existing low-order methods for incorporating turbulence into a boundary layer prediction rely heavily on experimental data [75]. Figure 5.21, however, still has significant value to the current prediction of vortex formation. Turbulent instabilities, for instance, do not necessarily impact the entire boundary layer, as a complete "transition" to turbulence occurs some finite distance away from the stagnation point, usually in the region of adverse pressure gradient. One could reasonably hypothesize that there exists a region of the boundary layer close to the leading edge in which the flow is laminar even for very high freestream Reynolds numbers. If the separation point moves within this region, the predictive methodology of figure 5.21 again becomes a valid way of predicting leading edge separation, which can in turn be used as an estimate for the onset of vortex formation.

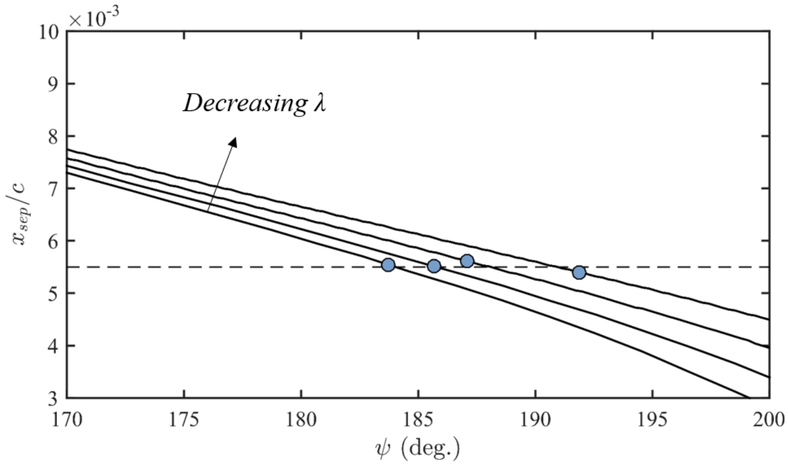

Figure 5.22: The predicted laminar separation point for a NACA 0012 airfoil over various surge amplitudes ($1.50 \leq \lambda \leq 2.25$).

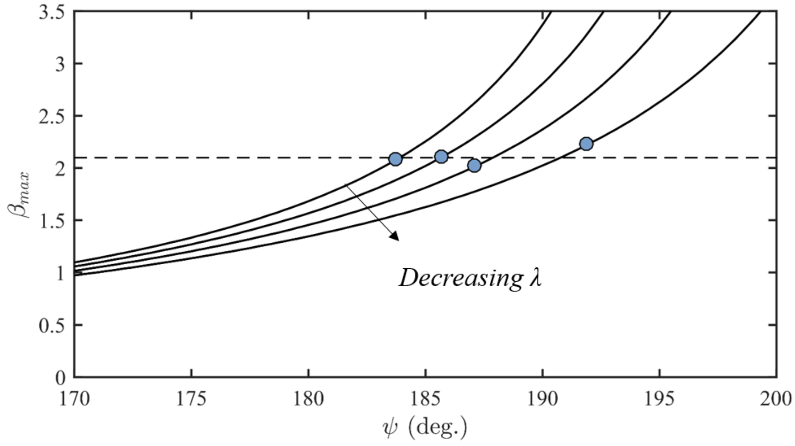

Figure 5.23: The value of the maximum non-dimensional pressure gradient (β_{max}), computed in a region near the leading edge ($0 \leq x/c \leq 0.25$), for a NACA 0012 airfoil over various surge amplitudes ($1.50 \leq \lambda \leq 2.25$).

The above hypothesis is equivalent to saying that the onset of vortex formation correlates with some critical upstream value of the laminar separation point. Figure 5.22, which plots the predicted laminar separation point for each of the four surge amplitude cases, provides evidence of such a correlation. Again, in this figure non-dimensional cycle time is plotted on the abscissa, and the location of the laminar separation point is plotted on the ordinate. The timing of vortex formation taken from experimental measurement (ψ_{vor}) is denoted for each surge amplitude case with a large blue dot. Figure 5.22 reveals that the onset of vortex formation roughly coincides with the passage of the laminar separation point through the same chordwise position on the surface of the wing. That is, for each of the four surge amplitudes, the onset of vortex formation begins when the laminar separation point reaches $x/c \approx 0.0065$. This observation agrees with the notion that the predicted laminar separation point moves upstream until it reaches some critical value near the leading edge, at which point the laminar assumption is valid, and leading edge separation begins.

Now in application, it is not always practical, or even possible, to estimate when the laminar separation point moves to its "critical" upstream position. To resolve the flow near $x/c = 0.0065c$ in figure 5.22, for instance, the number of panels on the airfoil had to be increased to $N = 300$, and a certain amount of filtering was needed to capture the surface velocity gradients near the suction peak. As a way of reducing the spatial resolution required to predict vortex formation, the current method makes use of another observation: that is, as the laminar separation point moves toward the leading edge, the peak value of the non-dimensional pressure gradient (β) increases downstream. To illustrate this idea, figure 5.23 plots the maximum value of β, computed on the suction side of the airfoil in the region $0 \leq x/c \leq 0.25$, in the portion of the cycle immediately preceding flow separation for each of the four surge amplitude cases. The maximum value, or β_{max}, is seen to monotonically increase for each case leading up to the experimentally measured timing of vortex formation (denoted with a blue dot). More importantly, figure 5.23 reveals that β_{max} is roughly constant at the onset of vortex formation, with ψ_{vor} occuring at roughly $\beta_{max} = 2.1$ for each case. The advantage of this observation is that unlike the laminar separation point, β_{max} can be estimated with minimum spatial resolution, as it occurs significantly further downstream than the laminar separation point.

The current work uses the observations of figure 5.23 to complete its methodology for predicting the onset of vortex formation. The complete method can be outlined as follows: for a given time step, the boundary layer exterior velocity is calculated using the inviscid panel method. The exterior velocity distribution is then used to calculate the value of the Falkner Skan parameter (β) on the suction side of the airfoil in a region near the leading edge ($0 \leq x/c \leq 0.25$). If the maximum value of β in this region exceeds $\beta_{max} = 2.1$, the flow is deemed to have separated at the leading edge, and vortex formation begins. If the maximum value of β is less than $\beta_{max} = 2.1$, the flow is said to be attached, and the method continues to time-march until vortex formation is predicted. The only empirical parameter at play in this method is the "critical" value of the Falkner Skan parameter, which in our case is empirically set to 2.1. Note also that this method is not universally expected to be

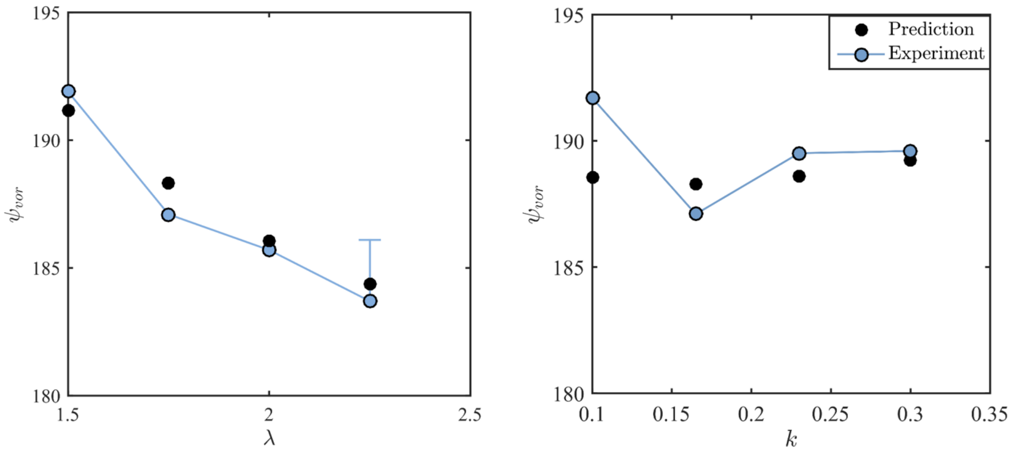

Figure 5.24: The predicted timing of vortex formation (ψ_{vor}) compared to experimental measurement for a sweep of surge amplitudes (λ, left) and reduced frequency (k, right).

valid, as it simply represents a "check" for flow separation at the leading edge of the wing, but for cases of massive flow separation like those considered here, it may prove to be a useful estimation.

Figure 5.24 applies our methodology for predicting the onset of vortex formation to the sweeps in surge amplitude (left) and reduced frequency (right). In each subfigure, the results of the prediction are plotted as solid black dots, while the experimental measurements are plotted as blue dots. The critical value of the Falkner Skan parameter was set to $\beta_{max} = 2.1$ for each of the cases presented in figure 5.24, meaning no "tuning" took place between individual cases. The left-hand side of figure 5.24, which corresponds to the sweep in surge amplitude, shows very good agreement between the experimental measurement and the prediction of vortex formation, with both the magnitude and trends in ψ_{vor} being well represented. The right-hand side of figure 5.24 shows that the method is also successful, although somewhat less so, when predicting the trends in reduced frequency. Despite neglecting the presence of unsteady effects in the boundary layer, the prediction of vortex formation never strays far from the experimental values, even if it is unable to capture the secondary variations in ψ_{vor}. Taken together, the subplots of figure 5.24 appear to suggest that the various assumptions inherent to our method (i.e., unsteadiness is negligible in the boundary layer, non-similarity effects are small, and the onset of vortex formation correlates with a critical value of the laminar separation point) are reasonably valid for the parameter space of interest here.

5.6.4 Comparison with the Leading Edge Suction Parameter (LESP)

The basic concept of the method outlined above (i.e., that the onset of vortex formation an be estimated based on the "critical" value of some flow property near the leading edge) is actually common to a few different models of vortex formation found in the literature [42, 59, 80, 116]. One particularly popular model, based on the "leading edge suction parameter" (LESP), was developed specifically for surging, pitching, and heaving airfoil motions, and has been subsequently used to predict vortex formation in applications ranging from a simple pitching wing [79] to the flow over an airfoil encountering a vortex street [81]. The foundational hypothesis of the LESP is that a given airfoil can withstand a finite amount of suction force at the leading edge before flow separation begins. The LESP itself is derived from thin airfoil theory, and its critical value, which determines the timing of flow separation, is empirically determined for each airfoil geometry and Reynolds number combination.

Due to the qualitative similarities between the LESP and our prediction of vortex formation, it is worth exploring the essential similarities and differences between these two models in a bit more detail.

In practice, the current method and the LESP are indeed quite similar. Both methods involve computing the unsteady inviscid flow around an airfoil, calculating its exterior velocity, then using that exterior velocity to determine some critical parameter near the leading edge. In terms of theory, however, there lies an important difference. Whereas the LESP hypothesis suggests that a critical pressure force determines the onset of flow separation, the current work uses the local non-dimensional pressure gradient, a local parameter calculated independent of geometry, to accomplish the same task. The main difference then is that the critical value of the non-dimensional pressure gradient in the current method does not need to be re-calibrated for each airfoil geometry. Since the Falkner-Skan parameter includes a spatial derivative ($\partial U_e/\partial x$), the current method inherently accounts for differences in geometry, and its critical value should theoretically be constant across multiple airfoil shapes. This makes the current method quite desirable for airfoil design applications, where a large number of geometric iterations are completed before arriving at a final airfoil cross-section.

These essential similarities and differences are on display in figure 5.25. Here, the current method and the LESP were both used to predict the timing of vortex formation on an SD7003 airfoil (8.5% thickness, 1.2% maximum camber) undergoing a linear pitch-up at constant freestream Reynolds number ($Re = 2\times10^4$). The LESP predictions were taken from a numerical data set that employed a high-fidelity CFD

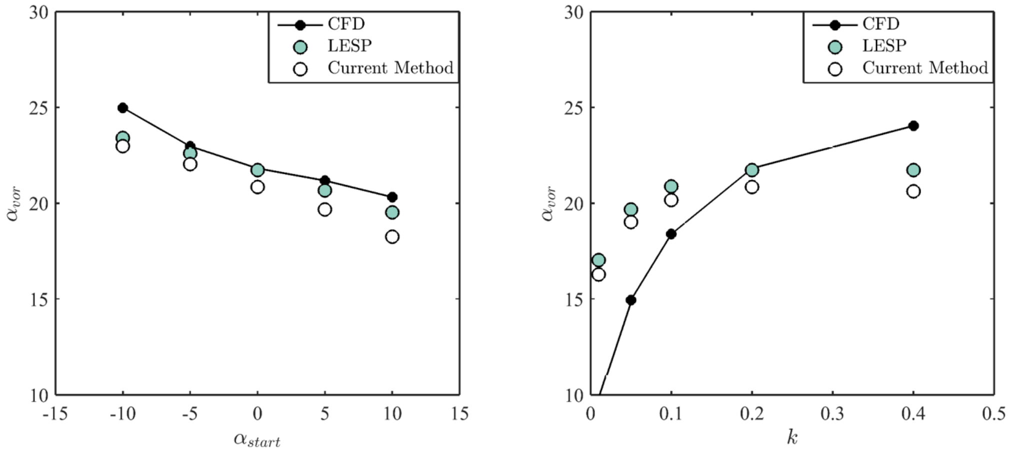

Figure 5.25: The angle of vortex formation as predicted by the current method (white dot), the LESP (green dot), and high-fidelity CFD (black line) for an SD7003 airfoil undergoing a linear pitch-up maneuver at $Re = 2 \times 10^4$.

simulation, the results of which are shown as a solid black line for reference, to establish the operating range of an LESP-based discrete vortex method [79]. In each subfigure, a sweep of pitching kinematics is plotted on the abscissa, and the angle corresponding to vortex formation is plotted on the ordinate. The current method was run using a critical non-dimensional pressure gradient of $\beta_{max} = 2.1$ (i.e., the same critical value used for the NACA 0012 in figure 5.24), while the LESP-based method was run using a critical value of the LESP empirically estimated specifically for the SD7003 airfoil.

Figure 5.25 reveals that the two methods perform very similarly in the context of a pitching wing in constant freestream. The current method slightly underpredicts the angle of vortex formation compared to the LESP, but the two models still behave almost identically across sweeps in starting angle (α_{start}, left) and reduced frequency (k, right). The current method in turn displays many of the same limitations of the LESP, as neither performs particularly well at low reduced frequency ($k < 0.1$), where a gradual trailing edge separation is an integral part of the vortex formation process. The current method, however, has the added advantage of being able to use to the same "critical value" ($\beta_{max} \approx 2.1$) across multiple airfoil geometries. One can thus view the current method, where vortex formation is predicted based on a critical pressure gradient (β_{max}), as having roughly the same accuracy as the LESP, but an expanded range of applicability. The expanded range is a result of including more information, namely a spatial gradient in exterior velocity ($\partial U_e/\partial x$), in the parameter used to predict the onset of vortex formation.

5.6.5 Comparison with Dynamic Stall Experiments

As a final comment, our method for predicting the onset of vortex formation is compared to the results of "classical" dynamic stall experiments. These experiments, which address a pitching wing at constant freestream, have served as a benchmark for many models of airfoil dynamic stall; the early semi-empirical models of dynamic stall, including the Leishman-Beddoes [42] and ONERA methods [43], were developed specifically to match these fundamental studies. Such models remain in use in the vast majority of modern rotorcraft design codes, but it must be kept in mind that they require the tuning of several empirical parameters (sometimes dozens) to match the experimental values of airfoil lift and drag. The current method is compared to a classical experiment with the crucial advantage of having only a single empirical parameter, the critical pressure gradient (β_{max}), the value of which is expected to be constant across a wide parameter space.

Figure 5.26 shows the predicted value of the lift coefficient, calculated using the vortex impulse method [117], for a NACA 0012 airfoil undergoing dynamic stall at three reduced frequencies ($0.10 \leq k \leq 0.25$). In each subfigure, the angle of attack (α) is plotted on the abscissa, and the coefficient of lift (c_l) is plotted on the ordinate. An experimental dynamic stall curve, taken from the experiments of McAlister et al. [38], is also plotted in each subfigure for comparison. Note that each run of the predictive method was performed assuming a critical non-dimensional pressure gradient of $\beta_{max} = 2.1$, which again, is the same value used for the simultaneous surging/pitching prediction (figure 5.24) and the linear pitch-up predictions (figure 5.25).

Although the agreement is not perfect, figure 5.26 shows that the current method is able to reasonably estimate the lift coefficient of a pitching NACA 0012 airfoil without any empirical adjustments. The slope of the attached flow portions ($\alpha < 15°$) are decently well-approximated in each curve, and the time of vortex formation, corresponding to the sudden spike in lift curve slope near $\alpha \approx 22°$, reasonably matches the experiments, especially for the $k = 0.100$ case. Since the current method does not include a re-attachment model, the predicted c_l value is not shown during the pitch-down portion of the motion, but know that the agreement between the two curves begins to significantly falter. This limitation is not expected to be a problem for cases on a high advance ratio rotor, however, as the presence of a reverse flow region "cuts off" the dynamic stall process and eliminates the period of reattachment (see figure 5.4).

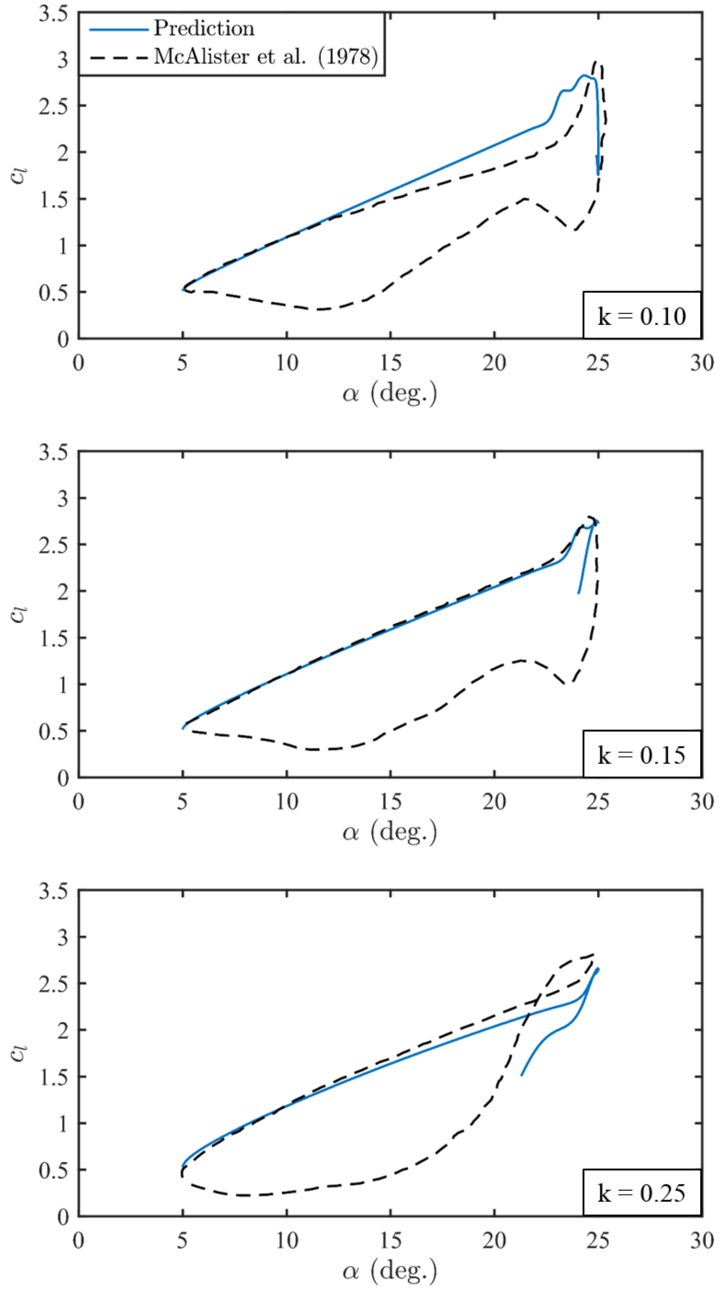

Figure 5.26: The prediction of lift coefficient (blue line) compared to its experimentally value from McAlister et al. [38] for a pitching NACA 0012 airfoil at various reduced frequencies (note: $\theta_0 = 15°$, $\theta_1 = 10°$).

The inaccuracies of figure 5.26 can be attributed to a number of sources. First, it is important to recall that unsteady boundary layer effects were only deemed negligible for cases with a large freestream oscillation, representative of a high advance ratio rotor; it is unclear whether the same is true for a pitching wing at constant freestream. Likewise, although the critical value of β_{max} appears to be independent of airfoil geometry, the timing of vortex formation is expected to exhibit some dependence on Reynolds number, which is not captured in the current method without tuning the value of β_{max}. Finally, we note that discrete vortex methods themselves are known to introduce errors in the convection of vortex particles, even for cases where the timing of flow separation is known exactly. The accuracy of force prediction in discrete vortex methods in general is an ongoing topic of research, one that is now seen to have major application in the prediction of airfoil dynamic stall.

Even with these drawbacks and sources of error, the current method of predicting vortex formation, which combines a simple panel method with a Falkner Skan treatment of the boundary layer, does seem to achieve very reasonable results, and provides a promising avenue for representing blunt-edge vortex formation in a low-order fashion.

5.7 Chapter Summary

The purpose of this chapter was to address the second vortical structure observed on a rotor at high advance ratio: the vortex emanating from the blunt edge of the rotor blade. This goal was approached in a slightly different fashion compared to previous sections. Rather than analyzing the 3-D flowfield of a spinning rotor, this chapter simplified the conditions of a blade element in forward flight with a set of 2-D surging and pitching wing experiments as a way of isolating the seldom-studied impact of a large amplitude freestream oscillation. These experiments involved a sweep in surge amplitude (λ) and surge reduced frequency (k) for a constant set of pitching kinematics. The resulting physical observations were then leveraged into a boundary layer method for predicting the onset of vortex formation on an airfoil with a rounded leading edge. The experimental measurements and the ensuing modeling effort led to a number of important conclusions.

First, the basic stages of blunt-edge vortex formation were visualized by considering a baseline set of surging/pitching kinematics. From phase-averaged flowfield measurements, the onset of vortex formation was observed to consistently occur during the pitch-up/deceleration portion of the wing's oscillation cycle. Freestream reversal, which was present for any case with a surge amplitude $\lambda > 1$, acted to "cut-off" the growth of the blunt-edge vortex, which was then seen to convect away from the wing as the magnitude of the reversed freestream increased. The unique shedding and convection behavior of the blunt-edge vortex allowed us to develop a method for experimentally estimating the timing of vortex formation at the leading edge, a measurement that combined the timing of freestream reversal, the final strength of the vortex, and a time-history of its growth rate.

Next, these experimental measurements were explored in the context of changing the amplitude (λ) and the reduced frequency (k) of the surge oscillation. In the first set of experiments, a change in the surge amplitude was found to uniformly shift the onset of vortex formation to earlier times in the wing's motion. Such an observation was attributed to an increase in the relative magnitude of the wake-induced velocity, and in turn the effective incidence of the wing, during the deceleration portion of the wing's motion. In the second set of experiments, a change in reduced frequency had very little impact on the timing of vortex formation, despite a change in the height of the boundary layer. The latter observation suggested that unsteady boundary layer effects play a small, secondary role in the timing of vortex formation on a surging/pitching wing.

The final stage of this analysis attempted to leverage these observations into a low-order method for predicting the onset of vortex formation. Beginning with the boundary layer equations in two dimensions, it was found that a Falkner-Skan treatment of the boundary layer may be a reasonable way of estimating the laminar separation point on our surging/pitching wing. What's more, the onset of vortex formation appeared to coincide with a "critical" local maximum in the Falkner-Skan pressure gradient parameter (β) for each of our surge amplitude cases. This led to a predictive methodology that first calculated the boundary layer exterior velocity using an inviscid panel method, then "checked" for separation in a region near the leading edge based on the value of the Falkner Skan parameter. This method, which compared well with similar models found in the literature, has the distinct advantage of using only a single empirical parameter (the critical value of β_{max}), the value of which that is not expected to vary across different airfoil shapes. Note that the method proposed here does not account for Reynolds number effects, and it performs poorly in cases that involve a gradual trailing edge separation, but it nonetheless represents a promising avenue for physics-based modeling of blunt-edge vortex formation, especially for the environment of a high advance ratio rotor.

Chapter 6: Conclusions

6.1 Summary

The current work represents a mixed experimental and computational approach to investigating the separated flow on a rotor operating at high advance ratios. The ultimate goal was to understand how separated flow structures, particularly those in the reverse flow region, evolve spatially and temporally on a rotor at high advance ratio, and to leverage that understanding into a widely applicable model for use in rotorcraft design. The analysis of the previous chapters resulted in a number of key observations and conclusions regarding the physics of vortex formation in a 3-D rotor environment, a summary of which will be provided here.

The first part of this thesis detailed the results of an experimental campaign aimed at obtaining flowfield measurements on a sub-scale, articulated rotor system operating in the high advance ratio regime ($0.60 \leq \mu \leq 0.80$). The rotor system was outfitted with four un-twisted, un-tapered NACA 0012 rotor blades, and phase-averaged, three-component flowfield measurements were collected for a single blade passing through a portion of the reverse flow region ($250^\circ \leq \psi \leq 290^\circ$). From these flowfield measurements, two unique vortical structures were identified in reverse flow: one vortex structure at the sharp edge of the blade (the “sharp-edge” vortex) and a second vortex structure emanating from the blunt edge of the blade (the "blunt-edge" vortex). Both of these flow structures, due to their proximity to the surface of the blade in reverse flow, are believed to contribute to the large spike in torsional loading associated with high advance ratio configurations. In addition, the sharp-edge vortex was found to increase in strength at inboard stations of the rotor, indicating a strong spanwise gradient in vorticity directed from the blade tip to blade root, and exhibited close quantitative agreement with a high-fidelity CFD simulation of the same rotor system, performed using an in-house finite volume solver.

The second part of this thesis addressed the physics of these flow structures individually, beginning with the sharp-edge vortex. This flow structure was subject to a vorticity transport analysis using the high-fidelity results of our CFD simulation. The analysis revealed that the net transport due to 3-D mechanisms of the flow, including spanwise convection, vortex tilting, and Coriolis effects, was in fact negligible when the sharp-edge vortex remained coherent (i.e., prior to "vortex burst"). Such an observation was attributed to the vortex tilting and Coriolis transport terms being oriented opposite one another; if these two terms are roughly of the same magnitude, which was proven to be true for most rotors in reverse flow, then the net contribution from 3-D effects is quite small. The sharp-edge vortex was in turn successfully modeled using a simple, 2-D discrete vortex method over a significant portion of the reverse flow region.

Note that the idea of 3-D flow physics being negligible in reverse flow is one of the main takeaways from this thesis. It is a feature unique to the reverse flow region, and implies that a model of the sharp-edge vortex can neglect 3-D effects entirely without sacrificing much in the way of accuracy, significantly reducing the computational rigor required to capture its growth and convection.

The next portion of this thesis investigated the vortex that appeared to emanate from the blunt edge of the rotor blade in reverse flow. This flow structure is similar to a conventional "dynamic stall" vortex, but is unique in that its formation is significantly impacted by the large-amplitude freestream oscillation experienced by a rotor blade element in high advance ratio flight. A series of 2-D surging and pitching wing experiments were undertaken as a way of isolating the impact of this unsteady freestream velocity on the formation of the blunt-edge vortex. The resulting flowfields were analyzed in terms of the time at which vortex formation began, and compared over a sweep of surge amplitudes ($1.50 \leq \lambda \leq 2.25$) and reduced frequencies ($0.100 \leq k \leq 0.300$).

The parameter sweeps revealed two important observations regarding the formation of the blunt-edge vortex. First, the velocity induced by the trailing wake appeared to play a very important role in triggering the onset of separation. As the wing decelerated into reverse flow, the wake-induced velocity became increasingly significant relative to the instantaneous freestream velocity, and eventually dominated the local incidence at the leading edge. Second, unsteady boundary layer effects were found to be insignificant in regard to the blunt-edge vortex. Despite the parameter space covering a large range of dimensional accelerations, the height of the boundary layer prior to separation remained relatively unchanged, implying that quasi-steady mechanisms in the boundary layer are of much higher magnitude. The onset of blunt-edge vortex formation was in turn found to be dominated by "quasi-steady" properties of the flow, such as the instantaneous freestream and incidence, and the contribution of the trailing wake.

The physical observations above were leveraged into a novel separation criterion for blunt leading-edge airfoils undergoing unsteady maneuvers. The shedding criterion is based on the idea that leading edge separation consistently occurs at a critical upstream position of the laminar separation point. In practice, separation is initiated when the maximum value of the Falkner Skan parameter along the airfoil ($\beta = \frac{1}{U_e}\frac{\partial U_e}{\partial x}x$) exceeds a critical value empirically correlated to the onset of flow separation. When combined with a simple unsteady panel method, this shedding criterion was able to predict the timing of vortex formation in our surging/pitching wing experiments with an accuracy similar to other methods found in the literature. The current criterion, however, is unique in the sense that the "critical" value of the Falkner Skan parameter is the only empirical component of the method, and it theoretically does not depend on the airfoil geometry, meaning it has a wide range of applicability.

Putting all of this together, the current work has gathered many new insights into the physics of flow separation in a rotating wing environment, and used those insights to establish a viable modeling framework for the aerodynamics of high advance ratio rotorcraft. In our CFD analysis, the sharp-edge vortex was found to be dominated by the 2-D generation and convection of vorticity; this flow structure was in turn successfully modeled via a simple 2-D discrete vortex method (with shedding from the sharp edge). In our 2-D surging and pitching wing experiments,

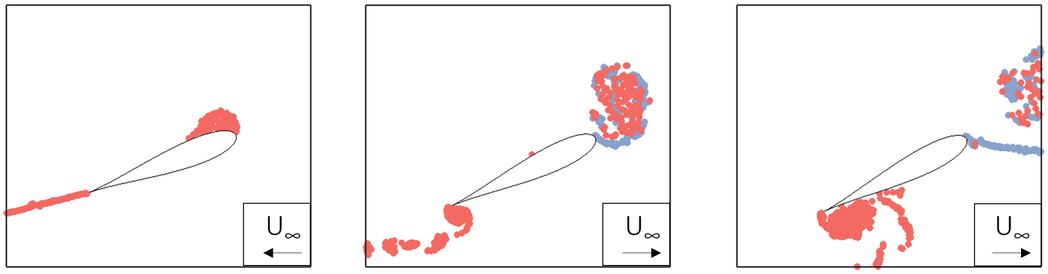

Figure 6.1: Demonstration of the discrete vortex method's ability to capture the vortices at the blunt and sharp edges of a rotor blade element as it transitions into reverse flow in high advance ratio forward flight.

the formation of the blunt-edge vortex was found to be independent of unsteady boundary layer effects; the initiation of this flow structure was then modeled based on the "quasi-steady" Falkner Skan equation. Together, our observations have allowed for the construction of a model that accounts for separation from both the blunt and sharp edges of a rotor blade, all while using minimal empirical parameters. This approach offers unique insight into the dynamics of a separated flow in the 3-D environment of a rotor at high advance ratio.

Figure 6.1 provides a final example of the flowfield predicted by our discrete vortex method, and serves as a concise summary of many of the important takeways from this thesis. In each subfigure, the position of counter-clockwise vortex particles are plotted with red dots, and clockwise vortex particles are plotted with blue dots. The model clearly captures the blunt-edge vortex, which begins its formation prior to reverse flow, the reversal of the trailing wake, and the rollup of the sharp-edge vortex, which evolves throughout reverse flow. The model is certainly not exact; in particular, it neglects the "vortex burst" phenomenon in the evolution of the sharp-edge vortex and is expected to be inaccurate in cases with a gradual trailing edge separation. However, it does offer a computation time on the order of minutes, features minimal empirical parameters, and is supported by the physical observations (i.e., 3-D effects are negligible in reverse flow, and unsteady boundary layer effects play a only small role in initiating separation outside of reverse flow) made throughout this thesis. The physics of separation on a high advance ratio rotor thus appear to be such that a discrete vortex method is a very reasonable option for predicting the onset and evolution of separated flow.

6.2 Original Contributions

The current work provides a number of unique contributions to the understanding and modeling of separated flows, especially in the context of rotorcraft aerodynamics. The most significant of these contributions can be stated as follows:

1. The flowfield of a Mach-scale, "slowed" rotor system has been visualized through three-component flowfield measurements at a variety of advance ratios ($0.60 \leq \mu \leq 0.80$) and radial stations ($0.30 \leq r/R \leq 0.60$). Focusing on the reverse flow region, the measurements revealed the presence of a "sharp-edge" vortex, a "blunt-edge" vortex, a tip-to-root spanwise flow, and a strong tip-to-root gradient in vorticity. These measurements expand on the work of Lind et al. [24] by providing flowfields at multiple radial stations, and expand on the work of Hiremath et al. [25] by considering the evolution of the flowfield over successive azimuths.

2. A RANS-based finite volume solver, developed by Jung et al. [91, 92, 93] for use in rotorcraft application, has been verified in its ability to quantitatively capture the evolution of the coherent sharp-edge vortex that forms in reverse flow at high advance ratio.

3. The 3-D vortex dynamics of the sharp-edge vortex have been explored at high advance ratio using the vorticity transport analysis procedure of Wojcik and Buchholz [86]. It has been found that the net role of 3-D vortex dynamics is quite small prior to the onset of vortex burst due to the cancellation of the Coriolis and spanwise convection/tilting terms. This finding is expected to hold on any rotor where the in-plane velocity gradients are larger than the spanwise gradients, a very reasonable assumption when the rotor blade is at high incidence.

4. A 2-D discrete vortex method has been developed that can properly capture the growth rate of the sharp-edge vortex prior to vortex burst. This model represents a very useful avenue for modeling separated flow structures in rotorcraft design and supports the notion that 3-D effects are negligible in reverse flow.

5. The fundamental impact of an unsteady freestream oscillation on the behavior of a blunt-edge vortex (or “dynamic stall” vortex) has been evaluated in a series of 2-D surging and pitching wing experiments. This work catalogs the timing of vortex formation for a variety of large surge amplitudes ($1.50 \leq \lambda \leq 2.25$) and reduced frequencies ($0.100 \leq k \leq 0.300$), both of which are directly

representative of the conditions on a high advance ratio rotor.

6. A novel vortex shedding criterion has been developed for blunt-edge airfoils undergoing unsteady surging and pitching maneuvers. The shedding criterion is an empirical parameter based on the Falkner Skan formulation of the boundary layer equations, and its critical value is expected to be independent of airfoil geometry.

6.3 Suggestions for Future Work

The current work was aimed at gaining a fundamental understanding of separated flow on a rotor in three dimensions. One must keep in mind, however, that there are still numerous avenues for investigation related to the aerodynamics of a high advance ratio rotor. The following section provides a few suggestions for continuing this work and improving the current understanding (and modeling potential) of the high advance ratio regime:

1. The 3-D flowfield measurements presented in chapter 3 were limited to a single, simplified rotor system over a subset of advance ratios ($0.60 \leq \mu \leq 0.80$). The inclusion of an auxiliary wing or propellor in this rotor system would more closely approximate the flowfield encountered by a compound helicopter, and could potentially reveal interactions between the vortex structures on the rotor (i.e., the sharp and blunt edge vortices) and those on the auxiliary wing. Such an endeavor has already been the subject of preliminary flowfield measurements [118] and represents an important step in generalizing the current

measurements to a wide variety of high advance rotorcraft configurations.

2. The analysis of the reverse flow region in chapter 4 focused on a conventional airfoil cross-section with a sharp geometric trailing edge. Certain next-generation rotor blades, however, are being designed with a rounded trailing edge to combat separation in the reverse flow region [5]. An exploration of a blunt trailing edge airfoil in reverse flow would offer insight into how successfully this design choice mitigates or delays the process of vortex formation on a high advance ratio rotor. Past studies have tested elliptical blades at high advance ratio in the context of performance and control [119], but there is still much to be learned regarding the flow over a rounded trailing edge airfoil in the three-dimensional environment of a rotor.

3. Chapter 4 noted that 3-D effects were negligible in the reverse flow region assuming that spanwise gradients were much lower magnitude than in-plane gradients. Although this assumption was validated over a large parameter space for our simplified rotor system, it remains to be seen how the inclusion of blade twist, which will inevitably increase gradients in vorticity along the span, impacts the conclusion made here.

4. The blunt-edge vortex (or the vortex that forms prior to the blade's entrance into reverse flow) was studied in the context of a 2-D surging and pitching wing due to the unknown effects of a time-varying freestream on the onset of vortex formation. There are several additional effects, including the impact of Reynolds number and 3-D vortex dynamics, that were not addressed

in the current work. Studying the blunt-edge vortex in a 3-D environment would allow for additional evaluation of the modeling framework developed in chapter 5.

5. A discrete vortex model was developed that is capable of capturing the major features of flow separation at high advance ratio, but it did not include any kind of reattachment model (the flow was simply assumed to reattach at the exit of the reverse flow region). The incorporation and evaluation of reattachment criterion could make the present model applicable to wider of variety of intermittently separated flows.
6. The low-order models developed here were evaluated in terms of their ability to capture properties of the flowfield, such as vortex strength and formation time. Their ability to predict unsteady airloads and blade loads, however, was outside the scope of the current work. It is suggested that the current models be coupled, even loosely, to a comprehensive structural dynamics solver such that the discrete vortex method can be assessed in terms of its usefulness in approximating the complete aeromechanics of a rotor at high advance ratio.

Even with the lingering questions noted above, the current work represents an important step toward understanding separated flows in a three dimensional aerodynamic environment. The most important physical conclusions made here, most notably those regarding (a) the direction of spanwise gradients in reverse flow and (b) the criteria for separation about a blunt edge, are fundamental to the 3-D physics of separation on a rotor, and are expected to be valid over a wide range of applications and flight conditions. The current work can thus be seen as a “baseline” understanding of separation on a conventional rotor at high advance ratio. The role of future work will be to leverage these baseline conclusions into an understanding of more complex and realistic rotorcraft configurations, and ultimately, push rotorcraft analysis toward an accurate modeling of next-generation designs.

Bibliography

[1] R.M. Hall and S.H. Woodson. Introduction to the abrupt wing stall program. *Journal of Aircraft*, 41(3):425–435, May 2004.

[2] J. Liiva. Unsteady aerodynamic and stall effects on rotor blade airfoil sections. *Journal of Aircraft*, 6(1):46–51, January 1969.

[3] H. Werle. Hydrodynamic flow visualization. *Annual Review of Fluid Mechanics*, 5:361–386, January 1973.

[4] J.G. Leishman. *Principles of Helicopter Aerodynamics.* Cambridge University Press, 2nd edition, 2006.

[5] A. Bagai. Aerodynamic design of the X2 Technology Demonstrator$^{\text{TM}}$ main rotor blade. In *64th Annual Forum of the AHS*, 29 April–1 May 2008.

[6] P. Roesch. Fast hybrid helicopter with long range with longitudinal trim control. U.S. Patent 8052094, November 2011.

[7] P.S. Bernard. *Fluid Dynamics.* Cambridge University Press, 1st edition, 2015.

[8] L.N. Trollinger. Refined performance and loads of a mach-scale rotor at high advance ratios. Master's thesis, University of Maryland, College Park, May 2017.

[9] C.A. Snyder, M. Robuck, J. Wilkerson, and C. Nordstrom. Summary of the Large Civil Tiltrotor (LCTR2) engine gearbox study. NASA Technical Memorandum 216908, 2010.

[10] W. Johnson, G.K. Yamauchi, and M.E. Watts. NASA heavy lift rotorcraft systems investigation. NASA Technical Paper 213467, December 2005.

[11] J.T.L. Abbe, R.H. Jr. Blackwell, and D.S. Jenney. Advancing Blade Concept (ABC$^{\text{TM}}$) dynamics. In *33rd Annual Forum of the AHS*, Washington, D.C., May 1977.

[12] D.S. Jenney. ABC$^{\text{TM}}$ aircraft development status. In *6th European Rotorcraft and Powered Lift Aircraft Forum*, Bristol, England, September 1980.

[13] J.B. Wheatley and M.J. Hood. Full-scale wind-tunnel tests of a PCA-2 Autogiro rotor. NACA Technical Report 515, 1935.

[14] J.R. Meyer and Gaetano Jr. Falabella. An investigation of the experimental aerodynamic loading on a model helicopter rotor blade. NASA Technical Note 2953, 1953.

[15] G.E. Sweet, J.L. Jenkins Jr., and M.M. Winston. Wind-tunnel measurements on a lifting rotor at high thrust coefficients and high tip-speed ratios. NASA Technical Note D-2462, September 1964.

[16] J.L. Jenkins Jr. Wind-tunnel investigation of a lifting rotor operating at tip-speed ratios from 0.65 to 1.45. NASA Technical Note D-2628, February 1965.

[17] B.O. Berry. *Fundamental Understanding of Rotor Aeromechanics at High Advance Ratio through Wind Tunnel Testing*. PhD thesis, University of Maryland, College Park, 2016.

[18] J.L. McCloud III, J.C. Biggers, and R.H. Stroub. An investigation of full-scale helicopter rotors at high advance ratios and advancing tip mach numbers. NASA Technical Note D-4632, July 1968.

[19] B.D. Charles and W.H. Tanner. Wind tunnel investigation of semirigid full-scale rotors operating at high advance ratios. Bell Helicopter Report 576-099-010, January 1969.

[20] A. Datta, H. Yeo, and T.R. Norman. Experimental investigation and fundamental understanding of a full-scale slowed rotor at high advance ratio. *Journal of the American Helicopter Society*, 58(2):1 – 17, January 2013.

[21] T.R. Norman, P. Shinoda, R.L. Peterson, and A. Datta. Full-scale wind tunnel test of the UH-60A airloads rotor. In *67th Annual Forum of the AHS*, Virginia Beach, Virginia, May 2011.

[22] B. Berry and I. Chopra. Slowed rotor wind tunnel testing of an instrumented rotor at high advance ratio. In *40th European Rotorcraft Forum*, Southampton, England, September 2014.

[23] B. Berry and I. Chopra. High advance ratio wind tunnel testing of a model rotor with pressure measurements. In *Fifth Decennial AHS Aeromechanics Specialists' Conference*, San Fransisco, California, January 2014.

[24] A.H. Lind, L.N. Trollinger, F.H. Manar, I. Chopra, and A.R. Jones. Flowfield measurements of reverse flow on a high advance ratio rotor. *Experiments in Fluids*, 59(185), November 2018.

[25] N. Hiremath, D. Shukla, V. Raqhav, S. Pirau, and N. Komerath. Effects of advance ratio and radial location on the vortex structure on a rotating blade in reverse flow. In *71st Annual Forum of the AHS*, Virginia Beach, Virginia, May 2015.

[26] N. Hiremath, D. Shukla, and N. Komerath. Vortical lift on retreating rotor blades at high advance ratios. *Experiments in Fluids*, 60(92):1–17, May 2019.

[27] M.W. Floros and W. Johnson. Performance analysis of the slowed-rotor compound helicopter configuration. In *4th Decennial Specialists' Conference on Aeromechanics*, San Francisco, California, January 21 -23 2004.

[28] S. Kottapalli. Performance and loads correlation of a uh-60a slowed rotor at high advance ratios. In *American Helicopter Society Future Vertical Lift Aircraft Design Conference*, San Francisco, California, January 18-20 2012.

[29] G.M. Bowen-Davies and I. Chopra. Aeromechanics of a slowed rotor. *Journal of the American Helicopter Society*, 60(3):1–13, July 2015.

[30] T. Theodorsen. General theory of aerodynamic instability and the mechanism of flutter. NACA Technical Report 496, 1935.

[31] W.R. Sears. *A Systematic Presentation of the Theory of Thin Airfoils in Non-uniform Motion*. PhD thesis, California Institute of Technology, 1938.

[32] J.M. Greenberg. Airfoil in sinusoidal motion in a pulsating stream. NACA Technical Report 1326, 1947.

[33] H. Yeo and W. Johnson. Optimum design of a compound helicopter. *Journal of Aircraft*, 46(4):1210–1221, 2009.

[34] K.O. Granlund, M.V. Ol, and A.R. Jones. Streamwise oscillation of airfoils into reverse flow. *AIAA Journal*, 54(5):1628–1636, May 2016.

[35] P.B. Kirk and A.R. Jones. Vortex formation on surging airfoils with application to reverse flow modeling. *Journal of Fluid Mechanics*, 859:59–88, January 2018.

[36] L.W. McCroskey, W.J.and Carr and K.W. McAlister. Dynamic stall experiments on oscillating airfoils. *AIAA Journal*, 14(1):57–63, 1976.

[37] L.W. Carr, K.W. McAlister, and W.J. McCroskey. Analysis of the development of dynamic stall based on oscillating airfoil experiments. NASA Technical Note TN D-8382, 1977.

[38] K.W. McAlister, L.W. Carr, and W.J. McCroskey. Dynamic stall experiments on the NACA 0012 airfoil. NASA Technical Paper 1100, 1978.

[39] W.J. McCroskey. The phenomenon of dynamic stall. NASA Technical Memorandum 81264, March 1981.

[40] P.F. Lorber and F.O. Carta. Airfoil dynamic stall at constant pitch rate and high Reynolds number. *Journal of Aircraft*, 25(6):548–556, 1988.

[41] K. Mulleners and M. Raffel. The onset of dynamic stall revisited. *Experiments in Fluids*, 52(3):779–793, 2012.

[42] J.G. Leishman and T.S. Beddoes. A semi-empirical model for dynamic stall. *Journal of the American Helicopter Society*, 34(3):3–17, July 1989.

[43] K.W. McAlister, O. Lambert, and D. Petot. Application of the ONERA model of dynamic stall. NASA Technical Paper 2399, 1984.

[44] H. Küssner. Summary report on the instationary lift of wings. *Luftfahrtforschung*, 13:410–424, 1936.

[45] H.A. Wagner. *On the Original of the Dynamic Lift of Wings*. PhD thesis, Zeitshrift für angewandte Mathematik and Mechanik, 1925.

[46] A. H. Lind and A. R. Jones. Unsteady aerodynamics of reverse flow dynamic stall on an oscillating blade section. *Physics of Fluids*, 28(7):1–22, July 2016.

[47] L.R. Smith, A.H. Lind, K. Jacobson, M.J. Smith, and A.R. Jones. Experimental and computational investigation of a linearly pitching NACA 0012 in reverse flow. In *72nd Annual Forum of the AHS*, May 2016.

[48] J. Katz. A discrete vortex method for the non-steady separated flow over an airfoil. *Journal of Fluid Mechanics*, 102:315–328, 1981.

[49] S.A. Ansari, R. Zbikowski, and K. Knowles. Non-linear unsteady aerodynamics model for insect-like flapping wings in the hover. part 1: Methodology and analysis. *Journal of Aerospace Engineering*, 220(2):61–83, February 2006.

[50] S.A. Ansari, R. Zbikowski, and K. Knowles. Non-linear unsteady aerodynamics model for insect-like flapping wings in the hover. part 2: Implementation and validation. *Journal of Aerospace Engineering*, 220(3):169–186, March 2006.

[51] J. Kriegseis, M. Kinzel, and D.E. Rival. On the persistence of memory: do initial conditions impact vortex formation? *Journal of Fluid Mechanics*, 736:91–106, 2013.

[52] C. Wang and J.D. Eldridge. Low-order phenomenological modeling of leading-edge vortex formation. *Theoretical and Computational Fluid Dynamics*, 27(5):577–598, 2013.

[53] P. Hammer, A. Altman, and F. Eastep. Validation of a discrete vortex method for low Reynolds number unsteady flows. *AIAA Journal*, 52(3):643–649, 2014.

[54] Field H. Manar. *Measurements and Modeling of the Unsteady Flow Around a Thin Wing*. PhD thesis, University of Maryland, College Park, May 2018.

[55] D. Darakananda and J.D. Eldredge. A versatile taxonomy of low-dimensional vortex models for unsteady aerodynamics. *Journal of Fluid Mechanics*, 858:917–948, 2019.

[56] L. Greengard. The fmmlib2d suite. `https://cims.nyu.edu/cmcl/fmm2dlib/fmm2dlib.html`, 2012.

[57] D.W. Moore. A numerical study of the roll-up of a finite vortex sheet. *Journal of Fluid Mechanics*, 63(2):225–235, 1974.

[58] A. SureshBabu, K. Ramesh, and A. Gopalarathnam. Model reduction in discrete-vortex methods for unsteady airfoil flows. *AIAA Journal*, 57(4):1409–1422, April 2019.

[59] K. Ramesh, A. Gopalarathnam, K. Granlund, M.V. Ol, and J.R. Edwards. Theoretical modeling of leading edge vortices using the leading edge suction parameter. In *30th AIAA Applied Aerodynamics Conference*, New Orleans, Louisiana, June 2012.

[60] L.M. Milne-Thompson. *Theoretical Hydrodynamics*. Dover Publications, 5th edition, 2011.

[61] R.K. Shukla and J.D. Eldredge. An inviscid model for vortex shedding from a deformed body. *Theoretical and Computational Fluid Dynamics*, 21(5):343 – 368, 2007.

[62] K. Ramesh, A. Gopalarathnam, J.R. Edwards, M.V. Ol, and K. Granlund. An unsteady airfoil theory apllied to pitching motions validates against experiment and computation. *Theoretical and Computational Fluid Dynamics*, 27(6):843–864, 2013.

[63] J. Katz and A. Plotkin. *Low-Speed Aerodynamics*. Cambridge University Press, 2nd edition, 2001.

[64] J.L. Hess. Panel methods in computational fluid dynamics. *Annual Review of Fluid Mechanics*, 22:255–274, 1990.

[65] S. Bal. A potential based panel method for 2-D hydrofoils. *Ocean Engineering*, 26(4):343–361, August 1998.

[66] L. Fornasier. Linearized potential flow analysis of complex aircraft configurations by HISSS, a higher-order panel method. In *23rd AIAA Aerospace Sciences Meeting*, Reno, Nevada, January 14 -17 1985.

[67] J.D. Anderson Jr. *Fundamentals of Aerodynamics*. McGraw Hill, 5th edition, 2011.

[68] S.A. Kinnas and C. Hsin. Boundary element method for the analysis of the unsteady flow around extreme propellor geometries. *AIAA Journal*, 30(3):688–696, March 1992.

[69] P.R. Spalart. Vortex methods for separated flows. NASA Technical Memorandum 100068, June 1988.

[70] G. Cottet and P.D. Koumoutsakos. *Vortex Methods: Theory and Practice.* Cambridge University Press, 1st edition, 2000.

[71] F. Manar and A.R. Jones. Evaluation of potential flow models for unsteady separated flow with respect to experimental data. *Physics of Fluids*, 4(3):034702, 2019.

[72] K. Pohlhausen. Zur näherungsweisen integration der differentialgleichung der laminaren grenzschicht. *Zeitshrift für angewandte Mathematik and Mechanik*, 1(4):252–290, January 1921.

[73] B. Thwaites. Approximate calculation of the laminar boundary layer. *The Aeronautical Quarterly*, 1(3):245–280, November 1949.

[74] J.A. Ekaterinaris. Computational prediction of airfoil dynamic stall. *Progress in Aerospace Science*, 33:759–846, 1997.

[75] H. Schlichting. *Boundary Layer Theory.* Springer, 9th edition, 2017.

[76] R.C. Lock and B.R. Williams. Viscous-inviscid interactions in external aerodynamics. *Progress in Aerospace Sciences*, 24(2):51–171, 1987.

[77] M. Drela and M.B. Giles. Viscous-inviscid analysis of transonic and low Reynolds number airfoils. *AIAA Journal*, 25(10):1347–1355, October 1987.

[78] N. Ramos-Garcia, J.N. Sorensen, and W.Z. Shen. A strong viscous-inviscid interaction model for rotating airfoils. *Wind Energy*, 17(12):1957–1984, December 2014.

[79] K. Ramesh, K. Granlund, M.V. Ol, A. Gopalarathnam, and J.R. Edwards. Leading-edge flow criticality as a governing factor in leading-edge vortex initiation in unsteady airfoil flows. *Theoretical and Computational Fluid Dynamics*, 32:109–136, August 2017.

[80] K. Ramesh, A. Gopalarathnam, K. Granlund, and M.V. Ol. Discrete-vortex method with novel shedding criterion for unsteady aerofoil flows with intermittent leading-edge vortex shedding. *Journal of Fluid Mechanics*, 751:500–538, July 2014.

[81] A. Medina, A.V.S. Babu, M. Rockwood, A. Gopalarathnam, and A. Ahmed. Theoretical and experimental study of wake encounters on unsteady airfoils. In *57th AIAA Aerospace Sciences Meeting*, San Diego, California, January 7 -11 2019.

[82] T. Cebeci, M.F. Platzer, H.M. Hang, and H.H Chen. An inviscid-viscous interaction approach to the calculation of dynamic stall initiation on airfoils. *Journal of Turbomachinery*, 115(4):1–11, October 1993.

[83] K.D. Jones and M.F. Platzer. On the prediction of dynamic stall onset on airfoils in low speed flow. In *Unsteady Aerodynamics and Aeroelasticity of Turbomachines*, pages 1–11, 1998.

[84] N.M. Chaderjian. Navier-Stokes simulation of UH-60A rotor/wake interaction using adaptive mesh refinement. In *The 73rd Annual Forum of the AHS*, Fort Worth, Texas, May 2017.

[85] M. Potsdam, A. Datta, and B. Jayaraman. Computational investigation and fundamental understanding of a slowed UH-60A rotor at high advance ratios. *Journal of the American Helicopter Society*, 61(2), April 2016.

[86] C.J. Wojcik and J.H.J. Buchholz. Vorticity transport in the leading-edge vortex on a rotating blade. *Journal of Fluid Mechanics*, 743:249–261, March 2014.

[87] A.E. Panah, J.M. Akkala, and J.H.J. Buchholz. Vorticity transport and the leading-edge vortex of a plunging airfoil. *Experiments in Fluids*, 56(160), 2015.

[88] J. Akkala. *Understanding and Controlling Vorticity Transport in Unsteady, Separated Flows.* PhD thesis, University of Iowa, December 2015.

[89] X. Wang, Y. Jung, J. Baeder, and I. Chopra. CFD pressure/airload correlation with experimental data on a slowed rotor at high advance ratios. In *74th Annual Forum of the American Helicopter Society*, Phoenix, Arizona, May 14 - 17 2018. 74-2018-1272.

[90] K. Ferguson and D. Thomson. A performance analysis of compound helicopter configurations. In *70th Annual Forum of the AHS*, Montreal, Canada, May 2014.

[91] Y. Jung, B. Govindarajan, and J. Baeder. A Hamiltonian-strand approach for aerodynamic flows using overset and hybrid meshes. In *72nd Annual Forum of the AHS*, West Palm Beach, Florida, May 17 - 19 2016. 72-2016-280.

[92] Y. Jung, B. Govindarajan, and J. Baeder. Turbulent and unsteady flows on unstructured line-based Hamiltonian paths and strands grids. *AIAA Journal*, 55(6), 2017.

[93] Y. Jung. *Hamiltonian Paths and Strands for Unified Grid Approach for Computing Aerodynamic Flows.* PhD thesis, University of Maryland, College Park, 2019.

[94] G. Rubinstein, D.M. Moy, A. Sridharan, and I. Chopra. A Python-based framework for real-time simulation using comprehensive analysis. In *72nd Annual Forum of the AHS*, West Palm Beach, Florida, May 17 - 19 2016. 72-2016-323.

[95] L.R. Smith, Y. Jung, J.D. Baeder, and A.R. Jones. The role of rotary motion on vortices in reverse flow. *Journal of Fluid Mechanics*, 880:723–742, 2019.

[96] C. van den Berg and C.P. Ellington. The three-dimensional leading-edge vortex of a 'hovering' model hawkmoth. *Philosophical Transactions B*, 352(1351):329–340, 1997.

[97] J.D. Eldredge and A.R. Jones. Leading-edge vortices: mechanics and modeling. *Annual Review of Fluid Mechanics*, 51(1):75–104, 2019.

[98] A. Medina and Anya R. Jones. Leading-edge vortex burst on a low-aspect-ratio rotating flat plate. *Physical Review Fluids*, 1:044501, Aug 2016.

[99] J.Z. Wu, X.H. Wu, and J.M. Wu. Streaming vorticity flux from oscillating walls with finite amplitude. *Physics of Fluids*, 5(8):1933–1938, 1993.

[100] Jean M. Delery. Aspects of vortex breakdown. *Progress in Aerospace Sciences*, 30(1):1–59, 1994.

[101] A.R. Jones, A. Medina, H. Spooner, and K. Mulleners. Characterizing a burst leading-edge vortex on a rotating flat plate. *Experiments in Fluids*, 57(52):1–16, 2016.

[102] C.P. Ellington, C. van den Berg, A.P. Willmott, and A.L.R. Thomas. Leading-edge vortices in insect flight. *Nature*, 384:626–630, 1996.

[103] T. Jardin and L. David. Spanwise gradients in flow speed help stabilize leading-edge vortices on revolving wings. *Physical Review E*, 90(1):013011, 2014.

[104] T. Jardin. Coriolis effect and the attachment of the leading edge vortex. *Journal of Fluid Mechanics*, 820:312–340, 2017.

[105] M. Goman and A. Khrabrov. State-space representation of aerodynamic characteristics of an aircraft at high angles of attack. *Journal of Aircraft*, 31(5):1109–1115, 1994.

[106] J.W. Larsen, S.R.K. Nielsen, and S. Krenk. Dynamic stall model for wind turbine airfoils. *Journal of Fluids and Structures*, 23:959–982, 2007.

[107] B.A. Roccia, S. Preidikman, and J.C. Massa. Modified unsteady vortex-lattice method to study flapping wings in hover. *AIAA Journal*, 51(11):2628–2642, November 2013.

[108] X. Xia and K. Mohseni. Lift evaluation of a two-dimensional pitching flat plate. *Physics of Fluids*, 25(9):091901, 2013.

[109] H.A. Dwyer and W.J. McCroskey. Crossflow and unsteady boundary-layer effects on rotating blades. *AIAA Journal*, 9(8):1498–1505, August 1971.

[110] T. Fang. A note on the unsteady boundary layers over a flat plate. *International Journal of Non-Linear Mechanics*, 43(9):1007–1011, November 2008.

[111] A.M.O. Smith. Rapid laminar boundary-layer calculations by piecewise application of similar solutions. *Journal of the Aeronautical Sciences*, 23(10):901–912, October 1956.

[112] E.M. Sparrow, H. Quack, and C.J. Boerner. Local nonsimilarity boundary-layer solutions. *AIAA Journal*, 8(11):1936–1942, November 1970.

[113] M.R. Head. An approximate method of calculating the laminar boundary layer in two-dimensional incompressible flow. Aeronautical research counsel reports and memoranda, March 1957.

[114] F.M. White. *Viscous Fluid Flow*. McGraw-Hill, 2nd edition, 1991.

[115] C.F. Dewey Jr. and J.F. Gross. Exact similar solutions of the laminar boundary-layer equations. *Advances in Heat Transfer*, 4:317–355, 357–446, 1967.

[116] W. Sheng, R.A. McD. Galbraith, and F.N. Cotton. A new stall-onset criterion for low speed dynamic-stall. *Journal of Solar Energy Engineering*, 128(4):461–471, November 2006.

[117] J.D. Eldredge. A reconciliation of viscous and inviscid approaches to computing locomotion of deforming bodies. *Experimental Mechanics*, 50:1349–1353, 2010.

[118] A. Bauknecht, X. Wang, and I. Chopra. Wind tunnel test of a rotorcraft with lift compounding. In *45th European Rotorcraft Forum*, Warsaw, Poland, September 17 -20 2019. 0125.

[119] J.R. Ewans and T.A. Krauss. Model wind tunnel tests of a reverse velocity rotor system. DTIC document, 1973.